2013-08-13

Vision-Based Guidance for Air-to-Air Tracking and Rendezvous of Unmanned Aircraft Systems

Joseph Walter Nichols
Brigham Young University - Provo

Vision-Based Guidance for Air-to-Air Tracking and Rendezvous of Unmanned Aircraft Systems

Joseph W. Nichols

A dissertation submitted to the faculty of
Brigham Young University
in partial fulfillment of the requirements for the degree of

Doctor of Philosophy

Timothy W. McLain, Chair
Randal W. Beard
Mark B. Colton
Christopher A. Mattson
Bryan S. Morse

Department of Mechanical Engineering

Brigham Young University

August 2013

ABSTRACT

Vision-Based Guidance for Air-to-Air Tracking and Rendezvous
of Unmanned Aircraft Systems

Joseph W. Nichols
Department of Mechanical Engineering, BYU
Doctor of Philosophy

This dissertation develops the visual pursuit method for air-to-air tracking and rendezvous of unmanned aircraft systems. It also shows the development of vector-field and proportional-integral methods for controlling UAS flight in formation with other aircraft. The visual pursuit method is a nonlinear guidance method that uses vision-based line of sight angles as inputs to the algorithm that produces pitch rate, bank angle and airspeed commands for the autopilot to use in aircraft control. The method is shown to be convergent about the center of the camera image frame and to be stable in the sense of Lyapunov. In the lateral direction, the guidance method is optimized to balance the pursuit heading with respect to the prevailing wind and the location of the target on the image plane to improve tracking performance in high winds and reduce bank angle effort. In both simulation and flight experimentation, visual pursuit is shown to be effective in providing flight guidance in strong winds.

Visual pursuit is also shown to be effective in guiding the seeker while performing aerial docking with a towed aerial drogue. Flight trials demonstrated the ability to guide to within a few meters of the drogue. Further research developed a method to improve docking performance by artificially increasing the length of the line of sight vector at close range to the target to prevent flight control saturation. This improvement to visual pursuit was shown to be an effective method for providing guidance during aerial docking simulations.

An analysis of the visual pursuit method is provided using the method of adjoints to evaluate the effects of airspeed, closing velocity, system time constant, sensor delay and target motion on docking performance. A method for predicting docking accuracy is developed and shown to be useful for predicting docking performance for small and large unmanned aircraft systems.

Keywords: aerial docking, aerial recovery, aerial rendezvous, air-to-air tracking, autonomous formation flight, Lyapunov stability, nonlinear control, unmanned aircraft system, UAS, UAV, vector-field guidance, vision-based guidance

ACKNOWLEDGMENTS

I am extremely blessed to have had the opportunity to once again study at Brigham Young University. I have loved being on campus and associating with the professors and students that make this university truly unique among the great institutions of learning.

I appreciate Dr. Tim McLain for taking me on as one of his graduate students and providing the mentoring and guidance that were essential to completing this work. Dr. Randy Beard has been a source of ideas and encouragement to solve the technical challenges associated with this research. I want to acknowledge the help of Dr. Mark Colton for his collaboration on vector-field methods. Dr. Bryan Morse provided consultations on computer vision and statistical processes at key points in my research, and I thank Dr. Chris Mattson for his timely advice and encouragement. I appreciate the friendship and concern shown by Miriam Busch, the department graduate advisor, throughout my time at BYU.

I am grateful for my friends in the MAGICC Lab for their assistance and companionship. In particular I want to acknowledge the other students on the aerial recovery project: Daniel Carlson, Mark Owen, Jeff Ferrin, Dallin Briggs, and Liang Sun; and thank them for their help as we worked through the many hardware challenges associated with flying two unmanned aircraft and a towed drogue in formation. I also want to thank my lab colleagues, Rob Leishman, Peter Neidfeldt, and Robert Klaus for being willing to drop whatever they were doing to consult and help me in numerous ways.

Most importantly, I would like to thank my wife, Diane, for her encouragement and patience as I have pursued this educational opportunity at this late date in my working career. I also thank my children and father for their interest and continuous displays of support throughout my studies.

I appreciate the Department of Mechanical Engineering for providing a research fellowship and the Department of Veterans Affairs for their financial support through the GI Bill. Research funding for part of this work was provided by the Air Force Office of Scientific Research through

the Small Business Technology Transfer Program, contract number FA9550-10-C-0041, and in co-operation with Lockheed Martin Procerus Technologies. This support is gratefully acknowledged. In addition, I want to thank Mr. Neil Johnson from Lockheed Martin Procerus Technologies for his assistance in coding the methods developed in the paper for implementation on the Vision Processing Unit, and for assisting in the flight trials.

TABLE OF CONTENTS

LIST OF TABLES . . . . . **viii**

LIST OF FIGURES . . . . . **ix**

NOMENCLATURE . . . . . **xi**

Chapter 1 Introduction **1**
1.1 Motivation 1
1.2 Problem Statement 2
1.3 Definitions 4
1.4 Literature Review 4
1.4.1 Vector Field Following 4
1.4.2 Guidance for Air-to-Air Tracking 5
1.4.3 Aerial Rendezvous 6
1.5 Contributions 7
1.5.1 Enhanced Vector Field Tracking 7
1.5.2 Visual Pursuit 8
1.5.3 Aerial Docking 9
1.6 Organization 9

Chapter 2 Simulation Tools and Experimental Hardware **11**
2.1 Simulation 11
2.2 Hardware 12
2.2.1 Seeker 12
2.2.2 Mothership 13
2.2.3 Drogue 15
2.2.4 Ground Station 15

Chapter 3 Air-to-Air Rendezvous using Vector Field Methods **19**
3.1 Introduction 19
3.2 Orbit Tracking Using Vector Fields 20
3.3 Vision-based Enhancements to Orbit Tracking Using Vector Fields 25
3.3.1 Interior Orbit Following for Improved Vehicle Tracking 25
3.3.2 Altitude Bias Correction Using Vision 27
3.4 Experimental Results 30
3.5 Chapter Summary 33

Chapter 4 Visual Pursuit **34**
4.1 Introduction 34
4.2 Model Development 36
4.2.1 Coordinate Frames 36
4.2.2 Camera Geometry 37

4.2.3 System Dynamics . . . 38
4.3 Guidance Methods . . . 42
4.3.1 Proportional-Integral Pursuit . . . 42
4.3.2 Visual Pursuit . . . 43
4.3.3 Limitations . . . 52
4.4 Guidance Laws from Decoupled Dynamics . . . 55
4.5 Simulation Results . . . 56
4.6 Experimental Results . . . 60
4.6.1 Tracking Algorithm Performance . . . 60
4.6.2 Vision Sensor Performance . . . 61
4.7 Chapter Summary . . . 64

Chapter 5 Aerial Docking Using a Passive Towed Cable System . . . 66
5.1 Introduction . . . 66
5.2 Seeker Guidance . . . 67
5.3 Experimental Results . . . 68
5.4 Modified Visual Pursuit for Near-target Maneuvering . . . 71
5.4.1 Minimum-distance Contact Factor . . . 73
5.4.2 Fixed-length Contact Factor . . . 74
5.4.3 Comparison of Methods . . . 75
5.5 Chapter Summary . . . 78

Chapter 6 Adjoint Analysis of Aerial Docking System . . . 79
6.1 Introduction . . . 79
6.2 Linearization and Model Simplification . . . 79
6.2.1 Linear Longitudinal Guidance Model . . . 81
6.2.2 Linear Lateral Guidance Model . . . 83
6.2.3 Model Stability . . . 85
6.3 Method of Adjoints . . . 87
6.4 Target Motion . . . 89
6.5 Seeker Maneuverability . . . 97
6.6 Velocity Effects . . . 101
6.7 Sensor Effects . . . 102
6.8 Comparison of Large and Small UAS Performance Using Visual Pursuit . . . 107
6.9 Chapter Summary . . . 109

Chapter 7 Conclusions and Future Work . . . 110
7.1 Summary of Main Results . . . 110
7.2 Future Work . . . 110
7.3 Conclusions . . . 111

REFERENCES . . . 114

Appendix A Guidance Laws from Decoupled Dynamics . . . 118
A.1 Longitudinal Dynamics . . . 118

A.2 Lateral Dynamics 120
A.3 Visual Pursuit in Two Dimensions 123
A.4 Simulation Results 129

LIST OF TABLES

4.1 Simulation LOS angle comparison 59
4.2 Flight trial LOS angle comparison 65

5.1 Comparison of minimum-distance and fixed-length contact factor performance . . 76

6.1 Nominal system variables 85
6.2 Nominal system variables 95
6.3 Nominal system variables 97
6.4 Small and large UAS system characteristics 108
6.5 Docking simulation results 108

A.1 Comparison of coupled and decoupled guidance laws during docking 129
A.2 Comparison of coupled and decoupled guidance laws during tracking 131

LIST OF FIGURES

1.1 Aerial recovery concept. 1

2.1 System architecture. 12
2.2 Internal communication block diagram. 13
2.3 Seeker aircraft. 14
2.4 Mothership preparing for takeoff. 15
2.5 Drogue system. 16
2.6 Drogue launch procedure. 16
2.7 Ground station display. 17

3.1 Flight path defined by intersecting surfaces. 20
3.2 Seeker orbit modification for improved LOS 26
3.3 Camera image frame. 28
3.4 Vector field following distance test results. 30
3.5 Video frame from seeker camera 31
3.6 Enhanced vector field following test results. 32

4.1 Proportional navigation and pursuit guidance methods 35
4.2 Seeker and target in formation flight 36
4.3 Seeker camera frame. 37
4.4 Longitudinal dynamics 38
4.5 Lateral dynamics 39
4.6 Control system block diagram 44
4.7 Comparison of guidance commands and dynamic response 51
4.8 Hidden dynamic response 53
4.9 Flight control saturation limits 55
4.10 Waggle maneuver 57
4.11 Comparison of PI and visual pursuit tracking 58
4.12 Comparison of PI and visual pursuit tracking in crosswind 60
4.13 Guidance method results 62
4.14 Seeker video frame with track enabled 63
4.15 Vision-based results 64

5.1 Drogue altitude deviation in the presence of wind 66
5.2 Drogue in seeker image 69
5.3 Flight test results. 70
5.4 Lateral dynamics for fixed contact factor. 72
5.5 Fixed-length and minimum-distance contact factor comparison 75
5.6 Contact factor LOS distance error comparison. 77
5.7 Docking performance comparison using the contact factor 78

6.1 Comparison of linear and nonlinear guidance models 81
6.2 Linearized longitudinal guidance system 82
6.3 Linearized lateral guidance system 84

6.4 Stability of linearized system . . . 86
6.5 Lateral adjoint system . . . 88
6.6 Longitudinal adjoint system . . . 90
6.7 Lateral adjoint system . . . 91
6.8 Longitudinal step and sine target motion . . . 92
6.9 Step response . . . 92
6.10 Sine response . . . 93
6.11 Adjoint system for white noise . . . 94
6.12 Sine response . . . 95
6.13 Comparison of adjoint simulation and forward simulation . . . 96
6.14 Stability of linearized closed loop guidance system . . . 98
6.15 System time constant effect on miss distance . . . 99
6.16 Non dimensional miss distance . . . 100
6.17 Closure velocity effect . . . 102
6.18 Airspeed effect . . . 103
6.19 Sensor noise effect . . . 103
6.20 Sensor delay effect on stability . . . 106
6.21 Sensor delay effect on performance . . . 107

A.1 Longitudinal dynamics . . . 119
A.2 Lateral dynamics . . . 121
A.3 Comparison of coupled and decoupled guidance laws during docking . . . 130
A.4 Comparison of coupled and decoupled guidance laws during tracking . . . 132
A.5 Comparison of coupled and decoupled LOS during tracking . . . 133

NOMENCLATURE

a, b	ellipse major and minor radii
A	drogue oscillation amplitude (m)
$\mathbf{C}$	contact factor vector
C	contact factor distance (m)
d	horizontal seeker distance behind target (m)
d^c	desired seeker distance behind target (m)
f	camera focal length (pixels)
g	gravitational acceleration (9.81 m/s)
G	vector field contraction strength weighting function
G_i	forward path transfer function
H	vector field circulation vs contraction weighting factor
h_{bias}	GPS altitude bias (m)
h_D	drogue altitude (m)
h_S	seeker altitude (m)
i	unit vector in the camera frame
j	unit vector in the camera frame
k	unit vector in the camera frame
K	selectable control gain
L	lateral LOS distance (m)
L_i	feedback loop transfer function
$\mathbf{L}$	two-dimensional lateral LOS vector
P	longitudinal LOS distance (m)
$\mathbf{P}$	two-dimensional longitudinal LOS vector
$\dot{p}_n^d$	desired north velocity in inertial frame (m/s)
$\dot{p}_e^d$	desired east velocity in inertial frame (m/s)
$\dot{p}_d^d$	desired down velocity in inertial frame (m/s)
q	pitch rate (rad/s)
r	yaw rate (rad/s)
r_{eff}	effective radius of elliptical orbit (m)
R	radius of mothership orbit (m)
R_1	drogue orbit radius (m)
R_2	UAS orbit radius (m)
$\mathbf{R}$	rotation matrix
t	system time (s)
T	time step (s)
T_d	sensor time delay (s)
T_f	final time (s)
u	vector field function output, vector of directional velocity commands
$\mathbf{V}$	vector field scalar potential function
V	airspeed (m/s)
V_C	closure airspeed (m/s)
V_D	drogue airspeed (m/s)
V_S	seeker airspeed (m/s)

V_g	UAS ground speed (m/s)
$\mathbf{v}_D$	drogue velocity vector
$\mathbf{v}_S$	seeker velocity vector
$\mathbf{W}$	scalar Lyapunov function
$\mathbf{w}^*$	adjoint system output
x_i	position variable in each of the three dimensions
y_{miss}	docking miss distance (m)
y^*	non-dimensional maximum miss distance
α_i	vector field surface functions
α	UAS angle of attack
β	longitudinal line-of-sight angle or elevation (rad)
$\bar{\beta}$	longitudinal camera field-of-view limit (rad)
χ	Aircraft ground referenced course angle
Δh	UAS altitude difference from drogue altitude (m)
ε	distance from the center of the image (pixels)
ε_i	image pixels in i direction in camera frame
ε_j	image pixels in j direction in camera frame
η	lateral line-of-sight angle or azimuth (rad)
$\bar{\eta}$	lateral camera field-of-view limit (rad)
γ	flight path angle (rad)
ν	lateral LOS slack variable
ϕ	bank angle (rad)
Φ	power spectral density (rad^2/Hz)
ψ_S	seeker heading angle (rad)
ψ_T	target heading angle (rad)
ψ_1	rotation angle from ellipse frame to inertial frame
ψ_2	rotation angle from ellipse frame to inertial frame
ρ	line-of-sight distance from seeker to drogue (m)
$\boldsymbol{\rho}$	line-of-sight vector from seeker to target (m)
ρ_{fixed}	LOS distance using fixed-length contact factor (m)
ρ_{lim}	LOS distance using contact factor with minimum allowable distance (m)
σ	parameter describing parametric defined ellipse
τ	system time constant (s)
θ	pitch angle (rad)
ω	drogue oscillation frequency (rad/s)
ω	angular velocity (rad/s)

CHAPTER 1. INTRODUCTION

1.1 Motivation

Many small unmanned aircraft systems (UAS) have relatively short endurance and range when compared with manned aircraft. This limited endurance and range limits small UAS utilization when the objective is a long distance from a location where the aircraft can be safely launched and recovered. Providing a method for aerial rendezvous is one way to increase the utility of small UAS in these scenarios. A notional system consists of a larger aircraft to transport several small UAS to the area of interest, launch them, and subsequently autonomously retrieve them by deploying a high-drag drogue that allows the smaller UAS to match the angular velocity of the mothership, while at a much lower airspeed. The concept motivating this work is shown in Figure 1.1. This dissertation explores the technological challenges associated with a vision-based aerial rendezvous system for small UAS.

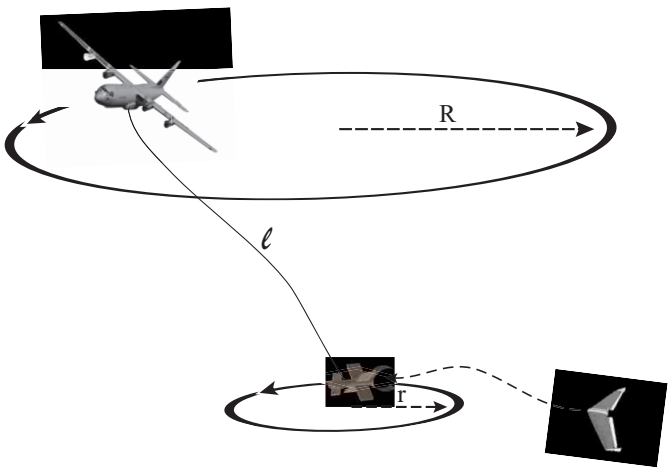

Figure 1.1: Aerial recovery concept. The mothership tows a high-drag drogue that is pulled into an interior orbit to facilitate aerial docking with a small UAS.

There are other UAS mission objectives that require solving the autonomous aerial docking problem. For example, autonomous aerial refueling requires that the seeker UAS acquire, track and fly in precise formation with the tanker vehicle and dock with a towed refueling drogue [1]. Another example would be autonomous formation flying to increase fuel savings by taking advantage of the wing-tip vortices of the lead aircraft [2] or flying in formation with manned or unmanned aircraft to transit controlled airspace [3].

The experimental approach taken in this work is to employ a drogue towed by a flexible cable attached to a larger UAS or mothership. The minimum velocity of the mothership is likely to be much faster than the maximum velocity of the UAS which necessitates a flexible cable system that will place the drogue in an orbit inside the mothership orbit and at a velocity achievable by the UAS. This dissertation focuses on developing a method for tracking and following an airborne towed drogue and subsequently closing the distance between the two and performing aerial docking.

1.2 Problem Statement

Guidance and navigation are generally considered to be two different things. One author explained it this way, ”One can almost say that if you know where you are and where you want to go, navigation would be the method for getting there. However, if you didn't know where you were or where you wanted to go, guidance would the method of getting you there [4].” Navigation works in an inertial reference frame and guidance works in a relative reference frame. The principal problem that this dissertation solves is development of a guidance method that is suitable for use with a camera system and autopilot to provide relative guidance for a small UAS tracking and rendezvousing with an airborne target. The following questions are addressed in this work.

- How do you command a UAS to follow and remain in formation with another UAS or towed drogue?
- How can a vision sensor be used to determine the relative position of a UAS and drogue?
- What guidance law works best for controlling the rendezvous and docking of two airborne vehicles?

- How do you control the rendezvous and docking of a UAS with a drogue in the presence of wind?
- How do you implement the developed guidance laws in flight hardware?

The context in which this guidance method is developed is the aerial recovery scenario shown in Figure 1.1. There are several other problems that must be solved in addition to seeker guidance that must be addressed. These include: controlling the shape of the drogue orbit, communicating the drogue path to the UAS, vision-based acquisition and tracking of the target, and finally the mechanism for docking and capture of the UAS by the drogue. Some of these have been investigated by others in the Multiple Agent Intelligent Coordination and Control (MAGICC) laboratory at BYU as part of the overall aerial recovery research effort.

For example, previous work indicates that a phenomenon of towed cable systems in wind is that the orbit of the free end of the cable will not be horizontal, but will be an inclined ellipse with its centroid pushed off center from the centroid of the fixed or towed end of the cable [5]. To improve the chance that a seeker UAS can dock with a passive drogue at the end of a circularly towed cable, the drogue orbit should be as horizontal as possible. Sun developed a methodology for producing desired mothership trajectories that would produce horizontal drogue orbits using differential flatness [6]. In experimental rendezvous trials for this dissertation, Sun's method was used to control the mothership flight path to keep the drogue orbit as horizontal as possible.

Acquiring and tracking the target using a vision system is a critical component of an aerial rendezvous system. There have been a number of methods developed using computer vision techniques. Some of these include using mean shift algorithms [7, 8], machine vision with pattern recognition [9, 10], or a feature detection algorithm like edge detection [11]. During the work on this dissertation a rudimentary mean shift tracking algorithm was developed and tested. However, the experimental hardware used in this work included a built-in edge detector embedded on the Vision Processing Unit described in Chapter 2. The VPU could not be altered as part of this project and therefore experimentation was limited to techniques compatible with this tracker.

For control strategies using towed-body active control and cable length regulation, additional efforts are needed to design specific mechanisms for the towed body along with extra devices for cable length control like winches. The more versatile strategy for motion control of towed

cable systems is a maneuverable towed vehicle. An actively controlled drogue was designed and flight tested as part of this research, but the vehicle was never mature enough to test with the entire aerial recovery system [12]. Therefore, all rendezvous techniques developed in this dissertation were tested against a passive drogue. No work was performed on a capture method.

1.3 Definitions

Referring again to Figure 1.1, the small UAS that attempts to rendezvous with the drogue is referred to as the seeker throughout this dissertation. The seeker may be following a towed vehicle as shown in the figure, or another UAS. The airborne vehicle that the seeker is following is called the target, or when following a towed vehicle, it is referred to as the drogue. The UAS towing the drogue is referred to as the mothership. When the UAS are intentionally flying near one another they are said to be flying in formation; a term commonly used in military aviation when aircraft are flying together with a lead and one or more wingmen.

Rendezvous is used to describe the seeker attempting to close the distance to the target. This may be to get into position to fly in formation with the target or to perform aerial docking. Docking is used when the seeker is intentionally trying to make contact with the drogue while airborne.

1.4 Literature Review

Much of the prior work that influenced this dissertation is covered in the following subsections. This section is organized according to the three main research ares: vector field following, air-to-air tracking methods, and aerial rendezvous or docking.

1.4.1 Vector Field Following

Path following has been applied to many problems involving UAS. While many contributions have been made in the area of 2D path following [13, 14], research in 3D path following in which the control laws are proven to converge to the desired path is not nearly as developed. Some notable papers addressing this topic can be found in [15–17]. The work of Ambrosino [17] demonstrated 3D path planning and path following between two points with course and flight path

angle constraints, making use of a tracking algorithm that resembles line-of-sight based guidance. While this method is feasible for flying between two static points, such as on a landing approach, it does not allow for any time variance of the curve, start points or end points. A framework for constructing stable 3D Lyapunov vector fields around loiter orbits was developed in [15] but these principles were only demonstrated for horizontal, circular orbits and did not take into consideration the nontrivial problem of implementing such a control law on fixed-wing UAS. Gonçalves et al. [16] is a significant paper that provides further development of the closed curve tracking and extends it to n-dimensions while also accounting for possible time variance of the curve.

1.4.2 Guidance for Air-to-Air Tracking

Controls research in the area of vision-based rendezvous generally takes two approaches. In one approach, the guidance and control functions are completely integrated. A good example of this type of approach is a nonlinear vision-based method developed by Stepanyan and Hovakimyan [18]. In addition, most of the research assumes that the only information available to the seeker with respect to the target is the information that can be gleaned from the vision sensor and seeker autopilot. Some of the relevant work in this area includes research by Calise et al. that developed an estimation and guidance method for vision-based control using an extended Kalman filter formulation [19]. In Calise's work, no information other than noisy estimates of location and size from the camera were assumed. Position at long range was obtained through lateral movement of the target vehicle and at close range position was estimated through the change in the size of the target. Since we assume a cooperative target in this dissertation, we do not restrict ourselves to only vision-based information about the target. We allow the target to share state information with the seeker.

The other approach is to design separately the guidance and control functions and wrap an outer guidance loop around the inner aircraft control (autopilot) loop. This method assumes a well tested autopilot and therefore the research focuses on the outer guidance loop only. This strategy is more convenient for implementation in hardware, and it is therefore more generally applicable because the guidance laws can be implemented with a number of autopilot and airframe combinations. A good example of this approach is the work performed Park et al. [20] that produced a nonlinear method for path following that can be used for dynamic aerial target following as well.

This dissertation uses an outer guidance loop strategy called visual pursuit that enables a UAS to track and follow a cooperative aerial target. We begin with the dynamic equations of motion that define the relative lateral and longitudinal movement of a seeker and a cooperative target. These relationships form the basis for a guidance law that generates roll and climb rate commands for the seeker using a nonlinear Lyapunov approach. This approach ensures stability around the camera image center, and ensures that once the target is captured in the camera field-of-view (FOV) of the seeker it will remain in the FOV. The methods in this dissertation were developed for use with a vision sensor. However, it is also shown that these methods are effective in providing guidance using inputs from GPS. This is important, because research is being conducted into combining GPS with vision in autonomous aerial refueling [21]. For example, NASA successfully flew in formation and completed autonomous probe and drogue aerial refueling with an F-18 using a hybrid vision-GPS system that included a data link for passing relative position information between the tanker and the receiver aircraft [22]. Other sensors, in combination with vision or alone, may compensate for the limitations of vision-based guidance at close range to the target. Therefore the visual pursuit method developed here may be suitable with sensing systems beyond vision alone.

The visual pursuit method extends the work of Saunders and Beard [23] in a way that allows the target some movement within the FOV to provide tracking capabilities in high winds. Small UAS often operate at airspeeds below 25 m/s. In this region, winds are a significant environmental factor that must be considered for all useful applications.

1.4.3 Aerial Rendezvous

In the past, several publications investigated strategies for retrieval of UAS. Some of the proposed solutions included parachute systems, vertical takeoff and landing systems, and ship-based retrieval systems [24–26]. However, one of the central assumptions of the problem statement is that landing near the area of interest is not possible. There are many publications that consider the autonomous aerial refueling problem [9, 10, 27]. NASA has an ongoing effort to perform autonomous aerial refueling using two RQ-4 Global Hawk aircraft [1]. These works are typically concerned with large aircraft aerial refueling. While many of the techniques for accomplishing aerial rendezvous are germane to the small UAS problem, the flight environment is significantly

different. In the large aircraft aerial rendezvous environment, wake turbulence is the key external disturbance while wind velocity is generally a small fraction of the airspeed and not a significant factor. For small UAS, winds are the dominant external factor.

There has been considerable research in the Multiple Agent Intelligent Coordination & Control (MAGICC) laboratory at BYU on the various aspects of the small UAS aerial rendezvous problem [5, 6, 12, 28–36]. Small UAS tracking and rendezvous work by MIT provided inspiration for this work as well [37]. The MIT group succeeded in bringing two small UAS comparable in size to the aircraft used in this dissertation into formation and within a few meters of one another using a modified form of proportional navigation taken from missile guidance. Considerable inspiration for the guidance methods and simulation techniques developed in this work were taken from tactical missile guidance techniques [38, 39]. Tactical and anti-ballistic missile guidance also provided a framework for addressing the effects of an oscillating target and the speed of the control response of the seeker on rendezvous miss distance [4, 40]. In particular, the formation of an adjoint system from the guidance block diagram proved to be a valuable analysis tool. The adjoint method was first introduced by Laning and Battin in 1956 [41]. It has been used since the late 1970s in the design and analysis of control systems for air-to-air missile systems [42, 43]. We have adopted the method of adjoints in this dissertation for the analysis of the main UAS rendezvous guidance method developed herein.

1.5 Contributions

The following research contributions were made during the period of work on this dissertation.

1.5.1 Enhanced Vector Field Tracking

We developed and demonstrated a non-vision based vector-field method for UAS formation flight. Early in this work we desired to explore the flight regime where both seeker, drogue and mothership would operate and to fly all three in close proximity to one another. We wanted to gather data on the relative stability of the seeker and drogue as well as capture airborne video of the drogue from seeker aircraft to aide in the development of vision-based guidance methods. Drawing

on the work of Lawrence, Frew and Pisano [15] and Gonçalves et al. [16] we developed a path planning method that used the intersection of two surfaces to define the desired three-dimensional flight path. We used this vector field method to follow the drogue at close range [33] and collect useful development data.

We developed modifications to the basic vector-field method and demonstrated improved tracking performance by correcting for GPS altitude bias and modifying predicted orbit. We extended this method by altering the vector field orbit to provide a better camera view of the drogue while following an elliptical path, and implementing a compensation method for eliminating GPS altitude differences between the drogue and seeker using vision-based line of sight angles [34]. These contributions provide a non-vision-based approach to aerial tracking and autonomous formation flight with the ability to compensate for GPS altitude differences between two vehicles when vision data is available, even if vision is not used in seeker guidance.

1.5.2 Visual Pursuit

We developed and demonstrated proportional-integral UAS guidance method for vision-based control. To visually track an airborne target the pixel location of the target in the camera image is converted to longitudinal and lateral line of sight (LOS) angles. Two guidance methods were developed for using the LOS angles to provide bank and pitch rate commands to the seeker aircraft autopilot [36]. The first method developed was a linear proportional-integral method that required only the LOS angles for guidance. The method was tested in simulation and flown successfully onboard the seeker test aircraft where it demonstrated robust tracking performance and formation flight capabilities.

The second method developed was a nonlinear vision-based guidance method for UAS air-to-air tracking in high winds. The second method developed was a nonlinear method named *visual pursuit* that in addition to the vision-based LOS angles, required the cooperation of the target or drogue to relay its airspeed and heading. The method was developed by forming Lyapunov scalar functions, and from these functions deriving climb rate and roll controls that were shown to be stable about the center of the image frame. The lateral control had an additional feature that allowed the target to optimize its flight path with respect to the prevailing wind. For example when flying in strong cross winds, the target was allowed to move within a region around the center of

the image frame. This resulted in the seeker following the target using less bank angle effort than if the guidance method worked to zero all LOS errors. The methods developed in this dissertation are unique and improve the ability of a small UAS to track an aerial target in high winds.

1.5.3 Aerial Docking

We developed and demonstrated an aerial recovery system using a towed cable system. Visual pursuit was used to attempt aerial docking with a drogue. A number of attempts were made with the seeker passing within a few meters of the drogue [35]. The test data was analyzed to determine ways to improve docking performance. The visual pursuit method was modified by adding a *contact factor* to the longitudinal and lateral dynamics which prevents the LOS distance between the seeker and the drogue used in the guidance algorithms from becoming very small in the calculations and thus causing roll and climb rate commands to saturate at close proximity to the drogue. This modification improved the guidance method performance when the seeker was at close range to the drogue.

We showed the influence of airspeed, closing velocity, sensor delay, system time constant, control gain, and target movement on docking performance. It was observed that these factors may affect the ability of the seeker to dock with the drogue. Each of these factors were analyzed along with drogue movement to show the effect on stability and docking performance. A method for predicting docking performance was developed and demonstrated for small and large UAS.

1.6 Organization

The remainder of this dissertation is organized as follows. In Chapter 2, we describe the simulation software and experimental test tools used in conjunction with this research effort. In Chapter 3, we examine a non-vision-based tracking method using vector fields to follow an airborne target moving along an elliptical path. This method is augmented to provide better visual tracking and incorporate vision data to reduce altitude errors between the seeker and target. The contents of Chapter 3 were published in the proceedings of the AIAA, Guidance, Navigation and Control Conference in 2012 [34]. In Chapter 4, we develop a proportional-integral method and the visual pursuit guidance method. We demonstrate stability for visual pursuit in the sense of

Lyapunov and show how this method is effective at tracking an airborne target in a high-wind environment. The contents of Chapter 4 have been published in the International Journal of Micro Air Vehicles [36]. In Chapter 5, we extend the work presented in Chapter 4 to the aerial docking problem, and show aerial rendezvous and docking with a drogue being towed with a flexible cable. The work in Chapter 5 has been submitted for publication in the Journal of Guidance, Dynamics, and Control [35]. In Chapter 6, we develop an analytical method for characterizing the contributions of airspeed, roll time constant, sensor time delay and drogue movement to the ability of the seeker aircraft to dock with the drogue. In Chapter 7, we offer our concluding remarks and recommendations for future work. Appendix A contains an alternate development of visual pursuit using two-dimensional dynamics.

CHAPTER 2. SIMULATION TOOLS AND EXPERIMENTAL HARDWARE

2.1 Simulation

The main simulation tool used for this work was Matlab Simulink. A full six-degree-of-freedom (6-DOF) model of the UAS used in the experimental trials was developed based on the techniques of Beard and McLain [13]. This model was used to develop the linear pursuit and nonlinear visual pursuit algorithms described in this dissertation. Other simplified models were also developed in the Matlab Simulink environment for use in developing adjoint systems and computing Monte Carlo simulations that were essential to describing the interaction between the key variables that affect air-to-air docking.

Prior to experimental flight testing the guidance methods developed in this dissertation were ground tested using Virtual Cockpit 3D and Aviones. Virtual Cockpit 3D is the same software used to access autopilot variables and monitor aircraft status during flight. It can also communicate with a flight simulator program. The simulation environment that was used in conjunction with Virtual Cockpit 3D is called Aviones. Aviones simulates the UAS in-flight by calculating the state information feeding a simulated autopilot. The software provides visualization of the aircraft and terrain and communicates with Virtual Cockpit 3D over a TCP/IP connection as though the simulated aircraft was in-flight and communicating with the ground station via radio link [44]. The ground station functions in nearly an identical manner when working with Aviones or when conducting actual flight operations. Aviones was developed at BYU and the open source code can be downloaded at http://sourceforge.net/projects/aviones. Virtual Cockpit 3D and Aviones were used to verify algorithm functionality and maturity prior to experimentally testing them in the air.

2.2 Hardware

The overall system architecture for the hardware used in the flight trials for this dissertation is shown in Figure 2.1. The hardware consisted of four elements: a seeker aircraft which was equipped with a camera for visually tracking other airborne targets, a mothership vehicle for towing a passive drogue, a towed drogue, and a ground station with operator interfaces with the aircraft and down links for video and data. These elements are described in this chapter.

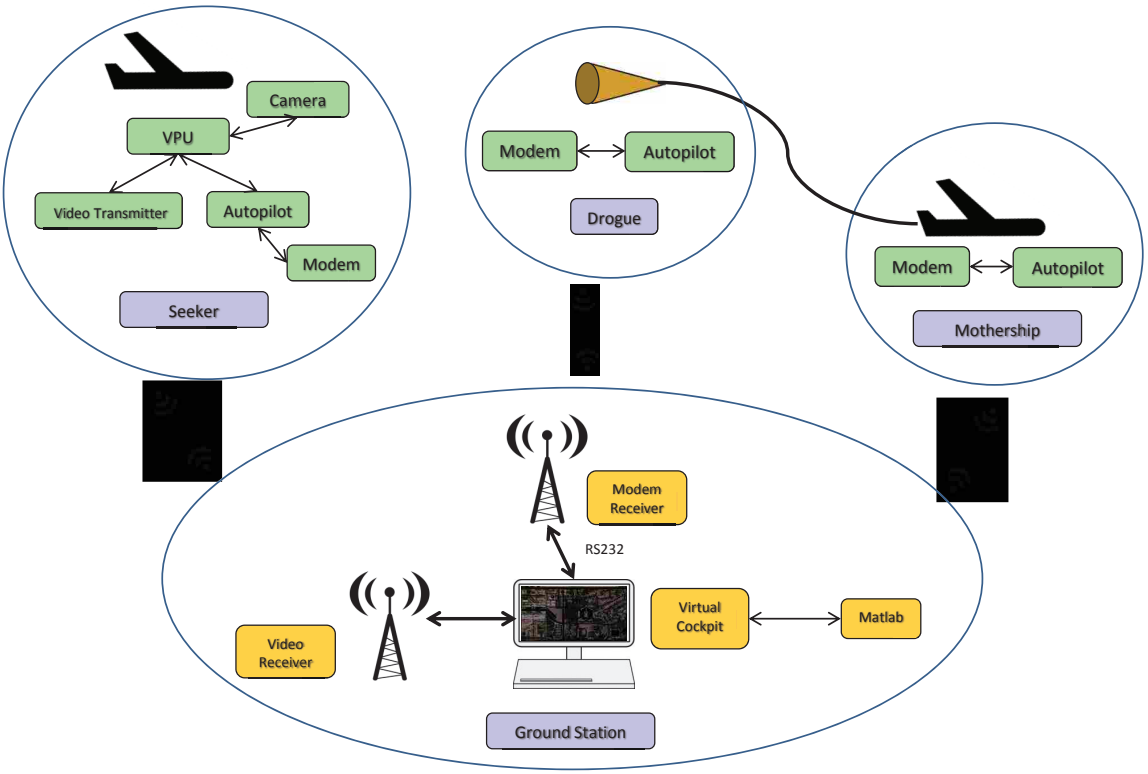

Figure 2.1: System architecture.

2.2.1 Seeker

Visual tracking methods were tested with a seeker following another UAS or a passively towed drogue. The aircraft used for the seeker is shown in Figure 2.3. It was a 1.4 m wing span elastic polypropylene (EPP) foam flying wing. This vehicle was equipped with GPS, a Kestrel 2 autopilot, and a vision processing unit (VPU) that interfaced directly with the camera. The seeker

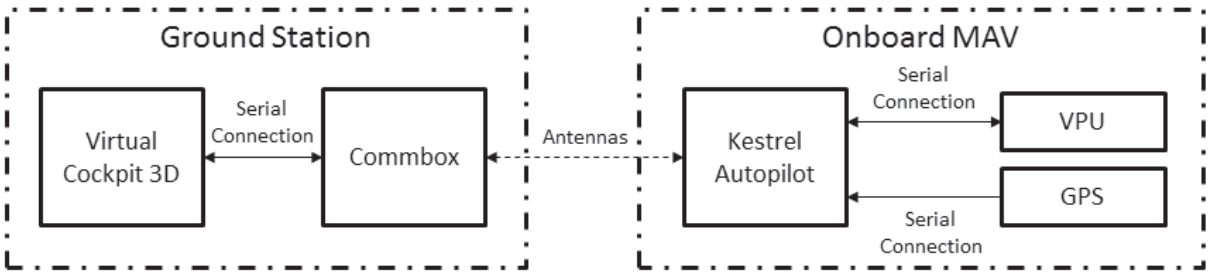

Figure 2.2: Internal communication block diagram.

was powered using two 5000 mAh lithium polymer batteries connected to a single 350 W Himax brushless motor. The seeker had a maximum flight time of 45 min. The autopilot interfaced with the ground station through an RF digital modem. The ground station sent high-level commands to the autopilot and VPU and received real-time vehicle telemetry from the autopilot as depicted in Figure 2.2.

The seeker guidance algorithms were implemented onboard the VPU. The VPU received autopilot telemetry packets and sent command packets to the autopilot at 30 Hz. The Kestrel autopilot loops ran at 50 Hz. For inner control loops, the autopilot climb rate control loop, the airspeed control loop, and the roll angle control loop were used. The outer guidance loop controlled the inner loop by sending airspeed, roll angle, and climb rate commands to the autopilot.

A digital camera was used in conjunction with the VPU. The fixed camera was mounted in the nose of the seeker and had a 78 deg field-of-view. Visual tracking techniques programmed on the VPU made it possible to manually designate user-selected airborne targets. The video feed was transmitted to the ground and displayed at the ground station. Using the ground station, the user manually selected the drogue or other targets that the UAS was commanded to follow. Particular attention was given to the location of the GPS antenna and processing unit with respect to the VPU. To prevent electro-magnetic interference on the video signal, the GPS had to be located at least 20 cm from the VPU.

2.2.2 Mothership

The aircraft used for the mothership is shown in Figure 2.4. It is a 1.4 m wing span Multiplex Twin Star airframe equipped with a Kestrel 2 autopilot and modem to communicate with

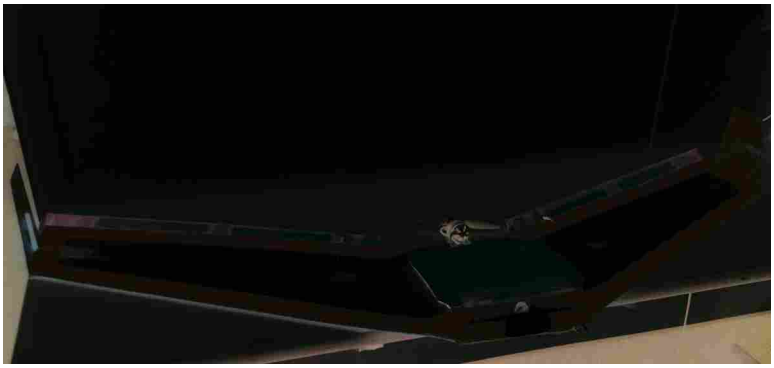

(a)

(b)

Figure 2.3: (a) Seeker vehicle is a 1.4 m wingspan flying wing equipped with an autopilot, camera, and on-board vision processing unit. (b) Cockpit.

the ground station. The autopilot contained an inertial measurement unit that estimated the vehicle state. A GPS unit provided position data. The mothership was powered using two 5000 mAh lithium polymer batteries connected to twin 910 W Turnigy motors typically using about 500 W each. When pulling the drogue, the mothership had a maximum flight time of 30 min. The mothership control algorithms were implemented in Matlab and run on the ground station computer. Mothership navigation waypoint commands were broadcast from the ground station to the mothership. Both the mothership and seeker were hand launched as shown in Figure 2.4 and belly landed.

Figure 2.4: Mothership preparing for takeoff.

2.2.3 Drogue

The 30 cm diameter hemisphere drogue used in this project was constructed of reinforced plastic as shown in Figure 2.5. Even though the drogue had no control surfaces, it was equipped with GPS and a Kestrel 2 autopilot and modem for reporting its position and velocity to the ground station. The drogue airspeed and heading were rebroadcast through the ground station to the seeker. The drogue was passive with no controllable surfaces and it was attached to the mothership using an $85 - 100$ m nylon cable. Launching a small UAS with a towed drogue was best accomplished by using a single loop of the cable and then launching the mothership on a heading 90 degrees from the layout of the cable as shown in Figure 2.6. This minimized the potential of tangling the cable and allowed the mothership to gain sufficient altitude and airspeed to pull the drogue up into the air avoiding low obstacles. The rendezvous methods were tested with the seeker following the hemispheric drogue attached to the mothership with a flexible cable. The drogue was towed in a circular orbit with an approximate airspeed of 15 m/s.

2.2.4 Ground Station

The ground station included a desktop computer that communicated with the autopilots on the mothership, drogue, and seeker, as well as the VPU on the seeker. The ground station allowed

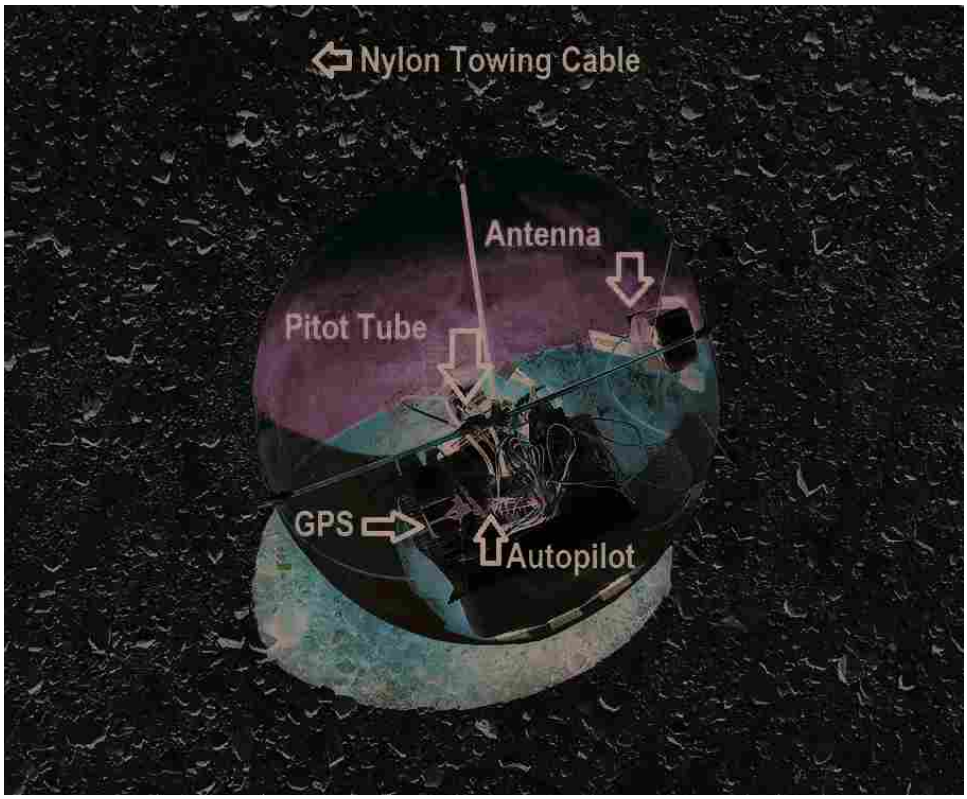

Figure 2.5: Drogue system.

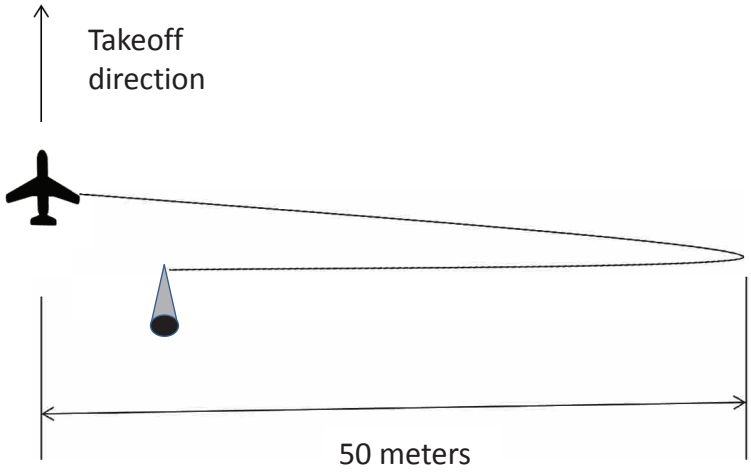

Figure 2.6: Drogue launch procedure.

Figure 2.7: Ground station display.

the operator to monitor the status of all three autopilots simultaneously and communicate with the VPU to change pursuit modes and designate airborne objects to be tracked by the VPU. The radio frequency video down link was at 2.4 GHz. The communications link with the autopilots was a 900 MHz data link that operated at 115.2 KB/s. In addition, the ground station computer had Matlab installed to run the control algorithms for the mothership. A screen shot from Virtual Cockpit 3D can be see in Figure 2.7

The autopilots communicated with the communications relay (Commbox) on the ground. The Commbox interfaced with the Virtual Cockpit 3D ground station software. This software was used to send high-level commands to the autopilot and VPU as well as receive realtime vehicle telemetry and produce plots of the vehicle navigation data. The high-level commands provided the ability to switch between guidance modes. A high-level block diagram of the system architecture can be seen in Figure 2.2. Vision-based tracking was initiated by looking at the real-time video in the ground station and then manually designating with a mouse click the location on the image that

the UAS should track. The airspeed and heading of the target were rebroadcast through the ground station to the seeker. The delay in passing the target data to the seeker was approximately 200 ms.

CHAPTER 3. AIR-TO-AIR RENDEZVOUS USING VECTOR FIELD METHODS

3.1 Introduction

This chapter presents a non vision-based air-to-air tracking method that is effective using the GPS position of the target vehicle to predict its elliptical flight path. By constructing a vector field based on the target path, the seeker can follow the target in loose formation flight. The method was developed as an interim step to gather in-flight video of the target vehicle and to evaluate the flight environment with respect to flight in close proximity to the target.

To track an orbiting drogue, estimates of the drogue orbit are needed. One factor that must be considered when using this method is that the accuracy is limited primarily by the resolution of GPS, our primary positioning sensor. GPS measurements do not provide sufficient accuracy to directly facilitate a rendezvous between the two vehicles. Additionally, wind and turbulence make aerial rendezvous of small UAS a difficult problem to solve in the real world [37]. Therefore, tracking the target along a known path gives additional information that can be used by the seeker to maintain a visual track on the target. This chapter couples vector-field path following with vision-based guidance to develop and demonstrate a method for tracking a target along an elliptical path.

Nelson, et al. showed how vector fields, rather than waypoints, can be used by a UAS for path following [14]. Lawrence, Frew and Pisano developed the construction of vector fields that can be used for UAS guidance around flat closed curves [15]. Gonçalves further developed this idea by demonstrating a method for construction of vector fields that allow a UAS to circulate around three-dimensional generic curves [16]. The vector field construction defined the desired flight path as the intersection of two surfaces. It has been shown that the method developed by Gonçalves can be used to produce vector fields that are effective in describing an inclined elliptical path that can be used by the seeker to follow the drogue at close range [33].

This chapter is organized with a description of the vector-field tracking method first, followed by vision-based enhancements to the vector-field approach. Experimental results using the vision-enhanced vector field rendezvous method are then produced and discussed.

3.2 Orbit Tracking Using Vector Fields

The method for constructing three-dimensional vector fields about a curved path is divided into two components: contraction towards the curve and circulation about the curve [16]. For the purposes of this dissertation, three-dimensional vector fields are produced that do not vary with time. Let the surfaces be described by the functions $\alpha_1(x_1,x_2,x_3)$ and $\alpha_2(x_1,x_2,x_3)$ with bounded second-partial derivatives. The curve of interest is defined as the set of all points that lie in the intersection of the level sets $\alpha_1 = 0$ and $\alpha_2 = 0$. This can be visualized by the intersection of a plane with a cylinder as shown in Figure 3.1.

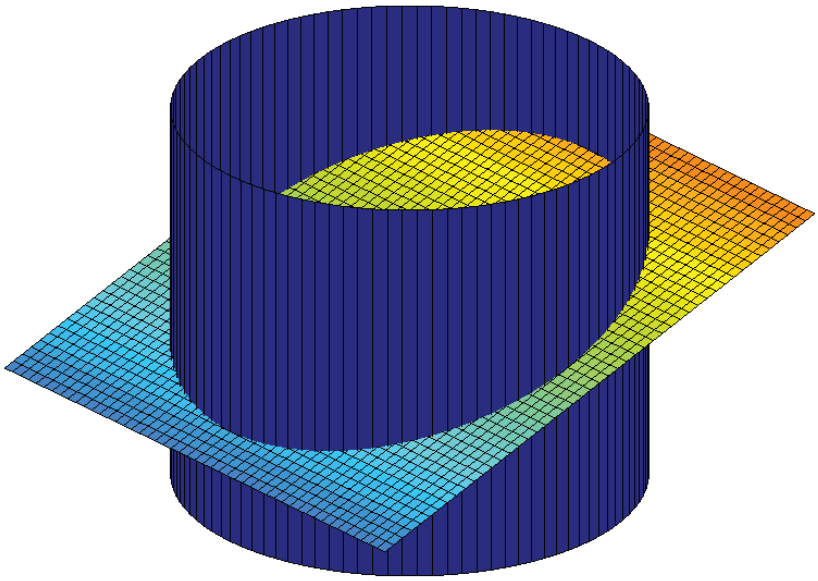

Figure 3.1: The intersection of two surfaces describes the zero-level set for the vector field. An elliptical flight path can be described by intersection of a cylinder and the $x_1 - x_2$ plane. The x_1 axis is aligned with the major radius of the ellipse (a), and the minor radius (b) is aligned with the x_2 axis.

We define a differentiable, positive-definite, scalar potential function $V(\alpha_1, \alpha_2)$, where $V = 0$ if and only if $\alpha_i = 0, i = 1,2$. Thus, the scalar function is zero only when evaluated on the curve.

Any function that meets these requirements can be used for V. The contraction term is described by the equation $u = -G\nabla V$ and the circulation term as $u = H(\nabla\alpha_1 \times \nabla\alpha_2)$ where $G(x_1, x_2, x_3)$ is a nonnegative diagonal matrix, $H(x_1, x_2, x_3)$ is a strictly positive or negative diagonal matrix, and $\times$ is the cross-product operator [16]. G and H are tunable gains that provide a mechanism for balancing the relative strengths of the convergence and circulation terms. The complete equation for time-invariant curves is

$$u = -G\nabla V + H(\nabla\alpha_1 \times \nabla\alpha_2). \tag{3.1}$$

This equation produces a 3x1 vector, u, containing velocity commands in each of the directions x_1, x_2 and x_3. The coordinate frame used for calculating the elliptical path is the ellipse frame. The origin of the ellipse frame is located at the orbit center which is a fixed location in the inertial frame. We define the ellipse frame with the x_1 and x_2 axes aligned with the major and minor ellipse axes respectively and the x_3 axis oriented perpendicular to the plane containing the ellipse. The inertial frame is also assumed to be at the origin of the ellipse frame so that all inertial positions and velocities are also referenced to the ellipse center. The combined 3-2-3 Euler rotation matrix for converting a vector in the north, east, down (NED) inertial frame for an arbitrarily oriented ellipse frame is written as

$$\mathbf{R}_e^i = \begin{pmatrix} \cos\psi_2 & \sin\psi_2 & 0 \\ -\sin\psi_2 & \cos\psi_2 & 0 \\ 0 & 0 & 1 \end{pmatrix} \begin{pmatrix} \cos\theta_1 & 0 & -\sin\theta_1 \\ 0 & 1 & 0 \\ \sin\theta_1 & 0 & \cos\theta_1 \end{pmatrix} \begin{pmatrix} \cos\psi_1 & \sin\psi_1 & 0 \\ -\sin\psi_1 & \cos\psi_1 & 0 \\ 0 & 0 & 1 \end{pmatrix}, \tag{3.2}$$

where the subscript i specifies that the rotation begins in the inertial frame and ends in the ellipse frame, indicated by the superscript e.

The selection of the ellipse frame simplifies the zero-level surface functions needed to define the ellipse we wish to follow. We describe the ellipse of interest with the appropriate cylinder and the plane containing the x_1 and x_2 axes. These zero-level surface functions as shown in Figure 3.1 can be expressed as

$$\alpha_1(x_1,x_2,x_3) = \left(\frac{x_1}{a}\right)^2 + \left(\frac{x_2}{b}\right)^2 - 1 \tag{3.3}$$

$$\alpha_2(x_1,x_2,x_3) = x_3. \tag{3.4}$$

The positive definite, scalar potential function $V(x_1,x_2,x_3)$ for the vector field construction of both curves was selected to be

$$V(x_1,x_2,x_3) = \frac{1}{2}\alpha_1^2 + \frac{1}{2}\alpha_2^2. \tag{3.5}$$

This is the simplest function that meets the criteria for the scalar potential function. It is now a straightforward procedure to construct the vector fields for each of the curves. Substituting these surface functions into (3.1) and evaluating yields

$$u = -G\begin{pmatrix} \frac{2x_1}{a^2}\left(\left(\frac{x_1}{a}\right)^2 + \left(\frac{x_2}{b}\right)^2 - 1\right) \\ \frac{2x_2}{b^2}\left(\left(\frac{x_1}{a}\right)^2 + \left(\frac{x_2}{b}\right)^2 - 1\right) \\ x_3 \end{pmatrix} + H\begin{pmatrix} -\frac{2x_2}{b^2} \\ \frac{2x_1}{a^2} \\ 0 \end{pmatrix}. \tag{3.6}$$

This vector field equation provides a velocity vector command in the ellipse frame. The velocity command is made up of a circulation component and a contraction component. These components can be tuned with a gain H which must be a strictly positive or strictly negative diagonal matrix. The sign of H determines the direction of circulation (e.g., clockwise or counter-clockwise). The matrix G can be tuned to control the relative strengths of the contraction force in the directions of the ellipse frame, but it must be a positive definite matrix. This matrix can be used to command a constant ground speed and can also be used to limit the commanded vertical velocity to be within the UAS performance constraints. The relative strength of the circulation and contraction terms in (3.6) are a function of the ellipse parameters a and b. This can cause gains from one ellipse to perform poorly on an ellipse of different dimension. Owen developed a method

for nondimensionalizing the ellipse parameters to minimize the need for gain tuning for orbits of different sizes [45].

Course and Flight Path Angle Commands

To produce guidance commands, the desired ellipse frame velocities are rotated into the inertial frame. This relationship is presented mathematically as

$$\begin{pmatrix} \dot{p}_n^d \\ \dot{p}_e^d \\ \dot{p}_d^d \end{pmatrix} = (\mathbf{R}_e^i)^{-1} u. \tag{3.7}$$

For fixed-wing aircraft there are basic kinematic equations that relate inertial velocities, the angles of travel in the horizontal and vertical directions, and what we define as ground speed. The angle between the north direction and the direction of travel in the horizontal plane we define as the course angle (χ). The angle between the magnitude of the vertical velocity and horizontal velocity in the inertial frame is defined as the flight path angle (γ). Using these relationships we first solve for the desired ground speed, then calculate the commanded course angle and flight path angles. These are calculated as

$$V_g^d = \sqrt{(\dot{p}_n^d)^2 + (\dot{p}_e^d)^2 + (\dot{p}_d^d)^2} \tag{3.8}$$

$$\gamma^c = \arcsin\left(-\frac{\dot{p}_d^d}{V_g^d}\right) \tag{3.9}$$

$$\chi^c = \arctan 2(\dot{p}_e^d, \dot{p}_n^d) \tag{3.10}$$

The angle between the north direction and the direction of travel in the horizontal plane is defined as the course angle (χ).

Roll Feed Forward

The nominal bank angle necessary for flying the predicted elliptical path is fed forward based on the coordinated turn assumption. Feeding forward the nominal roll angle significantly

reduces the steady-state error when tracking curved paths [46]. This is accomplished by computing a nominal roll angle command using the relationship

$$\phi_{nom} = \frac{\dot{\chi} V_g}{g}, \tag{3.11}$$

where $\dot{\chi}$ is the appropriate course angle rate, V_g is the vehicle ground speed, and g is the acceleration due to gravity. This nominal roll angle can be added to the roll angle command produced by the course angle hold loop. The value of $\dot{\chi}$ evolves according to the curve being followed. To follow elliptical orbits, we approximate the appropriate course-rate as

$$\dot{\chi} = \frac{V_g}{r_{eff}}, \tag{3.12}$$

where r_{eff} is the effective radius of the elliptical orbit that is to be followed. The effective radius of an elliptical orbit is computed as

$$r_{eff} = \frac{(a^2\sigma^2 + b^2\sigma^2)^{\frac{3}{2}}}{ab} \tag{3.13}$$

where a and b are the ellipse major and minor radii and σ is the parametric variable used to describe the angular position of the vehicle on the ellipse. This parametric relationship for an ellipse is represented as

$$x_1 = a\cos\sigma \tag{3.14}$$

$$x_2 = b\sin\sigma \tag{3.15}$$

and can be used to solve for σ given the vehicle position relative to the ellipse center.

Airspeed Control

Up to this point in this chapter, the equations for commanding ground speed V_g^d, flight path angle γ^c, course angle χ^c and a nominal roll angle ϕ_{nom} have been developed such that the seeker will remain on the same elliptical path as the target. The autopilot commands are provided in (3.8), (3.9), (3.10), and (3.11). It is also desired that the seeker maintain a set separation distance from the target while following the elliptical path of the target vehicle. Separation distance from the target is controlled by varying the seeker airspeed V_S^c. Seeker airspeed is controlled based upon the error in the desired distance behind the drogue. Distance measurement is computed based on the relative GPS positions of the target and seeker. Target position is relayed to the seeker through the ground station as shown in Chapter 2. Proportional control is used according to

$$V_S^c = V_g^d + K_p(d^c - d), \tag{3.16}$$

where K_p is a proportional gain and $d^c - d$ the horizontal error between the desired following distance and the current distance behind the drogue. The horizontal distance d between the seeker and the drogue is computed using the GPS position data from the drogue.

3.3 Vision-based Enhancements to Orbit Tracking Using Vector Fields

It was found that the vector-field following method could be improved by the use of vision information when available. This section describes two methods that improved the capability to keep the target vehicle in the field of view of the camera and that provided a correction for GPS altitude differences between the two air vehicles.

3.3.1 Interior Orbit Following for Improved Vehicle Tracking

An enhancement to the vector field method for following the drogue orbit was developed to aid in keeping an ungimballed camera on the seeker pointed at the center of drogue. If the seeker follows the drogue on the same orbit, the drogue will continually be on the edge or even out of the camera field of view (FOV). For the seeker camera to be centered on the drogue, its inertial

velocity vector must be pointed at the drogue. Figure 3.2 shows how this is done. In the horizontal plane, this is accomplished by adjusting the seeker orbit radius so that the line running from the seeker through the center of the orbit is perpendicular to the line running from the seeker through the drogue. Since the desired separation distance d is given, the interior orbit radius R_2 can be calculated using the Pythagorean Theorem. In the vertical direction, the altitude of the seeker must be adjusted to account for the seeker angle of attack.

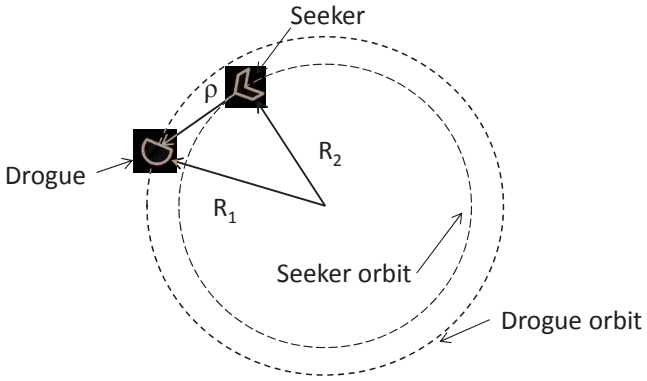

(a)

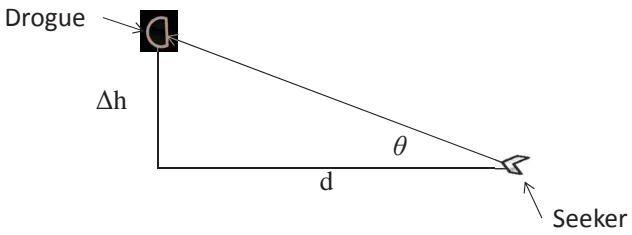

(b)

Figure 3.2: (a) Plan View: drogue and seeker flying counter-clockwise orbits, d is the horizontal distance between seeker and drogue, R_1 is the drogue orbit radius, and R_2 is the seeker orbit radius; (b) Vertical View: Δh is the seeker altitude difference from drogue altitude, and θ is the seeker pitch angle (rad).

The drogue is assumed to be pulled by a mothership flying in a circular orbit. In the presence of wind, the drogue orbit will become an inclined ellipse. However, for the purposes of pointing the seeker camera at the drogue, the orbit of the drogue is assumed to be instantaneously circular. The drogue position and airspeed are broadcast to the seeker through the ground station.

The drogue orbit radius is calculated based upon its position relative to the orbit centroid and the angular velocity are calculated onboard the seeker according to $\omega = V_D/R_1$.

For a desired horizontal distance behind the drogue d^c, the seeker must calculate the orbit radius R_2, desired airspeed V_S^c, and desired altitude h_S^c. The desired orbit radius is calculated according to

$$R_2 = \sqrt{R_1^2 - d^2}. \tag{3.17}$$

R_2 is substituted for a and b in the vector-field equations as described in Section 3.2. The position behind the drogue is maintained by proportionally controlling V_S based on the difference between the desired position and the actual position according to (3.16) where $R_2\omega$ is substituted for V_S^c.

The commanded altitude to keep the camera centered is computed based on the actual horizontal separation distance behind the drogue d and the pitch angle of the seeker θ according to

$$\Delta h = d(\tan(\theta)) \tag{3.18}$$

$$h_S^c = h_D - \Delta h, \tag{3.19}$$

where h_S^c is the commanded altitude for the seeker and h_D is the drogue altitude.

3.3.2 Altitude Bias Correction Using Vision

GPS information alone for determining position and altitude is not adequate for air-to-air docking. Even when the two vehicles are flying at the same commanded altitude they will often not physically be at the same altitude due to the error in the GPS altitude measurements. GPS accuracy without selective availability enabled is 4.6 m spherical error probable [47]. This means that two UAS flying side by side, one with the average altitude error in the positive direction and the other with the average error in the negative direction, could have a difference in perceived altitude of 9.2 m. Of course, this altitude error could also be much more. For this reason it is advantageous

to supplement the GPS altitude information with a vision-based correction when available. The vision data acquired from even short periods of tracking is useful for estimating the bias between the two GPS units.

We now present a method that is used to calculate a GPS bias between the two vehicles and then allow the seeker to apply that bias to the estimated target altitude to reduce the relative altitude error. This is done by using the camera onboard the seeker or trailing UAS. The reference frames used in this method follow the frames described by Beard and McLain [13]. The inertial frame is a NED frame with the origin at the center of the target orbit. The vehicle-1 frame is obtained by aligning the axes with the inertial frame and rotating the frame according to the heading the aircraft is flying. Since the vision commands are relative, the actual heading is not important to the solution and therefore the image information rotated into the vehicle-1 frame is the primary reference frame. That way image information can be used to provide control inputs to the seeker.

The camera is assumed to be located at the center of gravity of the seeker and aligned with the body frame as shown in Figure 3.3. Using computer vision convention, the i^{Im} axis points to the right and the j^{Im} axis points down in the image. The k^{Im} axis points out the front of the camera along the optical axis.

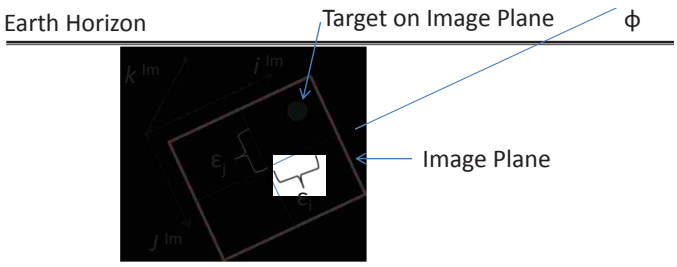

Figure 3.3: Camera image frame. seeker is pitched down and rolled to an angle ϕ. The distance of the target from the center of the image frame is specified by ε_i and ε_j.

The rotation matrix that will take the image data from the body frame to the vehicle-1 frame is found by rotating the body frame through the roll angle ϕ and pitch angle θ of the seeker. The rotation matrix from the image frame to the vehicle-1 frame is

$$\mathbf{R}_{Im}^{V_1} = \begin{bmatrix} \sin\phi\sin\theta & \cos\phi\sin\theta & \cos\theta \\ \cos\phi & -\sin\phi & 0 \\ \sin\phi\cos\theta & \cos\phi\cos\theta & -\sin\theta \end{bmatrix}.$$

Using these reference frames, an altitude bias correction can be calculated by using the location of the drogue in the image frame and rotating this into the vehicle-1 frame. This is given by

$$\varepsilon^{V_1} = \mathbf{R}_{Im}^{V_1}\varepsilon^{Im}. \tag{3.20}$$

The pixel location of the drogue in the vehicle-1 frame is ε^{V_1} The component $\varepsilon_j^{V_1}$ is used in calculating the difference in altitude between the two vehicles. The difference in altitude is

$$\Delta h = \varepsilon_j^{V_1}\frac{d}{f} + d\tan\theta, \tag{3.21}$$

where d is the horizontal GPS-based distance between the two vehicles, f is the camera focal length and θ is the pitch angle of the vehicle. The altitude bias is then calculated by comparing the difference between the drogue and seeker altitude and the vision-measured altitude difference according to

$$h_{bias} = (h_D - h_S) - \Delta h. \tag{3.22}$$

As the seeker approaches the drogue and the drogue becomes visible in the image frame, the operator is able to initiate a track on the drogue. The vision data acquired from even short periods of tracking is useful for calculating the GPS altitude bias between the two GPS units. The altitude bias is then subtracted from all drogue GPS altitude updates that are received. The bias remains active until another track is initiated or the bias is manually zeroed.

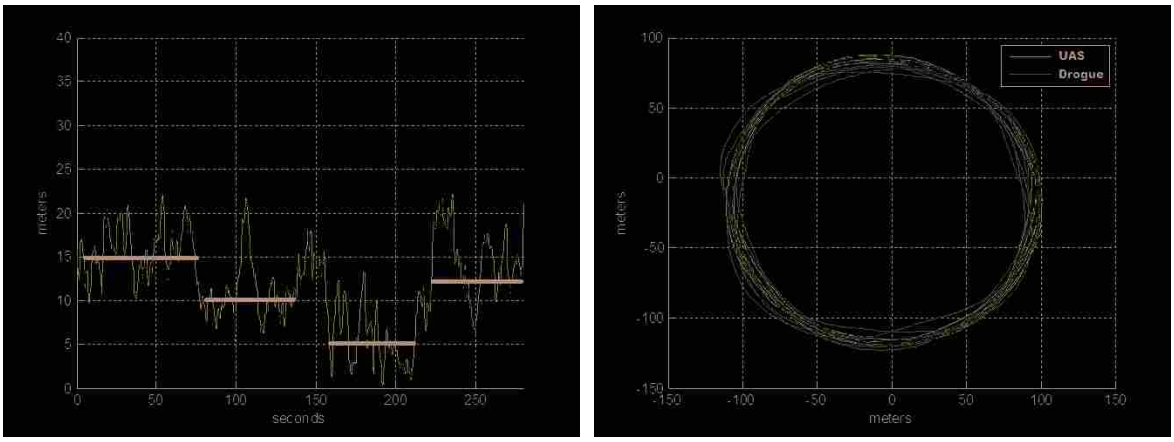

(a) (b)

Figure 3.4: (a) Separation distance between seeker and drogue while the seeker was estimating the drogue path and calculating vector field path commands. The commanded separation distance is indicated by the solid bar; (b) Drogue and seeker flight paths over 270 second period.

3.4 Experimental Results

The ability to follow another aerial vehicle and remain in flight formation with it was demonstrated by flying the mothership and drogue in a circular orbit and then using the vector-field algorithms programmed onto the VPU to estimate the drogue orbit and create the real-time path for the seeker to follow. Figure 3.4(a) contains the results of this test. The seeker was commanded to follow the drogue at several following distances between 5 and 15 m at an altitude of 100 m above terrain level. The seeker was able to adjust the distance behind the drogue according to the commands with a variation about the intended follow distance of about 5 m. It can be seen in Figure 3.4(b) that the seeker was able to successfully follow the drogue orbit. Tracks are displayed for the horizontal plane during a time segment of 270 s.

The vision-based altitude bias correction was effective whenever a visual track could be initiated. This was tested by commanding both vehicles to fly at the same altitude. Prior to initiating the track, the target vehicle was observed to be flying above the seeker and about 15 m in front. After initiating the track, the seeker applied a bias correction of 7 m to the target altitude and the seeker was observed visually to correct its flight path to fly at nearly the same altitude as the target vehicle. The test was repeated a number of times with altitude bias corrections of between

2 and 7 m both above and below the target vehicle. In each case the seeker made the appropriate correction and improved the location of the target vehicle in the seeker camera field of view.

An experiment was conducted to compare the performance of the vision-based enhancements to the basic vector-field following method. For this test, the seeker was commanded to follow the mothership rather than the drogue. Figure 3.5 shows a frame from the VPU camera on the seeker aircraft. This is the view that the operator has while observing the target and initiating a track on the target vehicle.

Figure 3.5: Video frame from seeker camera.

Using the interior orbit-following method and correcting for GPS altitude differences between aircraft resulted in a significant improvement in the ability of the seeker to keep the target in the camera field of view. For example by reviewing the VPU video we determined that prior to using the vision enhancements, the very best performance demonstrated was the ability to keep the target in the field of view 80 percent of the time over a single orbit. Typical orbit duration for a 100 m radius orbit was about 40 s. With the vision enhancements implemented we were successfully able to keep the target in the field of view on average 91 percent of the time.

Figure 3.6 depicts a comparison of the tracking performance of the interior-orbit and altitude bias adjusted guidance method compared to the baseline method. For both cases the seeker was commanded to follow the target vehicle at a distance of 30 m and at the same altitude.

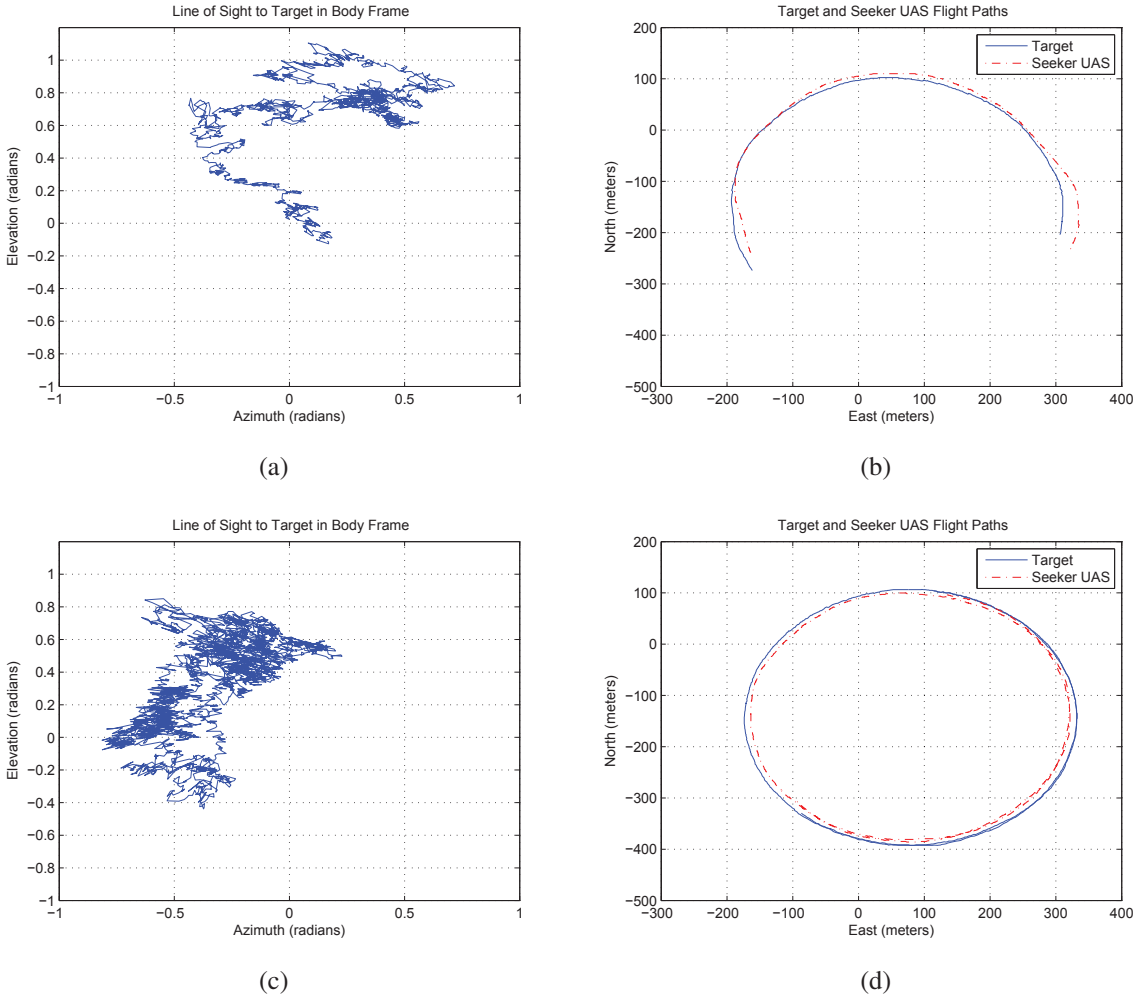

Figure 3.6: (a) LOS error to the target vehicle based on GPS position for seeker vehicle using vector-field ellipse following; (b) Seeker and target flight paths for vector-field ellipse following case. (c) LOS error to the target vehicle based on GPS position for seeker vehicle using vector-field ellipse following with interior orbit and altitude bias enhancement; (d) Seeker and target flight paths for the vision enhanced vector-field ellipse following case.

In Figure 3.6(d) the seeker path, when following the interior orbit commands, can be seen to be inside the target orbit. A comparison of the line-of-sight angle errors can be seen in Figure 3.6(a) and (c). It was found that the mean line-of-sight error for the baseline method was 41.3 deg and

for the interior orbit-enhanced method the mean line of sight error was 32.7 deg. This was an improvement of 20 percent over the baseline method. It can be seen that the elevation LOS errors are reduced, when using the altitude bias correction, indicating a reduced altitude error between the two aircraft. Lateral LOS errors are also reduced when using the interior orbit enhancement to the vector-field path following method.

3.5 Chapter Summary

In this chapter we have developed a non-vision-based method for flying two UAS in formation. We have shown how a three-dimensional flight path can be constructed from the intersection of two surfaces and how that flight path can be converted into a vector field that provides course angle and flight path angle commands to a UAS. Using proportional control for airspeed we have shown experimentally that this vector-field construction can be used to follow an airborne target to within about ± 5 m from a designated follow distance. We have developed a modification to the vector-field method to keep the flight-path vector pointed at the target vehicle and also a method to compensate for GPS altitude error between two UAS if vision data is available on the seeker.

CHAPTER 4. VISUAL PURSUIT

4.1 Introduction

When considering air-to-air rendezvous and docking, an obvious place to start is with air-to-air missile guidance. After all, tactical missiles have demonstrated the ability to track and hit a maneuvering aircraft with great consistency. The basis for many missile guidance systems is proportional navigation. This method was derived from naval navigation where it was learned that if two moving vessels keep the same line of sight angle between them, they will eventually collide [38]. Fighter pilots use a similar rule of thumb in aerial combat to ensure they do not collide with the other aircraft. This rule is that if the other aircraft is not moving on the canopy, the two aircraft are on a collision course [48]. Proportional navigation might work well for aerial docking if the aspect angle at which the seeker strikes the drogue was unimportant. However, for successful docking, it is important to approach the drogue from directly behind with wings relatively level. Another guidance method that is sometimes used in missile guidance is pursuit. Pursuit is similar to the way animal predators stalk and attack their prey [38]. A predators will keep the prey centered in its line of sight which, for pursuits of any significant length, will result in an attack from directly behind. Figure 4.1 shows the differences between proportional navigation and pursuit guidance methods when attempting aerial docking.

In both cases, the target aircraft is flying at a constant bank angle. In the proportional navigation case, the lateral LOS angle η between the seeker and the target remains constant throughout the docking engagement. In the pursuit case, the seeker velocity vector remains pointed at the target or in other words η remains zero throughout the docking engagement. Since our objective is to approach the drogue from directly behind it, the guidance methods developed in this chapter will be based upon pursuit, or the principle of driving the line of sight angle to zero, or to a region around $\eta = 0$.

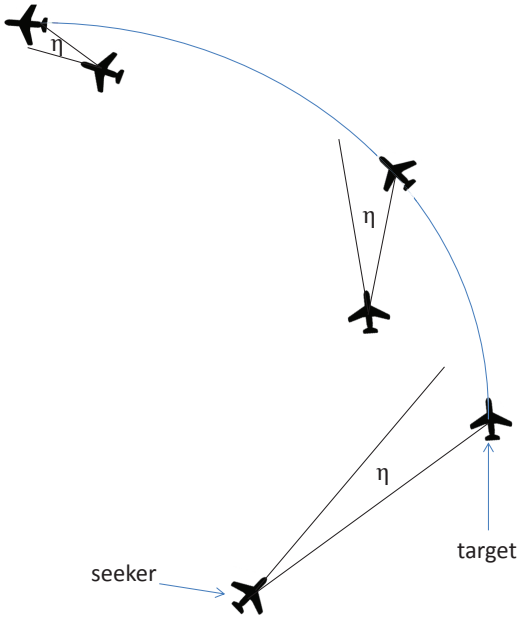

(a)

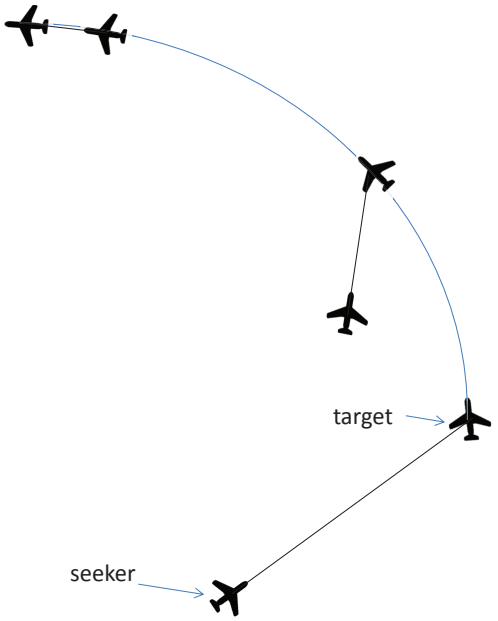

(b)

Figure 4.1: (a) Proportional navigation guidance; (b) Pursuit guidance.

4.2 Model Development

In this section guidance models that allow the seeker to follow a target aircraft or drogue are developed. Figure 4.2 is an example of two small UAS flying in formation using a pursuit guidance method.

Figure 4.2: Seeker and target in formation flight.

4.2.1 Coordinate Frames

The inertial, body, camera, and line-of-sight (LOS) frames are the primary coordinate frames referenced in the development of the visual pursuit method. The frames are referenced according the convention laid out in [13]. The inertial coordinate system is an earth-fixed coordinate system with its origin at the defined home location. It is oriented such that north is defined as the 0 radian heading direction, east as the $\frac{\pi}{2}$ radian heading direction and the altitude reference of positive direction being down. The body frame is obtained from the inertial frame by moving the origin to the center of mass of the seeker and then rotating the coordinate axes through the yaw or heading ψ. The aircraft is then rotated through the pitch θ and roll ϕ angles such that the x-axis runs from the center of mass along the centerline of the seeker and out the nose, the y-axis runs from the center of center of mass out the right wing perpendicular to the x-axis and the z-axis runs from the center of mass through the bottom of the seeker perpendicular to the x and y axes. The camera frame is located at the image plane of the camera with the axes aligned with the body

frame such that the camera frame i^{Im} axis is aligned with the body-frame y-axis and j^{Im} is aligned with the body-frame z-axis as shown in Figure 4.3. The LOS frame of reference is aligned with the line-of-sight vector ρ and is formed by rotating the body frame through the azimuth η and elevation β angles.

4.2.2 Camera Geometry

The seeker is assumed to have a fixed camera aligned with the body-x axis and located at the center of gravity of the aircraft. It is expected that the UAS has an autopilot with inner control loops to command pitch rate, roll angle and airspeed. It is further assumed that the control responses can be generated infinitely fast. Lateral commands originate with the horizontal distance of the target on the image plane from the center of the image. Longitudinal commands derive from the vertical distance of the target image from the center of the image as shown in Figure 4.3. Pixel

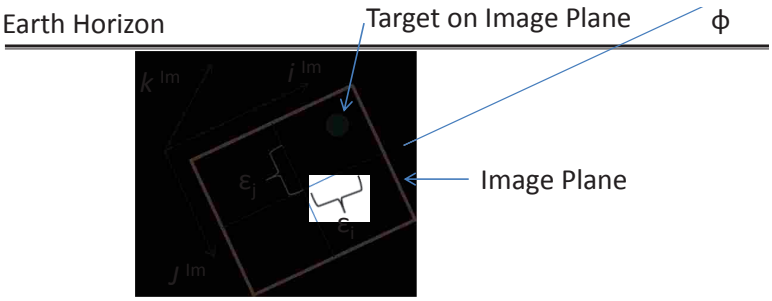

Figure 4.3: Seeker camera frame. UAS is pitched down and rolled to an angle ϕ. The distance of the projection of the target on the image frame from the center of the image frame is specified by ε_i and ε_j.

distances are converted to elevation (β) and azimuth (η) LOS angles in the body frame according to

$$\beta = \tan^{-1}\left(\frac{\varepsilon_j}{f}\right) \tag{4.1}$$

$$\eta = \tan^{-1}\left(\frac{\varepsilon_i}{f}\right) \tag{4.2}$$

where f is the focal length of the camera.

4.2.3 System Dynamics

The relative dynamics between the seeker and the drogue can be visualized in the lateral and longitudinal planes. The longitudinal dynamics are shown in the pitch plane by projecting the inertial y-axis onto the inertial x and z-axes as shown in Figure 4.4. The relative lateral dynamics between the seeker and the drogue are shown by projecting the inertial z-axis onto the inertial x and y-axes as shown in Figure 4.5.

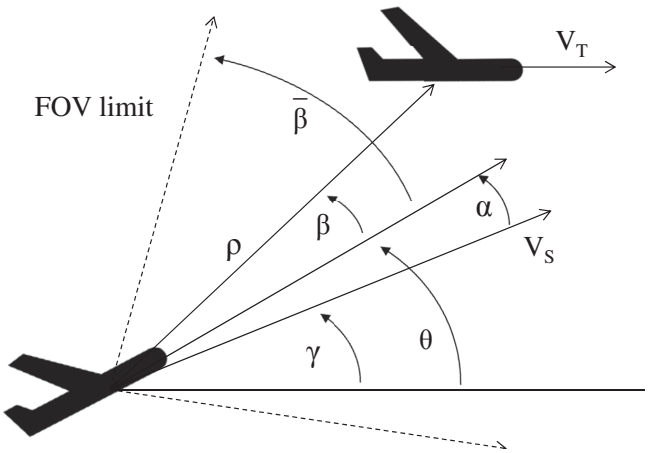

Figure 4.4: Longitudinal dynamics, where β is the angle between the seeker pitch angle θ and the longitudinal LOS vector; $\boldsymbol{\rho}$ is the LOS vector; and the angle $\bar{\beta}$ is the maximum FOV angle. The LOS frame of reference is aligned with the LOS vector $\boldsymbol{\rho}$.

Let $\mathbf{v}_S$ and $\mathbf{v}_T \triangleq (V_x^i, V_z^i, V_z^i)^T \in \mathbb{R}^3$, where $\mathbf{v}_S$ is the seeker velocity vector and $\mathbf{v}_T$ is the target velocity vector. The target vehicle is assumed to be flying at a constant altitude. The time rate of change of the LOS vector $\boldsymbol{\rho}$ in the inertial frame is computed by taking the vector difference of the target and seeker velocities according to

$$\dot{\boldsymbol{\rho}}^i = \mathbf{v}_T - \mathbf{v}_S, \tag{4.3}$$

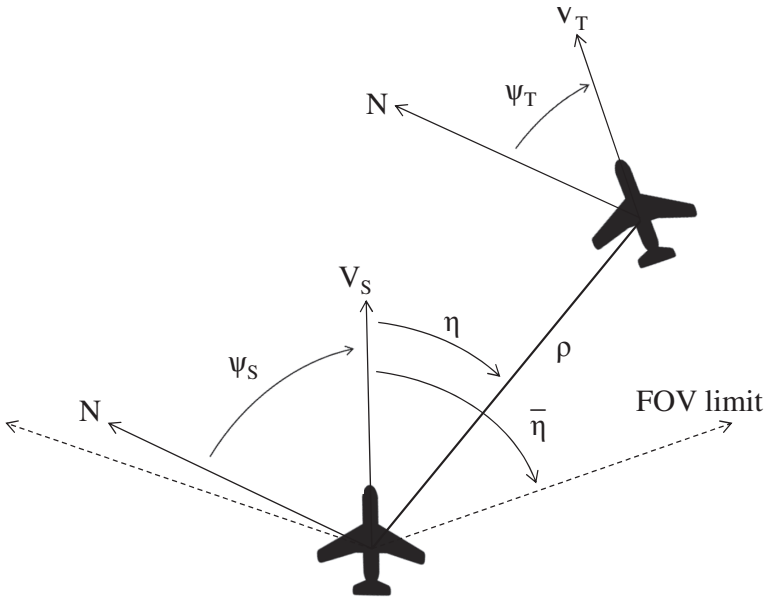

Figure 4.5: Lateral dynamics, where η is the angle between the seeker heading and the line-of-sight vector; $\boldsymbol{\rho}$ is the LOS vector between the seeker and the target; $\bar{\eta}$ is the maximum FOV angle; and the angles ψ_S, and ψ_T are the seeker and target headings.

where,

$$\mathbf{v}_T = \begin{bmatrix} V_T \cos\gamma \cos\psi_T \\ V_T \cos\gamma \sin\psi_T \\ 0 \end{bmatrix} \tag{4.4}$$

$$\mathbf{v}_S = \begin{bmatrix} V_T \cos\gamma \cos\psi_S \\ V_T \cos\gamma \sin\psi_S \\ V_S \sin\gamma \end{bmatrix}. \tag{4.5}$$

The target is assumed to be flying at a constant altitude. To rotate the LOS rate vector from the inertial frame into the line-of-sight frame requires a rotation about the body-y and body-z axes according to

$$\mathbf{R}_\mathbf{i}^{\mathbf{LOS}} = \mathbf{R}_\mathbf{y}\mathbf{R}_\mathbf{z}, \tag{4.6}$$

where

$$\mathbf{R}_\mathbf{y} = \begin{bmatrix} \cos(\theta+\beta) & 0 & -\sin(\theta+\beta) \\ 0 & 1 & 0 \\ \sin(\theta+\beta) & 0 & \cos(\theta+\beta) \end{bmatrix}, \tag{4.7}$$

and

$$\mathbf{R_z} = \begin{bmatrix} \cos(\psi_S+\eta) & \sin(\psi_S+\eta) & 0 \\ -\sin(\psi_S+\eta) & \cos(\psi_S+\eta) & 0 \\ 0 & 0 & 1 \end{bmatrix}. \tag{4.8}$$

The LOS rate, expressed in the LOS frame, can be written as

$$\dot{\boldsymbol{\rho}}^{LOS} = \mathbf{R_i^{LOS}}\dot{\boldsymbol{\rho}}^{\mathbf{i}} \tag{4.9}$$

$$= \begin{bmatrix} (V_T\cos(\psi_S-\psi_T+\eta)-V_S\cos\eta)\cos\gamma\cos(\beta+\theta)+V_S\sin(\beta+\theta)\sin\gamma \\ -(V_T\sin(\psi_S-\psi_T+\eta)-V_S\sin\eta)\cos\gamma \\ (V_T\cos(\psi_S-\psi_T+\eta)-V_S\cos\eta)\cos\gamma\sin(\beta+\theta)-V_S\cos(\beta+\theta)\sin\gamma \end{bmatrix}. \tag{4.10}$$

In the LOS frame, the radial and tangential components in the lateral and longitudinal directions are defined as

$$\dot{\boldsymbol{\rho}}^{LOS} \triangleq \begin{bmatrix} \dot{\rho}_r \\ \dot{\rho}_{lat} \\ \dot{\rho}_{lon} \end{bmatrix}. \tag{4.11}$$

From the dynamics shown in Figures 4.4 and 4.5, using the LOS frame, the change in the LOS vector in the radial direction $\dot{\rho}$, lateral tangential direction $\dot{\rho}_{lat}$, and the longitudinal tangential direction $\dot{\rho}_{lon}$ can be expressed as

$$\begin{bmatrix} \dot{\rho}_r \\ \dot{\rho}_{lat} \\ \dot{\rho}_{lon} \end{bmatrix} = \begin{bmatrix} \dot{\rho} \\ \rho(\dot{\psi}_S+\dot{\eta}) \\ \rho(\dot{\theta}+\dot{\beta}) \end{bmatrix}. \tag{4.12}$$

Combining the relationships in (4.10) and (4.12) and rearranging, the expressions for the change in the LOS distance $\dot{\rho}$ and the rate of change of the LOS angles $\dot{\eta}$ and $\dot{\beta}$ are written as

$$\dot{\rho} = (V_T \cos(\psi_S - \psi_T + \eta) - V_S \cos\eta)\cos\gamma\cos(\beta+\theta) + V_S \sin(\beta+\theta)\sin\gamma, \tag{4.13}$$

$$\dot{\eta} = -\dot{\psi}_S + \frac{1}{\rho}\left[-(V_T \sin(\psi_S - \psi_T + \eta) - V_S \sin\eta)\cos\gamma\right], \tag{4.14}$$

$$\dot{\beta} = -\dot{\theta} + \frac{1}{\rho}\left[(V_T \cos(\psi_S - \psi_T + \eta) - V_S \cos\eta)\cos\gamma\sin(\beta+\theta) - V_S \cos(\beta+\theta)\sin\gamma\right], \tag{4.15}$$

where V_T is constant. The target heading ψ_T is not controlled nor restricted explicitly. However, it is assumed that the target or drogue is cooperating and will not make evasive maneuvers. Since seeker follows the target, ψ_S follows ψ_T, and the quantity $\psi_S - \psi_T$ remains bounded. This will be shown for a typical maneuver later. There are two additional state variables that must be considered, heading angle ψ_S and pitch angle θ. The time rate of change of ψ_S is found using the equation for a coordinated turn [13], which is expressed as

$$\dot{\psi}_S = \frac{g}{V_S}\tan\phi, \tag{4.16}$$

where ϕ is the seeker bank angle. Using the convention of Beard and McLain [13], the time rate of change of the pitch angle θ evolves in terms of angular positions and body rates according to

$$\dot{\theta} = q\cos\phi - r\sin\phi, \tag{4.17}$$

where q is the pitch rate and r is the yaw rate, which can be expressed as

$$r = \frac{\dot{\psi}_S - q\sin\phi\sec\theta}{\cos\phi\sec\theta}. \tag{4.18}$$

Using the relationships for $\dot{\psi}_S$ in (4.16) and r in (4.18), (4.17) becomes

$$\dot{\theta} = q(\cos\phi + \tan\phi\sin\phi) - \frac{g}{V_S}\tan\phi\cos\theta. \tag{4.19}$$

It is recognized that the dynamics of ψ_S and θ are hidden in the development of visual pursuit. The hidden dynamics are assumed to be well behaved for the purposes of model development.

This will be shown to be true empirically later in the dissertation. The control variables will be V_S, ϕ, and q.

4.3 Guidance Methods

Two guidance methods are developed for the seeker. The objective is to develop methods that will ensure that once the target has been captured in the camera FOV, the guidance methods will keep the target in the FOV. The first method is a proportional-integral method that uses only LOS angles β and η to compute autopilot commands θ^c and ϕ^c. The second method is nonlinear and is constructed using a Lyapunov function coupled with the relative system dynamics using the relationships in (4.13), (4.14) and (4.15) to compute q^c, ϕ^c and V_S^c.

4.3.1 Proportional-Integral Pursuit

Proportional-integral control is based on pure pursuit which requires that the seeker vehicle point its velocity vector so that it coincides with LOS vector [38]. To control the seeker in the lateral direction or azimuth, we command the roll angle ϕ such that we minimize the lateral LOS angle η. We use a proportional/integral (PI) controller to produce a commanded roll angle ϕ^c according to

$$\phi^c = K_{p_\phi}\eta(t) + K_{i_\phi}\int_0^t \eta(\tau)\,\mathrm{d}\tau. \tag{4.20}$$

Similarly for the longitudinal case, we minimize the longitudinal LOS angle or elevation β by controlling the pitch angle θ through PI control of θ^c according to

$$\theta^c = K_{p_\theta}\beta(t) + K_{i_\theta}\int_0^t \beta(\tau)\,\mathrm{d}\tau. \tag{4.21}$$

Airspeed is regulated using proportional control according to

$$V_S^c = V_T - K_V(\rho^d - \rho), \tag{4.22}$$

where ρ^d is the desired following distance, and ρ is the actual separation distance between the seeker and the target aircraft. PI control is a common method used for many dynamic systems. While this method was shown to work well in actual flight experiments, it does not guarantee mathematically that the target will remain within the camera field of view.

4.3.2 Visual Pursuit

The goal is to develop a guidance method that guarantees convergence of the lateral and longitudinal LOS angles to the center of the image frame while the seeker distance to the target may be changing. In other words in the longitudinal direction, we want to develop a function that produces control inputs that will drive the longitudinal LOS angle β to zero while the seeker is closing or retreating with respect to the target, or following at a set distance. In the lateral direction, rather than drive η to zero, η should converge to a region around the center of the image, but not necessarily the image center. This relaxation in the lateral direction will be shown to improve performance in wind and still guarantee convergence of the LOS angles to a region within the camera image.

It is assumed for the purposes of model development that field-of-view (FOV) refers to the largest circular region that can be inscribed inside the rectangular image frame. This means that an object in the corners of the image may be visible but not considered in the FOV because it is not inside the inscribed circular region. This assumption is necessary because the model developed in this section ensures that once captured within a circular region, the target will remain within this region.

Bank angle ϕ^c, pitch rate q^c, and seeker airspeed V_S^c are the control inputs as shown in the system block diagram in Figure 4.6. There are physical limitations on our control variables ϕ^c, q^c, and V_S^c. For example, there is an upper and lower airspeed limit for the seeker. There are also limits on bank angle and pitch rate that the aircraft may not exceed. The following guidance method is developed and proved to be stable provided the seeker does not saturate the aircraft controls for airspeed, pitch rate or bank angle.

Since the guidance method is an outer guidance loop that wraps around a higher bandwidth inner autopilot control loop we assume that the commanded guidance inputs ϕ^c and q^c track the instantaneous roll and pitch rate for the purpose of proving stability of the methods. We now

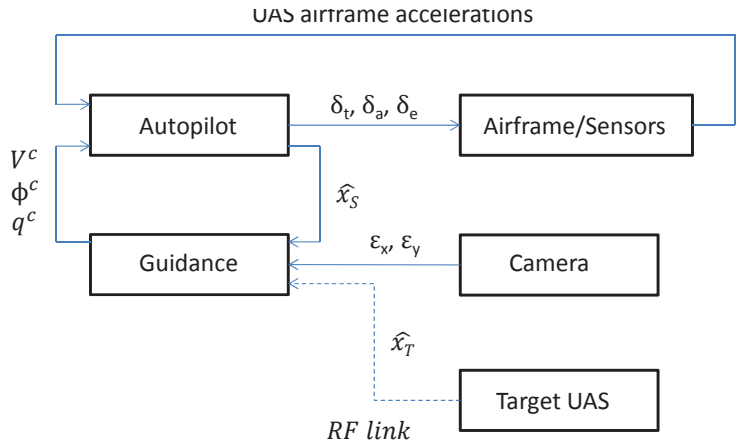

Figure 4.6: Control system block diagram.

develop a Lyapunov function based on ρ, η and β that will guide the selection of values for V_S, ϕ^c and q^c that will be convergent about the center of the image. Consider the Lyapunov function

$$\mathbf{W} = \underbrace{\frac{1}{2}\beta^2}_{\mathbf{W}_1} + \underbrace{\frac{1}{2}\eta^2}_{\mathbf{W}_2} + \underbrace{\frac{1}{2}\rho^2}_{\mathbf{W}_3}. \tag{4.23}$$

Differentiating the function with respect to time yields

$$\dot{\mathbf{W}} = \underbrace{\beta\dot{\beta}}_{\dot{\mathbf{W}}_1} + \underbrace{\eta\dot{\eta}}_{\dot{\mathbf{W}}_2} + \underbrace{\rho\dot{\rho}}_{\dot{\mathbf{W}}_3}. \tag{4.24}$$

For the system to be stable, or in other words to ensure that the target will remain within the FOV, $\dot{\mathbf{W}}$ must remain negative at all times [49]. This is accomplished by ensuring that each of the subterms $\dot{\mathbf{W}}_1$, $\dot{\mathbf{W}}_2$ and $\dot{\mathbf{W}}_3$ remain negative. The value of each subterm is respectively a function of pitch rate q^c, roll angle ϕ^c and seeker airspeed V_S^c. Each will be addressed in turn.

Longitudinal Guidance

Beginning with the subterm $\dot{\mathbf{W}}_1$ from (4.24) and substituting (4.15) for $\dot{\beta}$ we see that

$$\begin{aligned}\dot{\mathbf{W}}_1 &= \beta\dot{\beta} \\ &= \beta\left[-\dot{\theta}+\frac{1}{\rho}\left(\left(V_T\cos(\psi_S-\psi_T+\eta)-V_S\cos\eta\right)\cos\gamma\sin(\beta+\theta)-V_S\cos(\beta+\theta)\sin\gamma\right)\right].\end{aligned} \tag{4.25}$$

Using (4.19) for $\dot{\theta}$, the commanded pitch rate q^c is selected such that the nonlinear terms in (4.25) are zero according to

$$q^c = \frac{\left[\frac{1}{\rho}\left(\left(V_T\cos(\psi_S-\psi_T+\eta)-V_S\cos\eta\right)\cos\gamma\sin(\beta+\theta)-V_S\cos(\beta+\theta)\sin\gamma\right)+\frac{g\tan\phi\cos\theta}{V_S}+K_\theta\beta\right]}{\cos\phi+\tan\phi\sin\phi}, \tag{4.26}$$

and substituting back into (4.25), the scalar subterm becomes

$$\dot{\mathbf{W}}_1 \;=\; -K_\theta\beta^2. \tag{4.27}$$

If the gain K_θ is chosen to be positive, $\dot{\mathbf{W}}_\mathbf{1}$ is always negative which ensures that while using (4.26) for q^c, the target location in the camera FOV will longitudinally move toward the center of the image.

Lateral Guidance

Beginning with the subterm $\dot{\mathbf{W}}_2$ from (4.24) and substituting (4.14) for $\dot{\eta}$ we see that

$$\begin{aligned}\dot{\mathbf{W}}_2 &= \eta\dot{\eta} \\ &= \eta\left[-\dot{\psi}_S+\frac{1}{\rho}\left(-\left(V_T\sin(\psi_S-\psi_T+\eta)-V_S\sin\eta\right)\cos\gamma\right)\right].\end{aligned} \tag{4.28}$$

Using the expression for a coordinated turn from (4.16),

$$\dot{\psi}_S \;=\; \frac{g}{V_S}\tan\phi, \tag{4.29}$$

the expression for $\dot{\mathbf{W}}_2$ can now be written as a function of bank angle ϕ according to

$$\dot{\mathbf{W}}_2 = \eta \left[-\frac{g}{V_S} \tan\phi + \frac{1}{\rho} \left(-(V_T \sin(\psi_S - \psi_T + \eta) - V_S \sin\eta) \cos\gamma \right) \right]. \tag{4.30}$$

The lateral control must support two objectives, aerial tracking and aerial docking. Using bank angle command ϕ^c, the lateral control can be tailored for each purpose.

Lateral Command for Docking

For docking, it is desirable that the seeker LOS be pointed directly at the drogue such that at contact the seeker body-x axis is nearly perpendicular with the face of the drogue. The commanded bank angle ϕ^c is selected such that the nonlinear terms in (4.30) are zero according to

$$\phi^c = \tan^{-1} \left[\frac{V_S}{g} \left(\frac{1}{\rho} \left(-(V_T \sin(\psi_S - \psi_T + \eta) - V_S \sin\eta) \cos\gamma \right) + K_\phi \eta \right) \right] \tag{4.31}$$

and substituting back into (4.30), the scalar subterm becomes

$$\dot{\mathbf{W}}_2 \quad = \quad -K_\phi \eta^2. \tag{4.32}$$

If the gain K_ϕ is chosen to be positive, $\dot{\mathbf{W}}_\mathbf{2}$ is always negative which ensures that while using (4.31) for ϕ^c, the target location in the camera FOV will laterally move toward the center of the image plane.

Lateral Command for Tracking

Winds in the small UAS flight environment are often the dominant environmental factor to overcome when performing maneuvers requiring precision guidance. To accommodate high cross winds when tracking an airborne target, the lateral guidance has been extended in a way that preserves the desirable stability features and drives the target to a stable region of the image frame, but not necessarily to the center of the image. This is accomplished by adding $K_\phi \eta - \nu$ to the

commanded roll angle ϕ^c such that the nonlinear terms in (4.30) are zero according to

$$\phi^c = \tan^{-1}\left[\frac{V_S}{g}\left(\frac{1}{\rho}\left(-(V_T\sin(\psi_S-\psi_T+\eta)-V_S\sin\eta)\cos\gamma\right)+K_\phi\eta-\nu\right)\right] \tag{4.33}$$

and substituting back into (4.30), the scalar subterm becomes

$$\dot{\mathbf{W}}_2 \;=\; -K_\phi\eta^2+\eta\nu. \tag{4.34}$$

For $\dot{\mathbf{W}}_2$ to remain negative,

$$|\nu| \;<\; K_\phi\eta. \tag{4.35}$$

From (4.34), and observing the constraint in (4.35) and choosing K_ϕ to be positive, $\dot{\mathbf{W}}_\mathbf{2}$ is always negative. This means that while using (4.33) for ϕ^c, the target location in the camera FOV will laterally move toward a region around the center of the image. When the slack variable ν is chosen to be zero, the lateral guidance method works in the same manner as the lateral guidance for docking and drives the target to the center of the camera FOV. Ensuring that the target remains within the camera FOV requires placing additional limitations on the value of ν. We develop a metric for optimizing ν that allows the seeker to more easily track the target in crosswinds.

We desire to find a value of ν that keeps the target in the field of view, but allows the seeker to more lateral heading flexibility to keep the seeker pointed into the prevailing wind as much as possible. Keeping the nose of the UAS pointed into the wind reduces crosswind effects and allows the seeker to maneuver with less bank angle effort, which may be important for some UAS payloads. The basic problem statement for the optimization of ν is

$$\min_\nu \min\left(\left((\chi_w-\psi_S(t+2T))^2\right)^{\frac{1}{2}},\left((\chi_w+\pi-\psi_S(t+2T))^2\right)^{\frac{1}{2}}\right), \tag{4.36}$$

subject to:

$$|\nu| \;\leq\; K_\phi k_\nu\bar{\eta}, \tag{4.37}$$

where T represents the time step, χ_w is the prevailing wind direction and, $0 \leq k_\nu \leq 1$, is a selectable gain. Using (4.33) for commanded bank angle as a function of the slack variable $\phi(\nu(t))$, the following relationships are computed

$$\begin{aligned}
\dot{\psi}_S(t) &= \frac{g}{V_S}\tan\phi(\nu(t)), \\
\psi_S(t+T) &\approx \psi_S(t) + T\dot{\psi}_S(t), \\
\psi_T(t+T) &\approx \psi_T(t) + T\dot{\psi}_T(t), \\
\rho(t+T) &\approx \rho(t) + T\dot{\rho}(t), \\
\eta(t+T) &\approx \eta(t) + T\dot{\eta}(t).
\end{aligned}$$

Inserting the above values into (4.33) to calculate $\phi(\nu(t+T))$, the Euler approximation for $\psi_S(t+2T)$ is calculated as

$$\psi_S(t+2T) \approx \psi_S(t+T) + T\left[\frac{g}{V_S}\tan\phi(\nu(t+T))\right]. \tag{4.38}$$

For the experiments performed in this dissertation, the optimization is performed by selecting eight candidate values of ν beginning with the maximum and minimum values and then dividing each by 2, 5 and 10. Each of these values of ν are used in the above equations to calculate ψ_S two time steps into the future using an Euler approximation. The value of ν that minimizes the difference in aircraft heading with respect to the prevailing wind (head wind or tail wind) is chosen and used in the guidance loop for that time step. This allows the target to move within the camera FOV, but not leave it. As will be shown later, this method produced good crosswind tracking performance.

Airspeed Control

Beginning with the subterm $\dot{\mathbf{W}}_3$ from (4.24) and substituting (4.13) for $\dot{\rho}$ we see that

$$\begin{aligned}
\dot{\mathbf{W}}_3 &= \rho\dot{\rho} \\
&= \rho\left[(V_T\cos(\psi_S - \psi_T + \eta) - V_S\cos\eta)\cos\gamma\cos(\beta+\theta) + V_S\sin(\beta+\theta)\sin\gamma\right].
\end{aligned} \tag{4.39}$$

Airspeed control supports two objectives, aerial tracking and aerial docking. Using seeker commanded airspeed V_S^c, the airspeed control is tailored for each purpose.

Airspeed Control for Docking

In the docking scenario, the distance between the seeker and the drogue will decrease until the two vehicles make contact. For the system to remain stable throughout this maneuver, airspeed V_S^c is selected such that the nonlinear terms in (4.39) are zero according to

$$V_S^c = \frac{-V_T \cos(\psi_S - \psi T + \eta)\cos\gamma\cos(\beta+\theta) - V_C}{\sin(\beta+\theta)\sin\gamma - \cos\eta\cos\gamma\cos(\beta+\theta)} \tag{4.40}$$

where V_C is the closure velocity and subject to the restriction that, $\sin(\beta+\theta)\sin\gamma - \cos\eta\cos\gamma\cos(\beta+\theta) \neq 0$. Substituting back into (4.39), the scalar subterm becomes

$$\dot{\mathbf{W}}_3 \;=\; -V_C\rho. \tag{4.41}$$

If V_C is chosen to be positive and the separation distance ρ remains positive, $\dot{\mathbf{W}}_\mathbf{3}$ is always negative which ensures that while using (4.40) for V_S^c, the target location in the camera FOV will remain in the FOV as the seeker approaches the drogue. As the LOS angles become very small, (4.40) reduces to the intuitive relationship

$$V_S^c = V_T + V_C. \tag{4.42}$$

Airspeed Control for Tracking

In the tracking scenario, the seeker maintains a desired separation distance ρ^d from the target. The error between the actual separation distance $\rho^d - \rho$ is substituted for ρ in (4.23) such

that

$$\begin{aligned}
\mathbf{W}_3 &= \frac{1}{2}(\rho^d - \rho)^2 \\
\dot{\mathbf{W}}_3 &= -\dot{\rho}(\rho^d - \rho) \\
&= -(\rho^d - \rho)\left[(V_T \cos(\psi_S - \psi_T + \eta) - V_S \cos\eta)\cos\gamma\cos(\beta+\theta) + V_S \sin(\beta+\theta)\sin\gamma\right].
\end{aligned} \tag{4.43}$$

The airspeed V_S^c is selected such that the nonlinear terms in (4.43) are zero according to

$$V_S^c = \frac{-V_T \cos(\psi_S - \psi T + \eta)\cos\gamma\cos(\beta+\theta) + K_V(\rho^d - \rho)}{\sin(\beta+\theta)\sin\gamma - \cos\eta\cos\gamma\cos(\beta+\theta)} \tag{4.44}$$

with the restriction that, $\sin(\beta+\theta)\sin\gamma - \cos\eta\cos\gamma\cos(\beta+\theta) \neq 0$. Substituting (4.44) back into (4.43), the scalar subterm becomes

$$\dot{\mathbf{W}}_\mathbf{3} \quad = \quad -K_V(\rho^d - \rho)^2. \tag{4.45}$$

If K_V is chosen to be positive, $\dot{\mathbf{W}}_\mathbf{3}$ is always negative which ensures that while using (4.44) for V_C^c, the target location in the camera FOV will remain in the FOV as the seeker tracks the target from a desired separation distance. As the LOS angles become very small, (4.44) reduces to proportional control according to

$$V_S^c = V_T - K_V(\rho^d - \rho). \tag{4.46}$$

Example

To demonstrate the system response to the control inputs using the guidance equations for tracking (4.26), (4.33), and (4.44) a six-degree-of-freedom simulation that included the seeker and target is shown in Figure 4.7. The seeker began 40 m behind, 20 m offset laterally, and 20 m below the target. The target was flying level and on a straight course with no wind. The seeker was commanded to follow directly behind the target with a separation distance of 30 m. The system

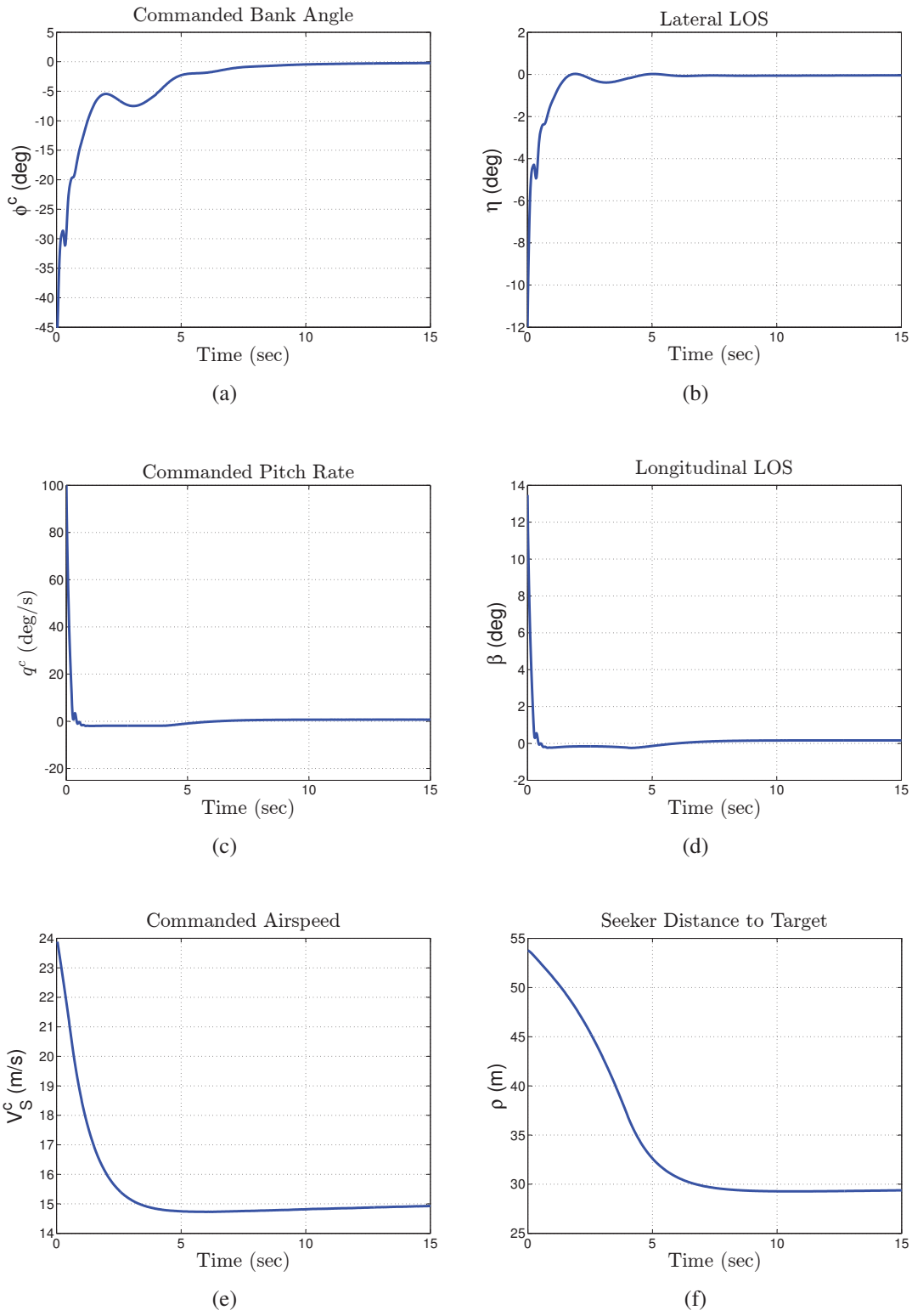

Figure 4.7: Comparison of visual pursuit guidance commands and dynamic response for aerial tracking; (a) commanded bank angle ($\nu = 0$); (b) lateral LOS angle; (c) commanded pitch rate; (d) longitudinal LOS angle; (e) commanded airspeed; (f) distance to target.

response is shown in Figure 4.7. It can be seen that the guidance inputs produce the appropriate dynamic responses for β, η, and ρ.

To show that the hidden dynamics with respect to ψ_S, ψ_T, and θ remain bounded for a typical maneuver, the target was flown at a constant altitude over a course with left and right turns of varying radii. The seeker began with a heading difference of 120 deg and an altitude separation of 30 m. The seeker was commanded to follow the target with a separation distance of 30 m. The system response is shown in Figure 4.8. It can be seen that ψ_S appropriately follows ψ_T and the large initial errors in θ and the quantity $\psi_S - \psi_T$ are rapidly corrected and then remain bounded throughout the maneuver. This example, while reassuring, does not constitute a proof that these variables will remain bounded under all circumstances. A full proof remains to be accomplished.

4.3.3 Limitations

There are two limitations to this method that occur when the seeker comes close to the target. The first occurs when the target reaches the camera FOV limit in either the lateral or longitudinal direction. Once the target has been acquired in the seeker FOV it will remain within the FOV as long as the distance between the two vehicles remains the same. However, if the seeker vehicle is closing the distance ρ between the vehicles it is possible for the target image to reach the boundary of the FOV and in some cases leave the FOV. The other limitation occurs when the distance between the two vehicles becomes so close that roll and pitch rate commands saturate the UAS pitch and roll control surfaces.

Closure Rate Limits

The longitudinal FOV limit may be reached when the seeker is climbing or descending and the target has reached the upper or lower FOV limit $\pm\bar{\beta}$ and the seeker has reached the maximum or minimum pitch angle θ_{max} and the maximum or minimum pitch rate $\dot{\theta}_{max}$. From (4.15), the longitudinal LOS rate can be written as

$$\dot{\beta} = -\dot{\theta}_{max} + \frac{1}{\rho}\left[(V_T\cos(\psi_S - \psi_T + \eta) - V_S\cos\eta)\cos\gamma\sin(\bar{\beta} + \gamma_{max}) - V_S\cos(\bar{\beta} + \theta_{max})\sin\gamma\right]. \tag{4.47}$$

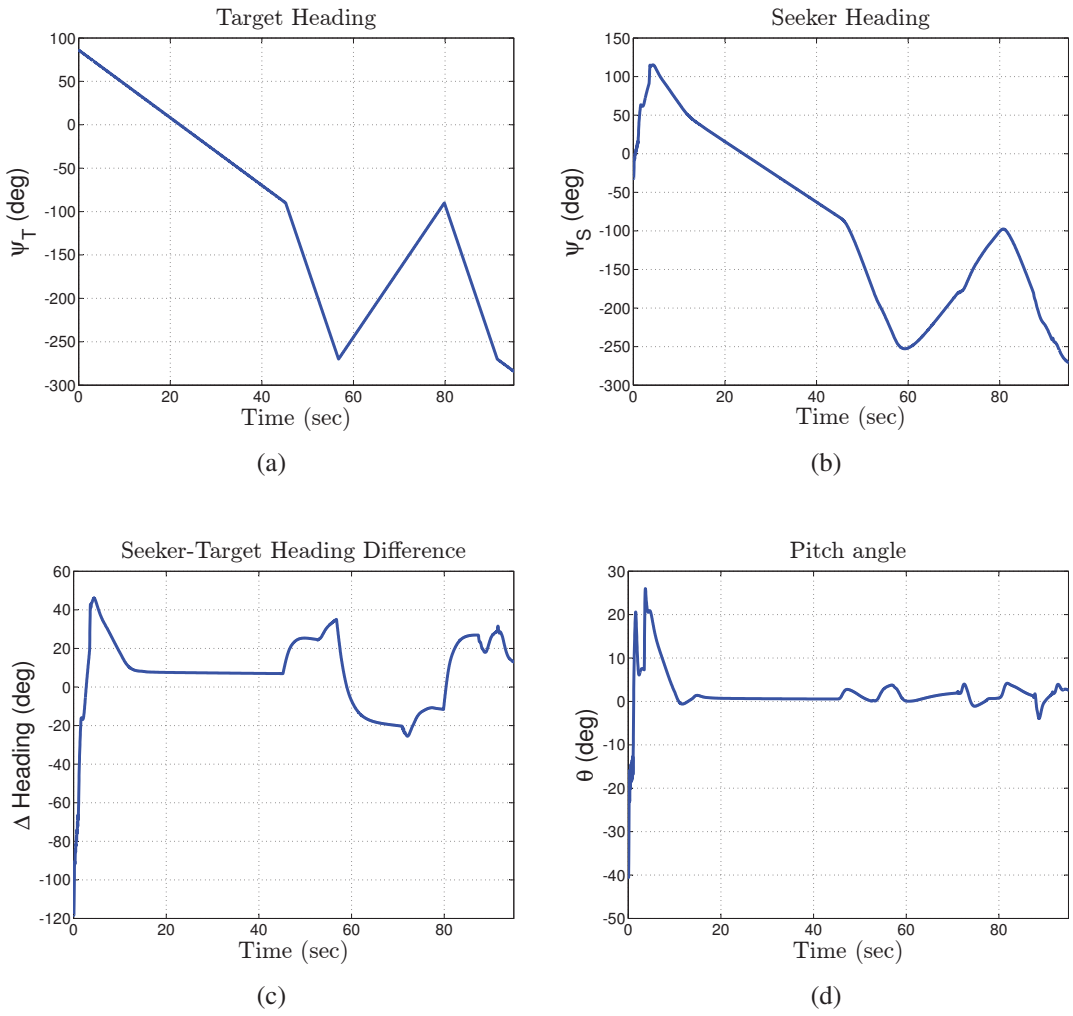

Figure 4.8: Hidden dynamic response; (a) target heading; (b) seeker heading; (c) heading difference between seeker and target; (d) pitch angle response.

For the target to remain within the FOV, $\dot{\beta}$ must remain negative according to

$$0 < -\dot{\theta}_{max} + \frac{1}{\rho}\left[(V_T\cos(\psi_S - \psi_T + \eta) - V_S\cos\eta)\cos\gamma\sin(\bar{\beta} + \gamma_{max}) - V_S\cos(\bar{\beta} + \theta_{max})\sin\gamma\right]. \tag{4.48}$$

To evaluate the closure rate limit, we rearrange to solve for V_s^c. When the pitch rate $\dot{\theta}$ has reached its maximum value, then the only way to keep the target in the FOV is to reduce the ascent

rate by restricting the commanded airspeed of the seeker V_s^c according to

$$V_S^c = \frac{V_T \cos(\psi_S - \psi_T + \eta)\cos\gamma \sin(\bar{\beta}+\theta) - \dot{\theta}_{max}\rho}{\cos(\bar{\beta}+\theta)\sin\gamma + \cos\eta\cos\gamma\sin(\bar{\beta}+\theta)}. \tag{4.49}$$

With the restriction that, $\cos(\bar{\beta}+\theta)\sin\gamma + \cos\eta\cos\gamma\sin(\bar{\beta}+\theta) \neq 0$. When $\dot{\theta}_{max}$ and $\bar{\beta}$ are negative we arrive at the same result as when positive values are chosen for $\dot{\theta}_{max}$ and $\bar{\beta}$.

In the lateral direction, from Figure 4.5 and (4.14), when the seeker is on the lateral FOV limit $\bar{\eta}$ the azimuth LOS rate $\dot{\eta}$ must remain negative to keep the target in the FOV according to

$$0 \quad < \quad -\dot{\psi}_{S_{max}} + \frac{1}{\rho}\left[-(V_T \sin(\psi_S - \psi_T + \bar{\eta}) - V_S \sin\bar{\eta})\cos\gamma\right]. \tag{4.50}$$

Rearranging and solving for V_S^c, it can be seen that when the heading change rate, or turn rate $\dot{\psi}_S$ has reached its maximum value, then the only way to keep the target in the FOV is to restrict the commanded airspeed of the seeker V_s^c according to

$$V_s^c \quad < \quad \frac{\rho\,\dot{\psi}_{S_{max}} + (V_T \sin(\psi_S - \psi_T + \bar{\eta})\cos\gamma}{\sin\bar{\eta}\cos\gamma}. \tag{4.51}$$

With the restriction that, $\sin\bar{\eta}\cos\gamma \neq 0$.

Separation Distance Limits

As the seeker closes on the target to very close distances, any movement of the target centroid in the image plane is magnified. By inspecting the longitudinal and lateral guidance algorithms (4.26) and (4.33) it can be seen that the line of sight distance ρ is in the denominator. When ρ becomes very small the control inputs ϕ^c and q^c become very large. As the seeker approaches the target, there comes a point when the movement of the target in the image plane results in commanded pitch rate or roll commands that exceed the ability of the aircraft to follow. This results in control saturation. A representative case for a small UAS is shown in Figure 4.9. For this case in the longitudinal direction, the pitch rate control using (4.26) may saturate at approximately 0.7 m from the target as shown in Figure 4.9(a). In the lateral direction, using $\nu < |0.27|$. It can be seen

in Figure 4.9(b) that inside of 2.8 m from the target, the vehicle roll control using (4.33) may be saturated.

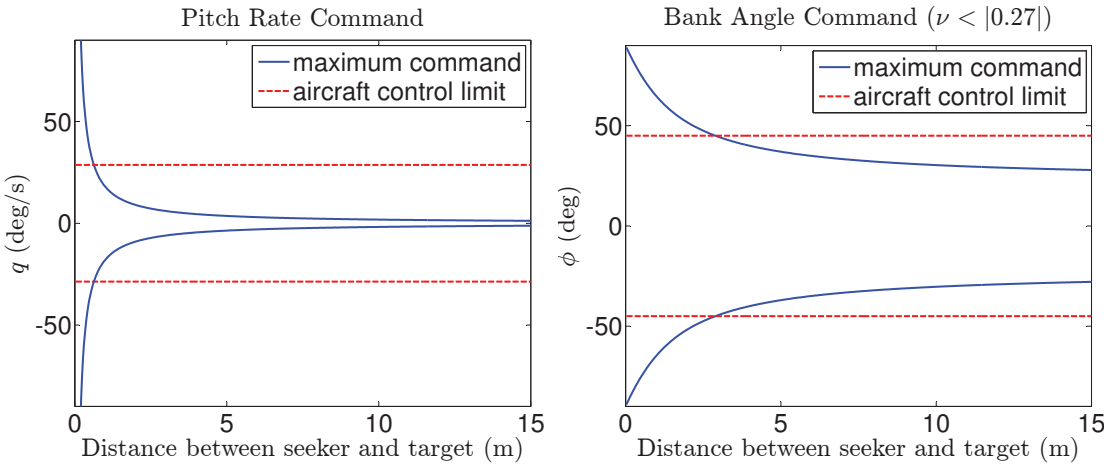

(a) (b)

Figure 4.9: Flight control saturation limits for a UAS with airspeed of 15 m/s. (a) Longitudinal saturation limit for $K_\theta = 0.8$ and $\bar{\beta} = 39$ deg; (b) lateral saturation limit for $K_\phi = 0.8$, $\nu < |0.27|$, and $\bar{\eta} = 39$ deg.

4.4 Guidance Laws from Decoupled Dynamics

The guidance laws for ϕ, $\dot{\theta}$, and V_S shown so far in this dissertation were developed using the three-dimensional dynamic relationships for aerial tracking and docking. The guidance laws can also be developed using two-dimensional dynamics where the lateral and longitudinal dynamics are decoupled. Guidance laws from two-dimensional dynamics can be used effectively when the aircraft does not operate in regions of high angle of attack where significant coupling between longitudinal and lateral control can occur. Guidance laws for visual pursuit were also developed using decoupled dynamics. The derivation of these models is provided in Appendix A. The two-dimensional models are simpler than the three-dimensional models, but show a very high degree of correlation in simulation. When the performance of the two models was compared over a highly dynamic course, the combined RMS difference in airspeed, bank angle, and for pitch angle was

less than 2 percent. Plots of the simulations can be seen in Appendix A. The guidance laws for ϕ and q, derived from decoupled dynamics, were used throughout the remainder of this dissertation.

An additional simplification was made with respect to seeker airspeed V_S. In (4.42) and (4.46) it was shown that for very small LOS angles, the airspeed command can be reduced to constant closure rate for docking and proportional control for maintaining a desired separation distance between the seeker and target. In Appendix A it was shown that by using the simplified airspeed relationships, the effect on performance when compared with the equations developed in this chapter is less than 10 percent. The simplified relationships for airspeed were used throughout the remainder of this dissertation.

Therefore the simplified versions of (4.31), (4.26), and (4.42) developed from decoupled lateral and longitudinal dynamics that are used for aerial docking are

$$\phi^c = \tan^{-1}\left[\frac{V_S}{g}\left(\frac{1}{\rho}(V_S\sin\eta - V_T\sin(\psi_S-\psi_T+\eta)) + K_\phi\eta\right)\right], \tag{4.52}$$

$$q^c = \frac{V_T\sin(\theta+\beta) - V_S\sin(\theta+\beta+\gamma)}{\rho} + K_\theta\beta, \tag{4.53}$$

$$V_S^c = V_T + V_C, \tag{4.54}$$

and the simplified versions of (4.33), (4.26), and (4.46) from decoupled dynamics for air-to-air tracking are

$$\phi^c = \tan^{-1}\left[\frac{V_S}{g}\left(\frac{1}{\rho}(V_S\sin\eta - V_T\sin(\psi_S-\psi_T+\eta)) + K_\phi\eta - \nu\right)\right], \tag{4.55}$$

$$q^c = \frac{V_T\sin(\theta+\beta) - V_S\sin(\theta+\beta+\gamma)}{\rho} + K_\theta\beta, \tag{4.56}$$

$$V_S^c = V_T - K_V(\rho^d - \rho). \tag{4.57}$$

4.5 Simulation Results

Simulations were conducted in Simulink using a six degree-of-freedom aerodynamic model of the seeker. The simulation airspeed of the target was between $15-20\,$m/s. The location of the camera was at the seeker center of gravity. Noise on the camera and on the GPS signal was included

in the simulation. A waggle maneuver that involved turns of various radii and direction as shown in Figure 4.10 was used to stress the lateral guidance algorithms.

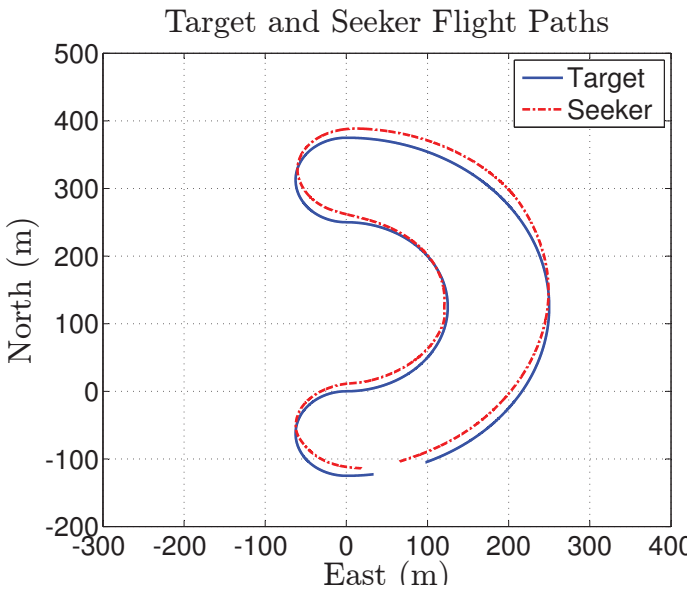

Figure 4.10: Waggle maneuver.

Three simulation cases are shown in Figure 4.11. The seeker was commanded to follow the target at a distance of 30 m. In addition to the difficult turns, the wind was simulated at 9 m/s from the south. The seeker began the maneuver with a 10 m altitude separation. The guidance inputs for the PI simulations were provided according to (4.20) and (4.21). For the simulation of visual pursuit, roll angle and pitch rate were controlled according to (4.55), (4.56) and (4.57), with $\nu = 0$ and $\nu < |.27|$.

The results depicted in Table 4.1 and Figure 4.11 show that the most effective method for maintaining a cooperative target in the center of the FOV is the visual pursuit method with $\nu = 0$. However the bank angle effort required to complete the maneuver is about 19 percent higher than using either PI or visual pursuit with $\nu < |0.27|$. The differences between the two cases of visual pursuit are significant. The mean LOS error when including ν in the guidance method is more than three times larger. This is by design as the addition of a non-zero value for the variable ν allows the target to move laterally within the FOV in order to optimize the seeker heading with respect to the wind and complete the maneuver with less bank angle effort. Overall LOS error and bank angle

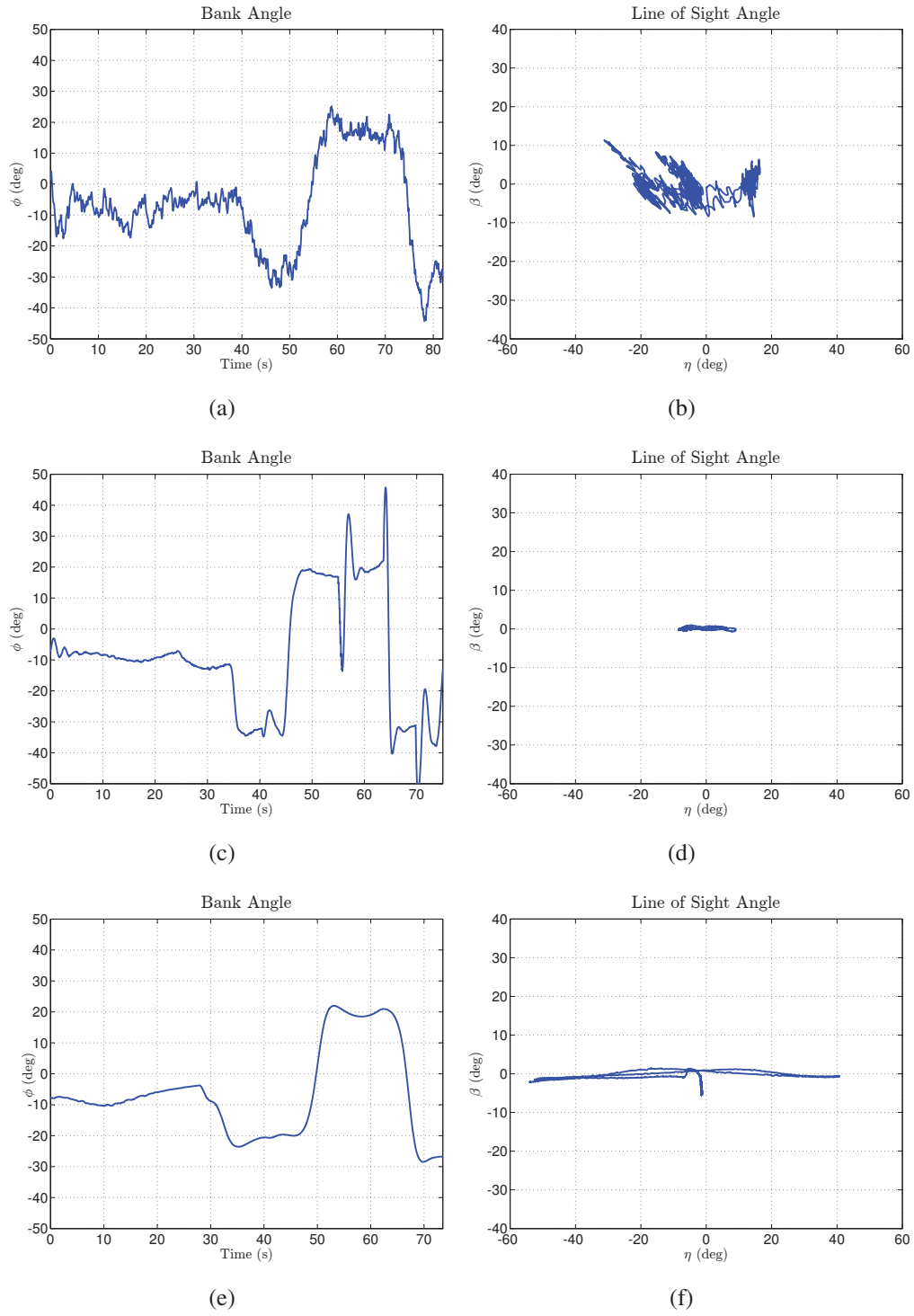

Figure 4.11: Simulation results from waggle maneuver with 9 m/s wind from the south; (a) PI bank angle; (b) PI LOS error to the target; (c) visual pursuit ($\nu = 0$) bank angle; (d) visual pursuit ($\nu = 0$) LOS error to the target; (e) visual pursuit ($\nu_{max} < |.27|$) bank angle; (f) visual pursuit ($\nu_{max} < |.27|$) LOS error to the target.

effort were calculated using the root mean square (RMS) of the data shown in Figure 4.11. An unexpected result from this scenario, was that the bank angle effort for the PI control was similar to the results for enhanced visual pursuit. Further investigation was conducted.

Table 4.1: Simulation LOS angles from waggle maneuver (RMS (deg))

Guidance Method	Line of Sight	Bank Angle
Proportional-Integral	11.6	14.2
Visual Pursuit, $\nu = 0$	5.8	18.0
Visual Pursuit, $\nu < \|0.27\|$	20.8	14.6

The significantly better LOS tracking performance of the baseline visual pursuit method with respect to the other methods had another effect; and that was to better maintain relative position with the target. In the examples shown, each used the same method for controlling airspeed given in (4.57). However, the baseline visual pursuit method was able to keep the target within 10 m of the desired separation distance, while both the PI control and enhanced visual pursuit methods allowed the seeker to lag as much as 70 m behind the target at some point during the waggle maneuver. The lag behind the target appeared to be a factor in the lower bank angle effort required to complete the maneuvers.

To more carefully differentiate the differences between PI control and visual pursuit in high winds a second simulation was conducted. The target was flown on a straight path with 20 m/s crosswind. The seeker was commanded to follow the target at a distance of 30 m. A comparison of the two methods after achieving a stable position behind the target is shown in Figure 4.12. It can be seen that the location of the target in the FOV of the seeker, when using visual pursuit with $\nu < |0.27|$, moved off center slightly, but the bank effort used was about 20 times less than the bank effort required by the UAS using PI control. The reduced bank-angle effort results from optimizing ν to keep the target heading as closely aligned with the prevailing wind direction as possible while allowing the target location in the image plane to move within a range that keeps the target within the FOV. The maximum absolute value of ν for stability is found using (4.37). However, to keep the target in the FOV, the maximum value of ν was experimentally found to be about 30 percent of the maximum allowable value.

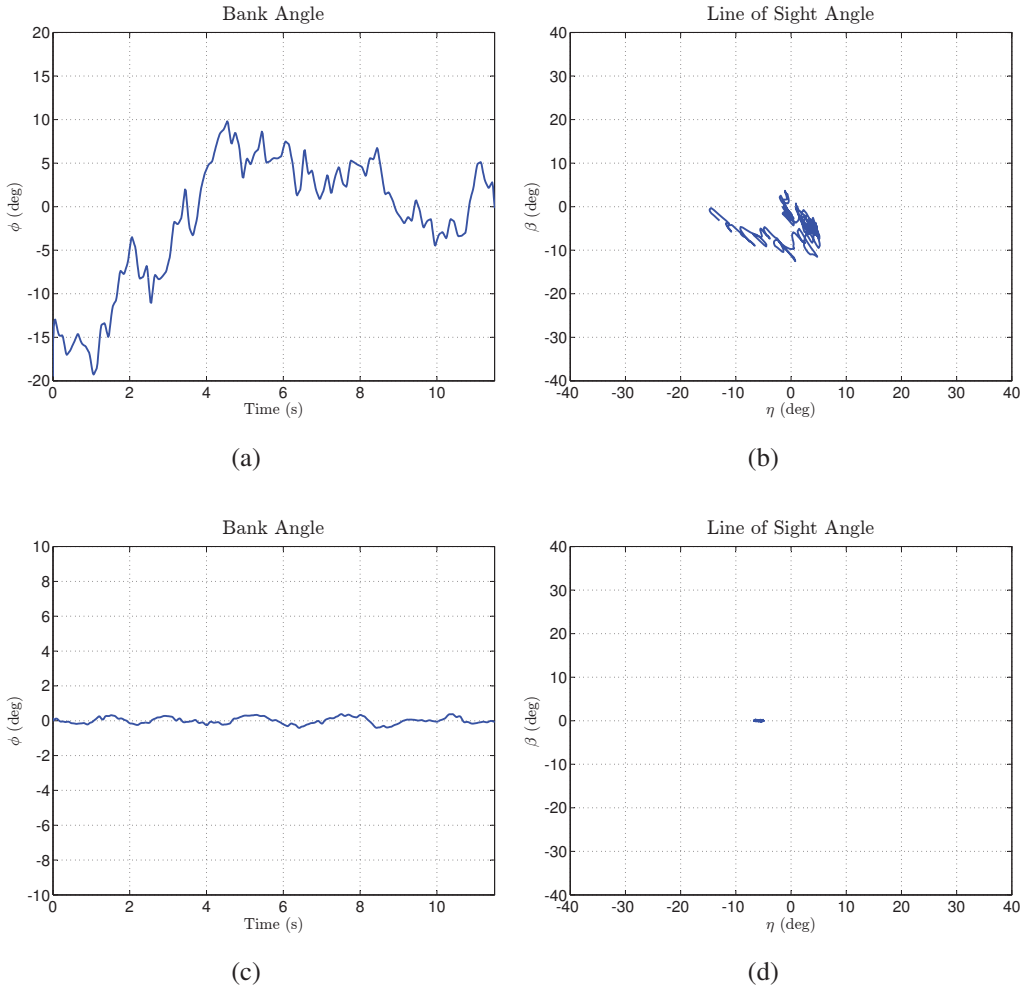

Figure 4.12: Simulation results from straight line flight with 20 m/s crosswind; (a) PI bank angle; (b) PI LOS error to the target; (c) visual pursuit bank angle; (d) visual pursuit LOS error to the target.

4.6 Experimental Results

In this section, flight trial results from experiments using PI guidance and visual pursuit are shown. A target UAS, a seeker UAS, and a ground station were the three elements that made up the hardware system used to test the guidance methods as described in Chapter 2.

4.6.1 Tracking Algorithm Performance

The visual pursuit algorithm was first flight tested and compared to the PI control method using only GPS position data from the target to test both algorithms over a long period of time

using the waggle maneuver to compare the algorithms when making turns in both directions. A comparison of the results can be seen in Figure 4.13. The methods were tested in with a 9 m/s wind from the south. Both vehicles flew nearly identical paths and were commanded to follow the target at a distance of 30 m and an altitude of 100 m. Both vehicles began at approximately the same altitude as the target so that the test primarily stressed the lateral tracking accuracy. Gains were tuned for both vehicles such that they were as aggressive as possible in the lateral direction without creating high frequency oscillations in the control effort.

The PI method controlled pitch and roll angle according to (4.20) and (4.21). The RMS of the LOS tracking error of 14.0 deg. Flight path angle rate and roll angle were controlled according to (4.26) and (4.33) with $\nu = 0$ for the visual pursuit method. This method had a RMS tracking error of 8.9 deg. This was an improvement of 37 percent over the PI method. Comparing the lateral guidance algorithms from (4.20) and (4.33) we see that the linear method is a function of the lateral LOS angle η only, while the nonlinear method includes additional information about the target including: LOS distance, heading, and airspeed along with η. The nonlinear method does not have the intuitive feel of the PI method, but the additional data used in the algorithm results in improved tracking performance. Both methods proved to be very robust. When using GPS data, either method could be initiated from any aspect angle to the target and the seeker would execute an appropriate maneuver to position itself behind the target at the commanded separation distance.

4.6.2 Vision Sensor Performance

The performance of both methods was tested using vision data. The visual image transmitted to the ground station from the camera was used by the ground station operator to manually designate the target. Vision data was used to drive the guidance algorithms running on the VPU to provide ϕ^c and q^c as seen in (4.26) and (4.33). Commands for the PI control method came from (4.20) and (4.21). Figure 4.14 shows the image as seen from the ground station prior to and after locking onto the target. When the seeker is locked on, a box is drawn around the region on the image that the seeker is tracking.

Figure 4.15 shows the seeker tracking and following the target from an average of 30 m over a approximately one orbit for both PI control and visual pursuit. The target is following a 250 m

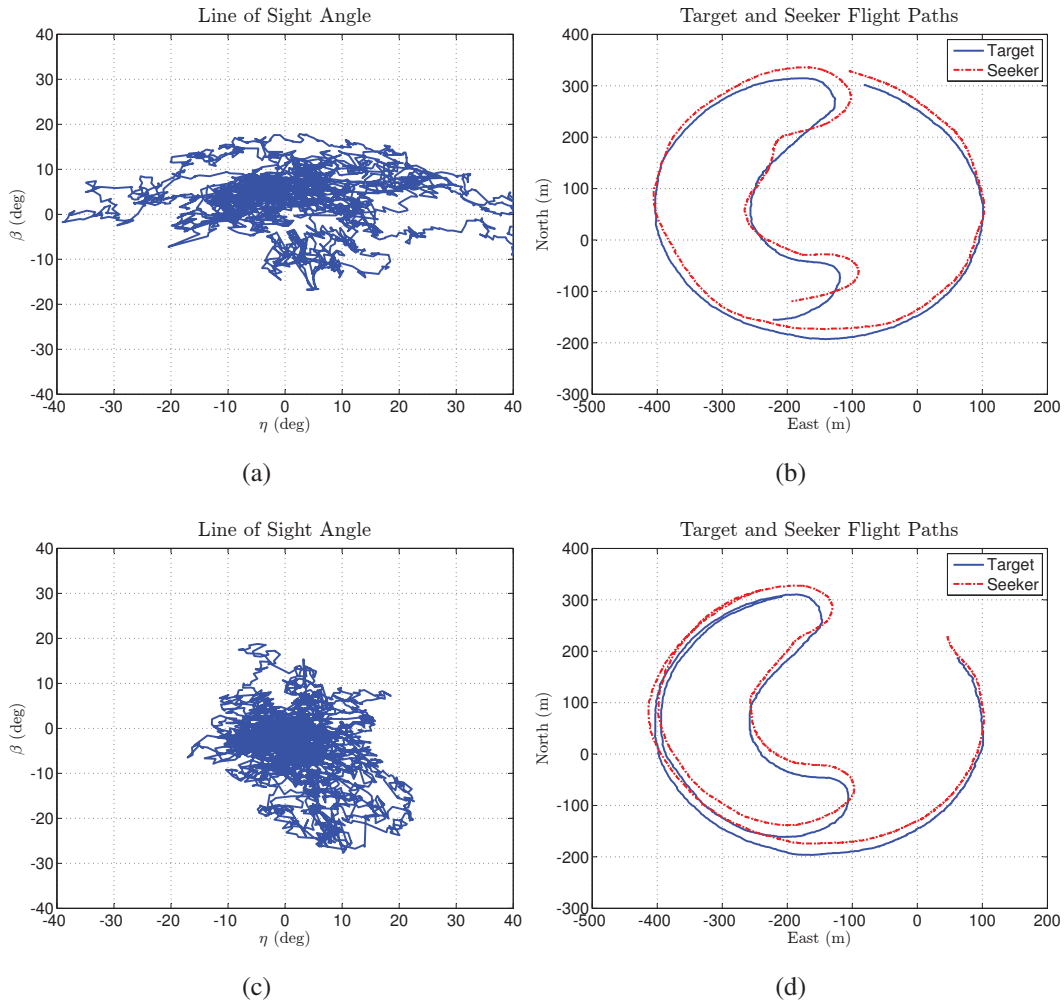

Figure 4.13: Flight results. (a) LOS error to the target vehicle based on GPS position for seeker vehicle using PI control guidance; (b) Seeker and target flight paths for PI control following. (c) LOS error to the target vehicle based on GPS position for seeker vehicle using visual pursuit $\nu = 0$; (d) Seeker and target flight paths for visual pursuit method. Average wind for both cases was 9 m/s from the south.

radius orbit and the seeker is using vision and GPS sensor data to follow it. With a 79 deg field of view lens, the LOS angles that allowed the target to remain on the image plane were ± 38 deg. When the seeker lost track on the target, it was due to the inability of the vision tracker to maintain a visual lock in the presence of movement of the target within the image. There were no observed instances where the seeker failed to keep the target in the FOV when a good visual track was active. When the seeker lost visual track of the target, the guidance software immediately switched to using GPS data for inputs.

Figure 4.14: Seeker video frame with track enabled. Camera had IR filter installed for this image. The square box indicates the tracked region.

For PI control, winds were 7 m/s from the northwest. The seeker lost the track twice during the experiment and was locked onto the target approximately 77 percent of the time. In Figure 4.15a, the LOS errors when using GPS are plotted along with the LOS errors when using vision. The vision data had a mean error from the centerline of 20.8 deg and the GPS data had a mean error of 38.3 deg. When using vision data, the PI control method had a mean error 84 percent better than when using GPS which can be attributed to the time delay and position uncertainty when using GPS. When using vision data, there is no appreciable time delay.

For visual pursuit, winds were light, approximately 2 m/s from the south and ν was set to zero. The seeker lost lock-on twice during this test and was locked on for approximately 66 percent of the time. In Figure 4.15c, the LOS errors when using GPS are plotted along with the LOS errors when using vision. The vision data had a mean error from the centerline of 11.8 deg and the GPS data had a mean error of 15.6 deg. The visual pursuit method when using vision had a mean error 32 percent better than when using GPS. The longitudinal LOS error β was significantly higher than observed in the simulation results. This is most likely a result of not tuning the K_θ sufficiently. Looking at a summary of the flight trial results in Table 4.2 it is evident that lateral LOS error η comparison between PI and visual pursuit are consistent with the results from simulation as shown in Table 4.1 and the flight trial performance using GPS inputs to the guidance algorithm as described previously.

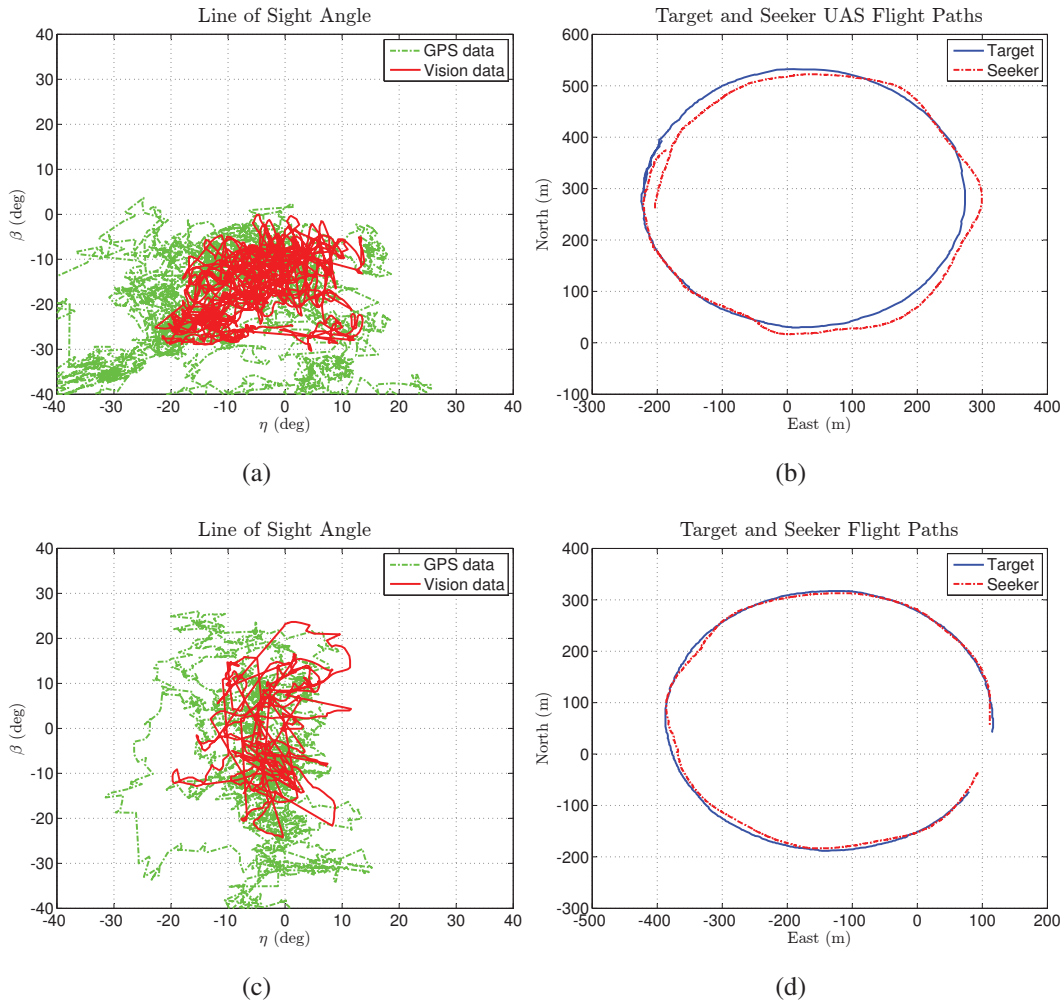

Figure 4.15: Flight results. (a) LOS error to the target vehicle based on GPS position (green) and vision data (red) for seeker vehicle using PI control guidance; (b) seeker and target flight paths; (c) LOS error to the target vehicle based on GPS position (green) and vision data (red) for seeker vehicle using visual guidance, $\nu = 0$; (d) seeker and target flight paths, $\nu = 0$.

4.7 Chapter Summary

In this chapter we have developed and experimentally flown two guidance methods for autonomous air-to-air tracking. The first method is a proportional-integral (PI) method that is based on minimizing the lateral and longitudinal LOS angles between the seeker and the target. The control inputs are commanded airspeed, bank angle and pitch. The second method is a nonlinear method called *visual pursuit* that in addition to using LOS angles also uses knowledge of the target velocity and heading (provided by a cooperative target) to produce control inputs for minimizing LOS angles. The control inputs to the autopilot are airspeed, bank angle and pitch rate. Visual

Table 4.2: Flight trial LOS angles for waggle maneuver (RMS (deg))

Guidance Method	Vision LOS	Vision η	Vision β	GPS LOS	GPS η	GPS β
Proportional-Integral	20.8	8.4	18.6	38.3	20.8	29.9
Visual Pursuit, $\nu = 0$	11.8	4.8	10.1	15.6	6.9	12.6

pursuit also has the capability to allow lateral movement of the target within the image frame to allow for improved tracking in high crosswind environments. A proof of stability in the Lyapunov sense is shown provided that the FOV is defined as a circular region and the control inputs for V_S^c, ϕ^c, and q^c do not saturate. PI guidance is compared with visual pursuit in both simulation and flight trials to demonstrate the suitability of both methods and to show the increased performance that is possible using visual pursuit in highly dynamic flight environments.

CHAPTER 5. AERIAL DOCKING USING A PASSIVE TOWED CABLE SYSTEM

5.1 Introduction

This section provides experimental results from docking trials and further develops methods developed in Chapter 4 to provide guidance for the seeker to autonomously rendezvous and dock with an airborne drogue. When the mothership flies a circular orbit while towing the drogue in steady-state flight, the drogue will adopt an interior orbit and in the presence of a constant wind this orbit will be roughly elliptical and rotated out of the horizontal plane [30] as shown in Figure 5.1. Chasing the drogue up and down an elliptical path that can change as much as 50 m in

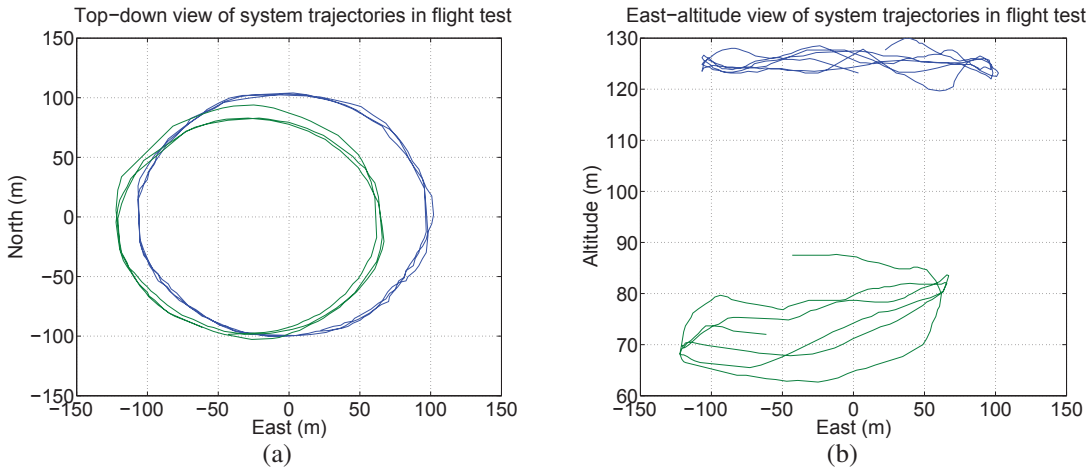

Figure 5.1: System trajectories in the presence of 4 m/s wind from the east. (a) Mothership and drogue orbits. Mothership (outer) orbit has a radius of 100 m at airspeed of 14 m/s while the resulting drogue (inner) orbit has a radius of approximately 90 m; (b) Side view, drogue (lower) orbit is inclined due to the presence of wind. The altitude oscillation is approximately 20 m.

altitude over a 150 m diameter orbit with $5-10$ m/s winds significantly increases the complexity of the rendezvous. It has been shown that by modifying the trajectory of the mothership, the drogue orbit can be flattened to altitude deviations of less than 10 m over the period of a single orbit [30].

Prior research developed a numerical method for approximating the elliptical drogue orbit using the drogue GPS position measurements [5].

In a windless environment, given a drogue with a large aerodynamic drag coefficient, a horizontal mothership orbit drives the drogue to converge to a horizontally level orbit with a smaller radius than that of the mothership orbit. However, when wind is present, the resulting drogue orbit will be inclined in the vertical direction and has an offset in the horizontal direction, as shown in Figure 5.1. For this case, the amplitude of the drogue's altitude oscillation was approximately 20 m. A flatter trajectory of the drogue is preferred for the seeker in the final phase of the aerial rendezvous. Therefore, a strategy for keeping the drogue orbit horizontally level in the presence of wind is needed to facilitate a successful aerial rendezvous. The cable is modeled as a series of rigid links connected by end-to-end frictionless spherical joints. Detailed description for equations of motion of cable dynamics can be found in [32]. Given a desired drogue trajectory, the desired trajectory for the mothership can be derived and converted into a series of waypoints for the mothership to follow [50].

The body of this chapter has three main sections. In Section 5.2, we describe the equations used for providing guidance to the seeker for docking with a drogue. Section 5.3 contains experimental results for docking trials from a full system demonstration. Section 5.4 provides a modification to visual pursuit that improves docking performance. The final section is a chapter summary.

5.2 Seeker Guidance

The seeker is assumed to be equipped with a monocular camera mounted on the centerline of the vehicle and the camera is able to provide the guidance algorithm with the lateral and longitudinal pixel location of the drogue in the image. A Lyapunov-based visual pursuit method that is compatible with both GPS and vision sensor data was developed in Chapter 4. Simplified guidance laws were developed by assuming decoupled lateral and longitudinal dynamics as shown in Appendix A. The guidance equations used in the docking trials are found in (4.52), (4.53) and (4.54).

As the seeker approaches the drogue, the LOS distance ρ is reduced in size until at very small distances, the guidance equations for ϕ and q saturate. It was assumed that with aircraft

limits on roll and pitch, and by scaling the gains K_θ and K_ϕ so that they were zero at contact, control saturation would occur at very close distances to the target and therefore would not be a significant factor in docking performance. This assumption was incorrect and resulted in control saturation at distances up to several meters from the drogue that significantly degraded docking performance in the flight trials. The observation of this problem led to the development of the contact factor explained later in this chapter that compensated for this limitation at close range to the target.

5.3 Experimental Results

The hardware system used to test the control algorithms developed during this project consisted of four elements: a seeker, a mothership UAS to tow the drogue, a passive towed drogue, and a ground station with associated communication structure. These elements are described in Chapter 2. The autopilot on the mothership received waypoint commands based on the desired drogue orbit and the current state of the mothership. The resulting trajectory, which roughly corresponds to one orbit, was then discretized into waypoints and sent to the autopilot.

The flight trials were conducted in a build-up approach, beginning with tracking the mothership as the target before attempting to follow and rendezvous with the drogue. Both GPS and vision data were used as sensor inputs for the tracking algorithm. The seeker followed the mothership at a nominal distance of 30 m and an altitude of 125 m. Both vehicles began at approximately the same altitude. Therefore, the test primarily stressed the lateral tracking accuracy. The test was conducted such that when the seeker lost visual lock on the mothership, the guidance algorithm reverted to using GPS position, velocity and heading data relayed from the mothership. If the seeker sensed that it had passed the drogue using the half-plane definition from [13], it reduced its airspeed and retreated to a position 30 m behind the drogue prior to beginning the docking attempt again.

The tracker sometimes lost track of the airborne target because of the target motion or changes in background color, even when the target remained within the camera FOV. This required the operator to rapidly redesignate the target location. When the vision track was lost, sensor data for tracking guidance reverted to receiving the GPS location of the airborne target as it was rebroadcast from the ground station. GPS position data from the target was always running in the

background. When using rebroadcast GPS data, the data was delayed by approximately 200 ms. At a nominal airspeed of 15 m/s, this results in a position error of about 3 m. The operator received visual feedback when vision tracking was engaged. Whenever the square designation box was visible, as can be seen in Figure 5.2, the seeker was using vision data for guidance with no appreciable delay in the drogue position information.

Figure 5.2: Single frame from UAS camera while following drogue. Drogue is visible in center of green acquisition box. Mothership is obscured by top right corner of acquisition box.

GPS is accurate to within 4.6 m spherical error probable [47]. Even though the same guidance algorithm was used independent of whether the data was received from GPS or vision processing, a change in the data source always created a jump in the target position as perceived by the seeker. This was followed by a period of oscillation while the seeker worked to zero the new errors in η and β caused by the rebroadcast time delay and GPS error. The size of the jump in the LOS angles generally increased as the distance to the drogue decreased. For example, a position uncertainty of 4.6 m at a distance of 30 m causes a LOS angle jump of 9 deg. That same position uncertainty at a distance of 10 m causes a LOS angle jump of 28 deg. From experience it was learned that any loss of vision data inside of 10 m from the drogue was unrecoverable and the docking engagement had to be restarted.

The test of the vision rendezvous system brought all the pieces together. The mothership was flown towing a non-actuated hemispheric drogue on an flexible 85 m cable while executing

trajectory tracking to keep the drogue orbit level. The seeker was flown using the visual pursuit algorithm to track, follow, and attempt to touch the airborne drogue. The drogue was towed in a 250 m radius circular orbit with an approximate airspeed of 15 m. The seeker began the rendezvous attempt from a stable position 20 to 30 m behind the drogue. When the seeker had a good visual lock, the engage command was given from the ground station which commanded the seeker to close the distance to the drogue using (4.54). The seeker closure airspeed was generally 2 m/s faster than the drogue airspeed. An example engagement is shown in Figure 5.3. Winds were 2 m/s

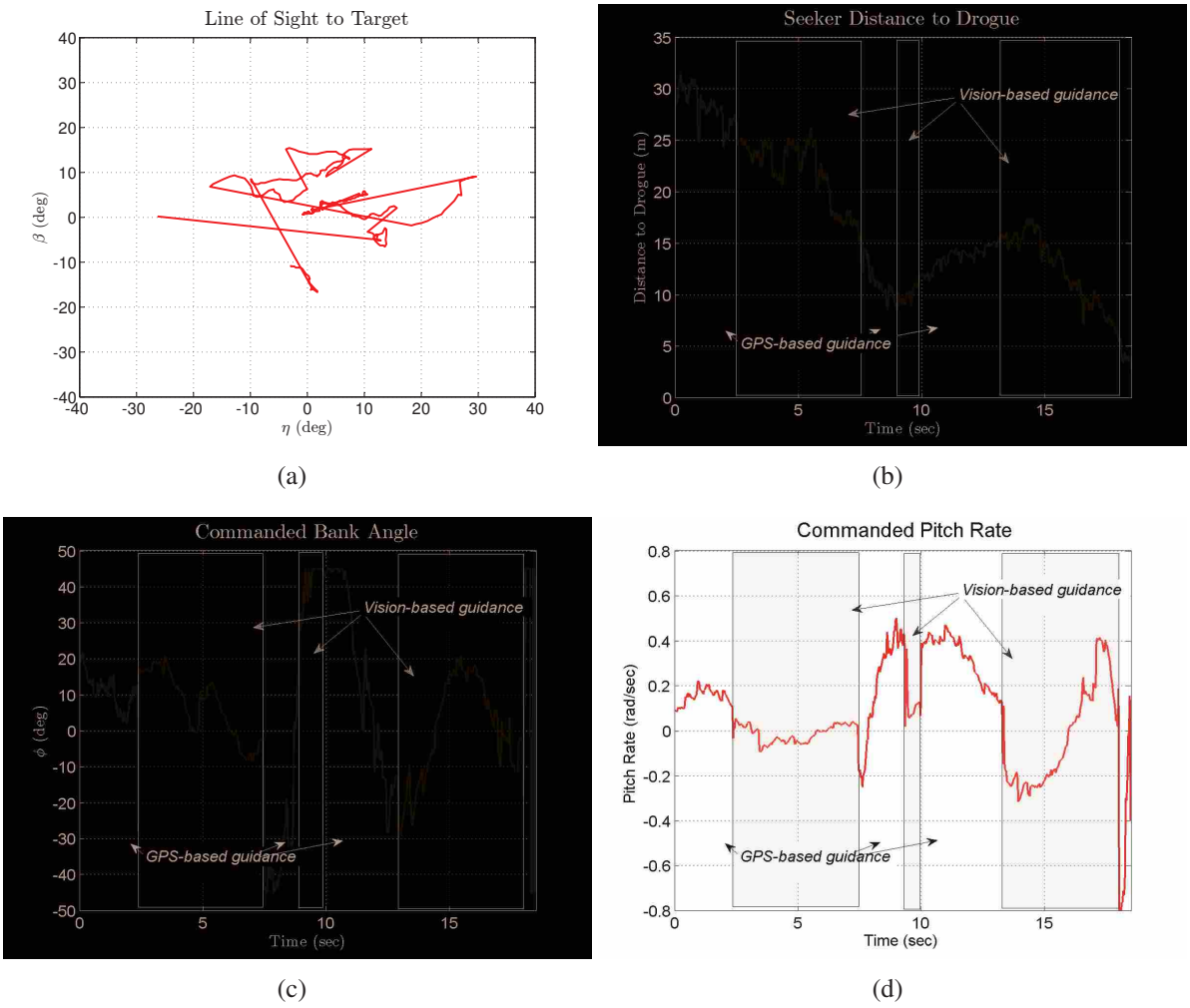

Figure 5.3: Flight test results of the seeker closing on the drogue (a) Vision-based LOS error to the drogue. Camera pixel data converted to LOS angles according to (4.1) and (4.2); (b) Seeker distance to drogue, time segments using vision guidance indicated by the shaded region, GPS data used at other times; (c) commanded roll angle; (d) commanded pitch rate.

from the west. The LOS angles to the drogue are shown in Figure 5.3 (a). The hardware limitations of the vision tracker mentioned previously are most evident as the seeker gets closer to the drogue. The sharp jumps in the LOS angles are a result of the guidance algorithm switching between vision data and GPS data as the seeker acquired and then lost visual track on the drogue. This phenomenon can more easily be seen in Figure 5.3 (b) where the regions of vision-based guidance and GPS-based guidance are overlayed on a plot of the separation distance between the seeker and the drogue. During this engagement the seeker passed by the drogue with its closest approach at 2.7 m. The control inputs shown in Figure 5.3 (c) and (d) also show a correlation with transitions between vision and GPS data. In addition, these plots show an inherent weakness of vision-based control as it nears the target. Examining (4.52) and (4.53) we see that commanded bank angle and pitch rate are functions of the LOS distance ρ in the denominator. At very close range to the target, the control inputs become large and eventually saturate during the final half-second of the engagement shown.

Approaches to within a few meters like the example shown were common. To improve end-game performance, a more robust visual tracker is needed and a modification to the guidance law must be made to prevent the control inputs from reaching saturation just before hitting the drogue.

5.4 Modified Visual Pursuit for Near-target Maneuvering

There are two ways that the guidance commands ϕ^c and q can become very large and saturate the flight controls. First the LOS of sight angles η and β can become large. At long distance from the target this general does not present a problem as the seeker has time to maneuver to reduce η and β. However just before contact with the drogue η and β are likely to spike. This is because any offset from the drogue centerline at fractions of a meter from the target will cause a large LOS angle. If the gains K_ϕ and K_θ are not reduced prior to contact with the drogue, there is usually a large pitch or roll command right at contact. Therefore to keep the seeker attitude level at contact, K_ϕ and K_θ are scaled to near zero over the last 0.2 m before contact. The gains remain positive satisfying the stability requirement in (4.24).

The other way to induce flight control saturation is to allow ρ to become very small. The flight test results from the previous section, as seen in Figure 5.3, showed that when the seeker

approached the target and the LOS distance ρ approached zero, the control inputs ϕ^c and q^c became large and caused the aircraft roll and pitch rate controls to saturate. To ensure that ρ does not approach zero the LOS vector $\boldsymbol{\rho}$ is extended in length beyond the target by a distance called the contact factor $\mathbf{C}$. This distance is added to the length of the LOS vector $\boldsymbol{\rho}$ as shown in the modified lateral dynamics in Figure 5.4. The LOS angles η and β are not modified in any way.

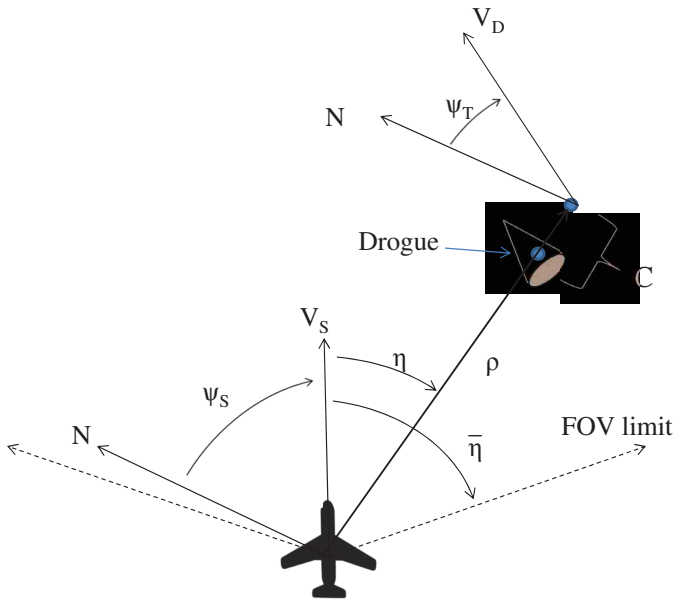

Figure 5.4: Two-dimensional lateral polar coordinates of the seeker and drogue in the $x-y$ body frame. Where $\boldsymbol{\rho}$ is the LOS vector between the seeker and the drogue; $\boldsymbol{C}$ is the contact factor extension to $\boldsymbol{\rho}$; η is the angle between the seeker heading and the line-of-sight vector; $\bar{\eta}$ is the maximum FOV angle; and the angles ψ_S, and ψ_T are the seeker and drogue headings.

The contact factor $\mathbf{C}$ is extended in both the lateral and longitudinal directions. We derive a new enhanced LOS vector $\boldsymbol{\rho}_\mathbf{C}$ that is an extension of $\boldsymbol{\rho}$ according to

$$\boldsymbol{\rho}_\mathbf{C} \;=\; \boldsymbol{\rho} + \mathbf{C}. \tag{5.1}$$

Two methods are considered for accomplishing this objective.

5.4.1 Minimum-distance Contact Factor

To prevent ρ from becoming too small, ρ is limited to a minimum value. As the distance between the seeker and the drogue becomes smaller it will eventually reach the critical distance ρ_{lim} where ρ will be held constant until contact with the drogue. Therefore, there are no changes to the guidance laws until the critical distance is reached after which, ρ is fixed for the remainder of the docking engagement. The minimum distance ρ_{lim} which is equal to the maximum length of the $\mathbf{C}$ is chosen so that it is at least long enough to keep the lateral and longitudinal control inputs out of the saturation region. This method has the effect of increasing the length of the contact factor $\mathbf{C}$, distance for distance, as the seeker approaches the drogue. The length of the contact factor is calculated according to

$$\mathbf{C} = \begin{cases} \rho_{lim} - \rho & \text{if } \rho > \rho_{lim} \\ 0 & \text{otherwise,} \end{cases} \tag{5.2}$$

therefore, from (5.1), the length of ρ_C is calculated according to

$$\begin{aligned} \rho_C &= \rho + \rho_{lim} - \rho, \\ &= \rho_{lim}. \end{aligned} \tag{5.3}$$

The LOS angles continue to run through the target and therefore the stability of the guidance equations with respect to $\boldsymbol{\rho}_{\mathbf{C}}$ is unchanged. The minimum-distance contact factor reaches its maximum C_{max} value when the seeker contacts the drogue. References to the value of the distance-limited contact factor will refer to C_{max}.

The equation used to command q^c becomes

$$q^c = \begin{cases} \frac{V_T \sin(\theta+\beta) - V_S \sin(\theta+\beta+\gamma)}{\rho} + K_\theta \beta & \text{if } \rho > \rho_{lim} \\ \frac{V_T \sin(\theta+\beta) - V_S \sin(\theta+\beta+\gamma)}{\rho_{lim}} + K_\theta \beta & \text{otherwise,} \end{cases} \tag{5.4}$$

and ϕ^c is

$$\phi^c = \begin{cases} \tan^{-1}\left[\frac{V_S}{g}\left(\frac{V_S}{\rho}\sin\eta - \frac{V_D}{\rho}\sin(\psi_S - \psi_T + \eta) + K_\phi \eta\right)\right] & \text{if } \rho > \rho_{lim} \\ \tan^{-1}\left[\frac{V_S}{g}\left(\frac{V_S}{\rho_{lim}}\sin\eta - \frac{V_D}{\rho_{lim}}\sin(\psi_S - \psi_T + \eta) + K_\phi \eta\right)\right] & \text{otherwise.} \end{cases} \tag{5.5}$$

The equation for airspeed control (4.54) remains unchanged.

The difference between the new method using $\mathbf{C}$ and the baseline method comes down to reducing the control input in relation to the difference between the actual LOS distance ρ and ρ_{lim}. When the ratio of ρ to ρ_{lim} is near unity, the guidance methods are the same. As ρ decreases, the ratio of ρ to ρ_{lim} becomes very small and the control inputs also become very small. The difference between this method and what was implemented in the experimental flight tests described in Section 5.3 is that ρ never becomes zero and therefore if ρ_{lim} is chosen correctly, the autopilot controls do not saturate.

5.4.2 Fixed-length Contact Factor

Another way to use the contact factor is determine a fixed length for $\mathbf{C}$ and use it throughout the docking maneuver. The contact factor should be chosen so that it is at least long enough to keep the lateral and longitudinal control inputs out of the saturation region. The length of the LOS vector with a fixed-length contact factor is expressed according to

$$\begin{aligned} \rho_C &= \rho + \mathbf{C} \\ &= \rho_{fixed}, \end{aligned} \tag{5.6}$$

where C is a fixed length. The LOS angles η and β continue to run through the actual target and therefore the control inputs are guiding the seeker to a point behind the target, but running through the target. The change to using ρ_{fixed} does not change any of the assumptions in the stability proofs presented earlier in this dissertation. The new longitudinal guidance equation from (4.53) becomes

$$q^c = \frac{V_T \sin(\theta + \beta) - V_S \sin(\theta + \beta + \gamma)}{\rho_{fixed}} + K_\theta \beta. \tag{5.7}$$

The lateral guidance equation from (4.52) becomes

$$\phi^c = \tan^{-1}\left[\frac{V_S}{g}\left(\frac{V_S}{\rho_{fixed}}\sin\eta - \frac{V_D}{\rho_{fixed}}\sin(\psi_S - \psi_T + \eta) + K_\phi \eta\right)\right]. \tag{5.8}$$

The equation for airspeed control (4.54) is unchanged.

5.4.3 Comparison of Methods

A comparison of the two methods was carried out using the same six-degree-of-freedom aerodynamic model and simulation technique used in Chapter 4. Fixed-length and minimum-distance contact factors between zero and 200 were selected and used in a scenario where the seeker began 130 m behind the drogue and with a heading difference of 90 deg between the drogue and seeker. The seeker was commanded to rendezvous and dock with the drogue using the guidance methods specified in (5.4), (5.5), (5.7) and (5.8). The drogue was moving on a constant heading and the seeker had a closing velocity of 3 m/s. Figure 5.5 shows the results from the simulations. Figure 5.5(a) shows the miss distance, which is the distance between the seeker and drogue centerlines at contact. Figure 5.5(b) shows the aircraft attitude in pitch and roll at contact.

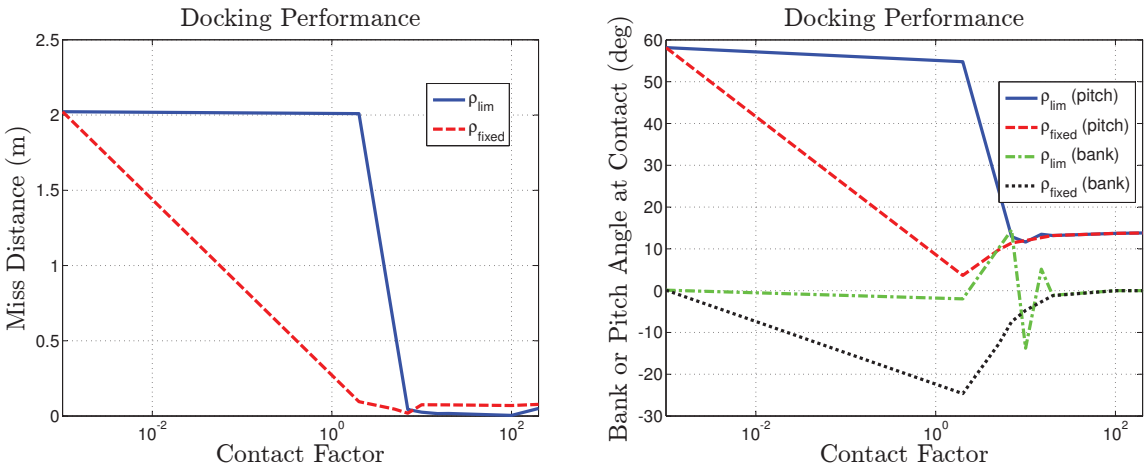

(a) (b)

Figure 5.5: Fixed-length and minimum-distance contact factor comparison; (a) miss distance comparison; (b) pitch and bank angles at contact.

It can be seen that without any modification to length of ρ, the miss distance is about 2 m which is consistent with the flight test results shown previously. As the fixed-length and minimum-distance contact factor distances are increased, the miss distance decreases and stabilizes at a contact factor value of 20 for both methods. It is interesting to note that even for very large contact factors, for example $C = 200$, docking performance is very good. While both methods produce miss distances less than 0.1 m, the minimum-distance contact factor rather than the fixed-length contact factor produced the smallest miss distances. The other factor that is important in docking is the seeker attitude at contact. It is desired that the seeker contact the drogue in a wings-level attitude and with a shallow pitch angle. As can be observed in Figure 5.5(b), when the contact factor reaches 20, the seeker aircraft contacts the drogue with wings level ($\phi = 0$), and at the desired steady-state approach pitch angle (for this scenario about 14 deg). In addition, there is no control saturation as the seeker approaches the drogue as was seen during the flight trials. The reason for the improved miss distance performance using the minimum-distance contact factor when compared with fixed-length contact factor can be seen in Table 5.1.

Table 5.1: Comparison of minimum-distance and fixed-length contact factor miss distances (m). $C = 20$.

Actual distance to target	30	25	20	15	10	5	0
ρ_{lim} distance to target	30	25	20	20	20	20	20
ρ_{lim} distance error	0	0	0	5	10	15	20
ρ_{fixed} distance to target	50	45	40	35	30	25	20
ρ_{fixed} distance error	20	20	20	20	20	20	20

Considering only the final 20 m of the rendezvous before contact, the cumulative distance error for the ρ_{lim} method is half the value of the distance error using ρ_{fixed} as can be seen in Figure 5.6. Modifying the length of the ρ vector in the guidance equations has the effect of damping the control inputs. The minimum-distance method delays the start of control input damping when compared with the fixed-length contact factor method. Damping then increases proportional to the distance to the drogue over the final few meters. This results in smaller miss distances when compared to having a fixed error for the entire approach and rendezvous. Therefore, the minimum-

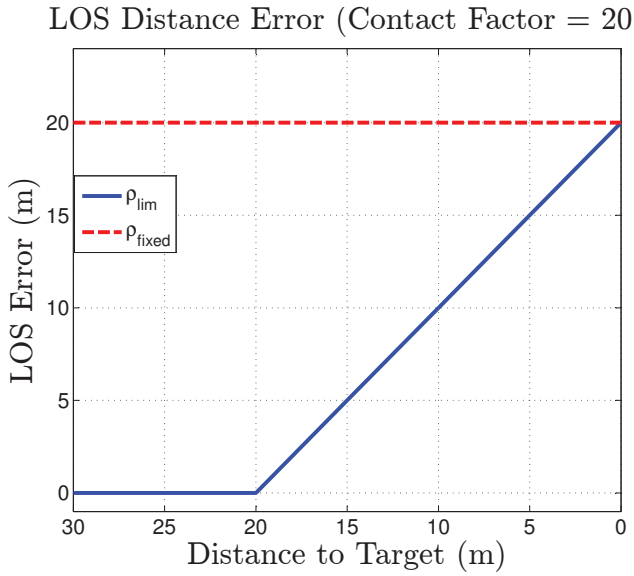

Figure 5.6: Contact factor LOS distance error comparison.

distance method or the method that does not allow ρ to become smaller than a pre-determined value showed the best performance in rendezvous and docking simulations.

To demonstrate the benefit of using the contact factor in a docking scenario, a Monte Carlo simulation was constructed using the previously described six-degree-of-freedom aerodynamic model. The parameters for the docking engagement were: seeker begins 20 m above, 20 m to the side, and 35 m behind the drogue. The drogue is traveling on a straight path with gaussian drogue movement that has a standard deviation of 0.1 m. There is a cross wind of 5 m/s and an updraft of 1 m/s. The drogue is moving at 14 m/s and the seeker is closing at 2 m/s. Fifty simulations were run for the scenario where the seeker used a distance-limited contact factor of 20 m, and fifty simulations without using the contact factor. Histograms for both scenarios are shown in Figure 5.7.

The mean miss distance without using the contact factor was 1.53 m. However, using a contact factor of 20 m, the mean miss distance was 0.098 m. This miss distance is a factor of 15 smaller when using the contact factor in visual pursuit.

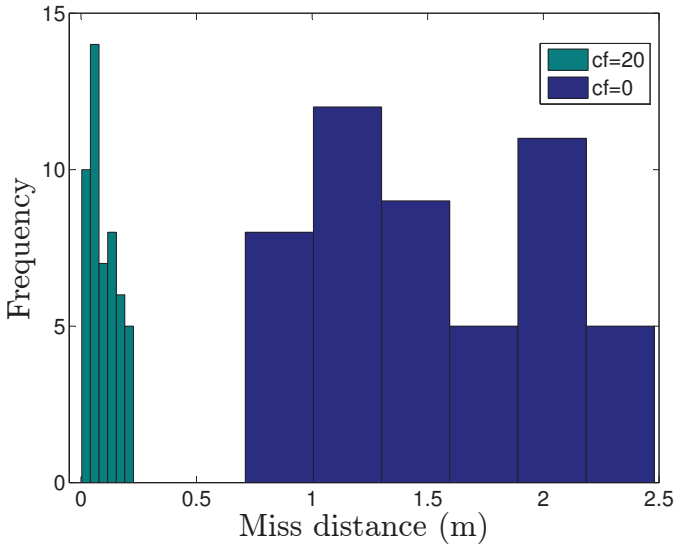

Figure 5.7: Docking performance comparison using the contact factor. Fifty simulations using the contact factor and fifty simulations without using the contact factor.

5.5 Chapter Summary

In this chapter we have used the visual pursuit method developed in Chapter 4 to perform aerial rendezvous and docking with a passively towed drogue. The drogue is towed by a mothership using a flexible nylon cable system. We have shown results from flight trials where the drogue was tracked and docking was attempted by the seeker. A modification to the visual pursuit method for operating in close proximity to the target vehicle was developed to improve docking performance. The modification involved extending the LOS vector ρ through the target to a point beyond the target. This improvement did not change the validity of the stability proof provided in Chapter 4 and ensured that the value of ρ used in the guidance algorithms would never get close enough to zero to cause control saturation. Simulation results showed that limiting ρ to a minimum value was the most effective method for achieving wings-level docking performance. Miss distances were shown to be more than an order of magnitude lower when the seeker used the contact factor for docking.

CHAPTER 6. ADJOINT ANALYSIS OF AERIAL DOCKING SYSTEM

6.1 Introduction

The objective of this chapter is to explore the effects of aircraft design characteristics and target motion on the performance of visual pursuit. Up to this point we have shown the development of a nonlinear guidance method that is suitable for aerial tracking and rendezvous. Now we wish to look at how control gains, roll and pitch rate time constant, airspeed, and sensor delay interact with seeker closing velocity and drogue movement to effect aerial docking accuracy.

Zarchan addressed the performance of air-to-air and ballistic missiles against maneuvering targets using the adjoint method for analysis [4, 39]. He created adjoint systems from the control block diagrams that were effective in separating the contributions of step, oscillatory, and stochastic target motion on the accuracy of the missile engagement [40]. We have adopted a similar approach by creating adjoint systems from linearized guidance models.

In this chapter we first describe the linearization of the visual pursuit guidance methods developed in Chapters 4 and 5. We compute the transfer functions for the linear systems to study model stability by evaluating the root locus plot with respect to changes in aircraft system characteristics. From the system block diagrams we develop adjoint systems to analyze the individual effects of system time constant, sensor time delay, airspeed, and closure velocity on aerial docking. Finally, we look at a comparison of model performance for small and large UAS.

6.2 Linearization and Model Simplification

The first step in the analysis process is to linearize the guidance models developed in Chapter 4. We are utilizing visual pursuit for docking and therefore we are linearizing about the center of the image frame such that η and β are minimized making the small angle approximation an appropriate technique for linearization. This approximation method assumes that, for small angles,

the sine or tangent of an angle can be approximated by the angle itself and the cosine of an angle can be approximated by unity. The error induced by linearization is 2 percent for an angle of 20 deg and about 9 percent for an angle of 40 deg. For the aerial rendezvous scenario, when the seeker is maneuvering within 30 m of the target, the roll and bank angles are almost always under 40 deg and usually under 20 deg. After linearization, the longitudinal control from (4.26) becomes

$$q^c = \frac{V_T)(\theta+\beta) - V_S(\theta+\beta+\gamma)}{\rho} + K_\theta \beta. \tag{6.1}$$

After setting ν in (4.33) to zero, the linearized lateral control becomes

$$\phi^c = \left[\frac{V_S}{g}\left(\frac{V_S}{\rho}\eta - \frac{V_T}{\rho}(\psi_S - \psi_T + \eta) + K_\phi \eta\right)\right]. \tag{6.2}$$

We make an additional assumption for the lateral model that the target heading is constant at 0 deg. For both models we use the minimum-distance contact factor according to

$$\rho = \begin{cases} \rho & \text{if } \rho > \rho_{lim} \\ \rho_{lim} & \text{otherwise,} \end{cases} \tag{6.3}$$

as explained previously in Chapter 5. A comparison of the linear and nonlinear guidance models is shown in Figure 6.1. For both examples the target was offset from the seeker by 10 m laterally and longitudinally. The effect of linearization on LOS tracking performance can be seen in Figure 6.1. The linearized models track the full non-linear method well.

Using Mason's Rule [51], the guidance system block diagrams can be consolidated into a single transfer function for the longitudinal guidance system and a single transfer function for the lateral guidance system. Mason's rule requires computing the transfer function for each forward path G and each feedback loop L. If all of the feedback loops touch the forward path, the overall transfer function can be represented by

$$\mathbf{TF} = \frac{\sum_{i=1}^{n} G_i}{1 - \sum_{j=i}^{m} L_j}, \tag{6.4}$$

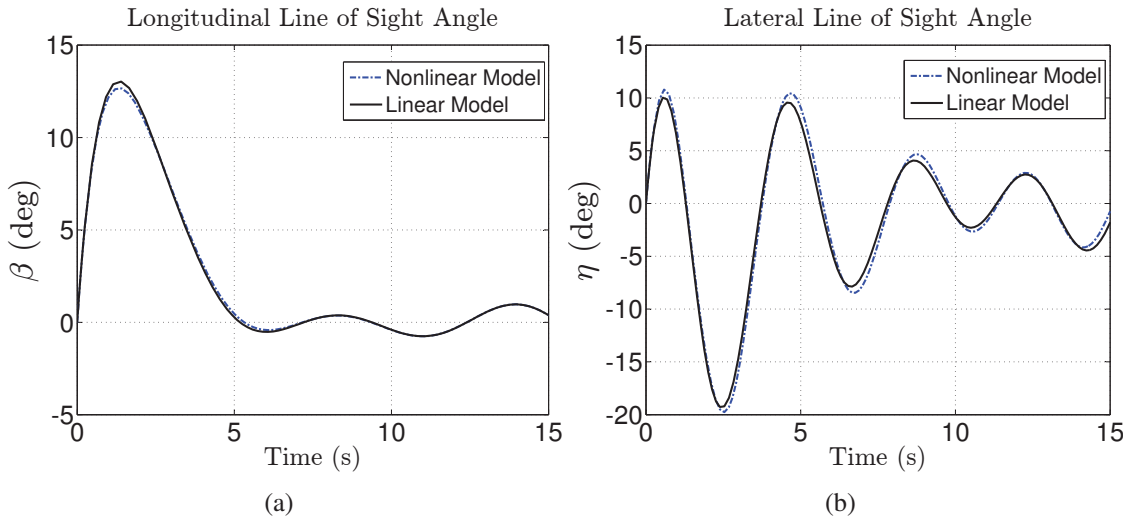

(a) (b)

Figure 6.1: Comparison of linear and nonlinear models. The target is offset from the seeker by 10 m in altitude and 10 m laterally; (a) Longitudinal comparison; (b) Lateral Comparison.

where n is the number of forward paths and m is the number of feedback loops. The poles of the characteristic equation in the transfer function determine the closed loop stability of the system.

6.2.1 Linear Longitudinal Guidance Model

The linearized block diagram for the lateral guidance system can be seen in Figure 6.2. The input to the model is the target altitude. To provide a calculation for the line of sight distance ρ, the model is run using the formulation, $\rho = V_C(T_f - t)$, where V_C is the seeker closing velocity and T_f is the flight time until docking. Therefore, $(T_f - t)$ is the time to go until docking.

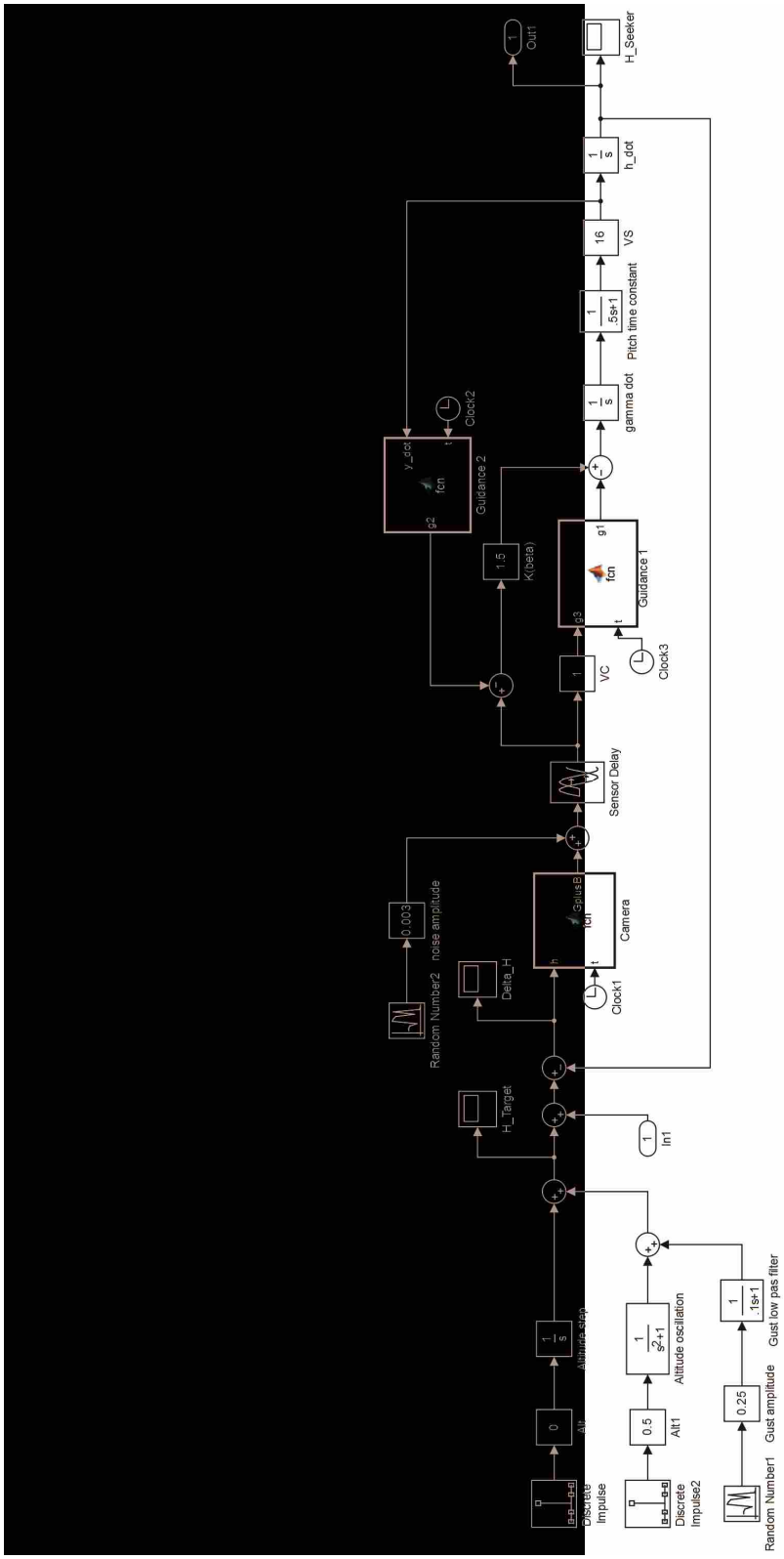

Figure 6.2: Linearized longitudinal guidance system.

Neglecting sensor delay for now, in the longitudinal guidance method shown in Figure 6.2. There are two forward paths and three feedback loops,

$$\begin{aligned} G_1 &= \frac{-V_S}{V_C T_f^2(\tau s+1)s^2} \\ G_2 &= \frac{K_\theta V_S}{V_C T_f(\tau s+1)s^2} \\ L_1 &= \frac{-K_\theta V_S}{V_C T_f(\tau s+1)s^2} \\ L_2 &= \frac{V_S}{V_C T_f^2(\tau s+1)s^2} \\ L_3 &= \frac{-K_\theta V_S}{V_C T_f(\tau s+1)s}. \end{aligned}$$

Inserting these values into equation (6.4), the overall transfer function for the linearized longitudinal guidance algorithm that relates the seeker altitude H_S to the target altitude H_T is

$$\frac{H_S}{H_T} = \frac{\frac{V_S}{V_C T_f \tau}\left[K_\theta - \frac{1}{T_f}\right]}{s^3 + \frac{1}{\tau}s^2 + \left[\frac{K_\theta V_S}{V_C T_f \tau}\right]s + \frac{V_S}{V_C T_f \tau}\left[K_\theta - \frac{1}{T_f}\right]}. \tag{6.5}$$

6.2.2 Linear Lateral Guidance Model

The linearized block diagram for the lateral guidance system can be seen in Figure 6.3.

Similarly, for the lateral guidance model with zero sensor time delay, analyzing the block diagram shown in Figure 6.3, it can be seen that there is one forward path and three feedback loops,

$$\begin{aligned} G_1 &= \frac{V_S}{V_C T_f(\tau s+1)s^2}\left[K_\phi + \frac{1}{T_f}\right] \\ L_1 &= \frac{-V_S}{V_C T_f(\tau s+1)s^2}\left[K_\phi + \frac{1}{T_f}\right] \\ L_2 &= \frac{-V_T}{V_C T_f(\tau s+1)s} \\ L_3 &= \frac{-V_T}{V_C T_f(\tau s+1)s}\left[K_\phi + \frac{1}{T_f}\right]. \end{aligned}$$

Inserting these values into equation (6.4), the overall transfer function for the linearized lateral guidance algorithm that relates the seeker lateral position in the inertial frame Y_S to the target

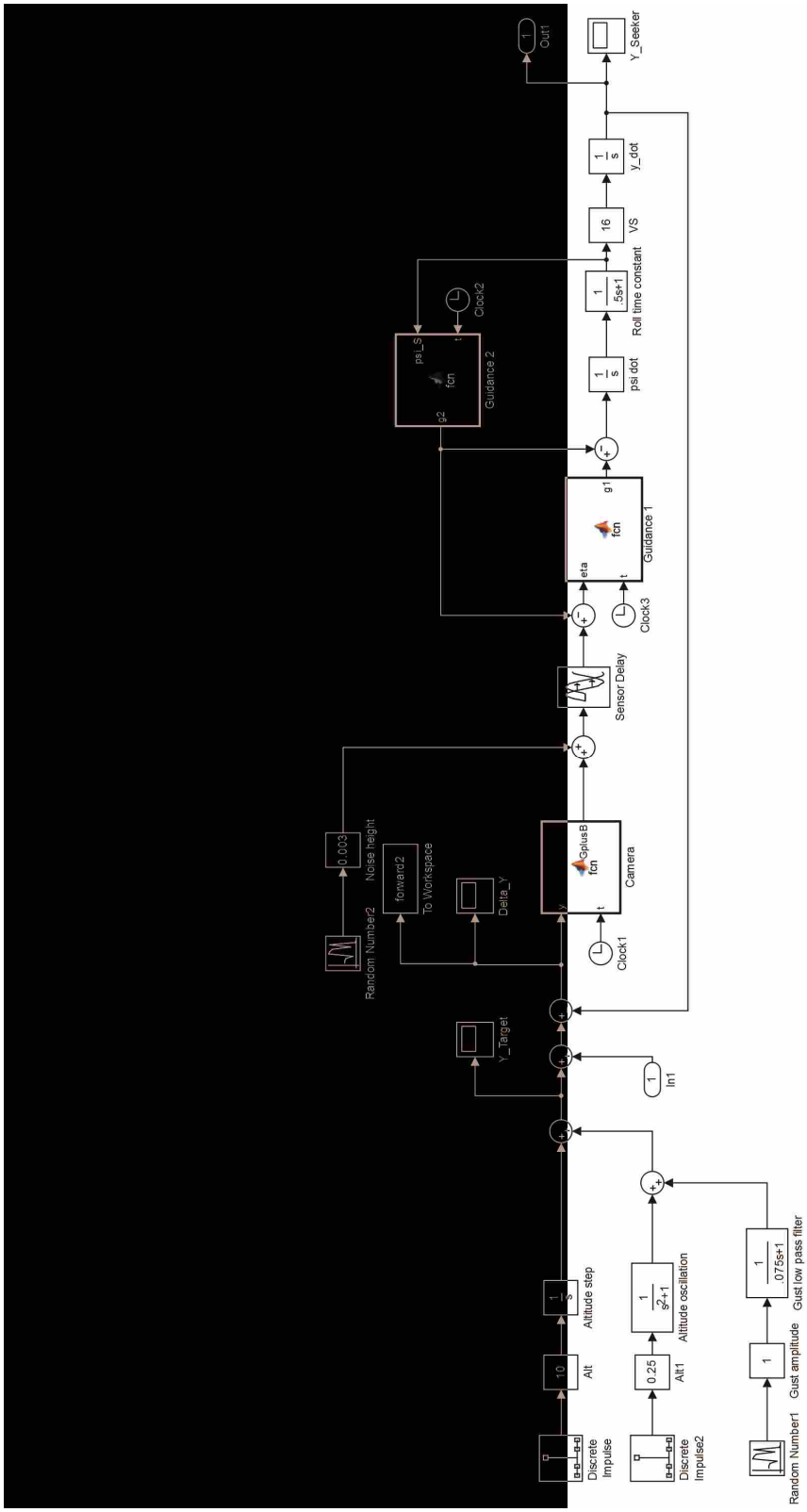

Figure 6.3: Linearized lateral guidance system.

lateral position Y_T is

$$\frac{Y_S}{Y_T} = \frac{\frac{V_S}{V_C T_f \tau}\left[K_\phi + \frac{1}{T_f}\right]}{s^3 + \frac{1}{\tau}s^2 + \frac{V_T}{V_C T_f \tau}\left(1 + \left[K_\phi + \frac{1}{T_f}\right]\right)s + \frac{V_S}{V_C T_f \tau}\left[K_\phi + \frac{1}{T_f}\right]}. \tag{6.6}$$

6.2.3 Model Stability

Since we have reduced each complex system block diagram to a single transfer function for lateral guidance and a single transfer function for longitudinal guidance we can evaluate the stability of the methods by looking at the roots of the characteristic equations. Plotting the roots on the real and imaginary axes of the root locus gives a visual representation of the stability and system damping. Watching how the roots move with changes in the system factors noted above determines the stable operating range of the methods. Beginning first with the system gains K_ϕ and K_θ and a representative set of system characteristics shown in Table 6.1, we examine the root locus plots for gains between zero and infinity in Figure 6.4.

Table 6.1: Nominal system variables

Seeker airspeed	16 m/s
Closing velocity	1 m/s
Roll time constant	0.5
Pitch rate time constant	0.5
Sensor time delay	0

Instability in the longitudinal model occurs at values of K_θ well below the anticipated operating range of the system. The lateral guidance model has no values of K_ϕ that make the system unstable. The increased stability of the lateral model in comparison with the longitudinal model over the range of gains shown is probably because the lateral model has a loop that feeds back a function of heading into heading rate. This loop acts as damping feedback where the longitudinal model does not have a similar feedback loop. The guidance models used here for analysis also do not consider the intrinsic aerodynamic stability of the air vehicle. For analysis, the

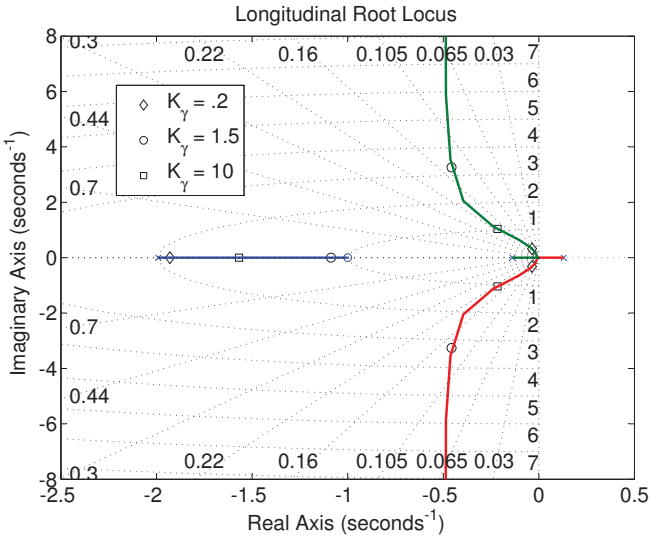

(a)

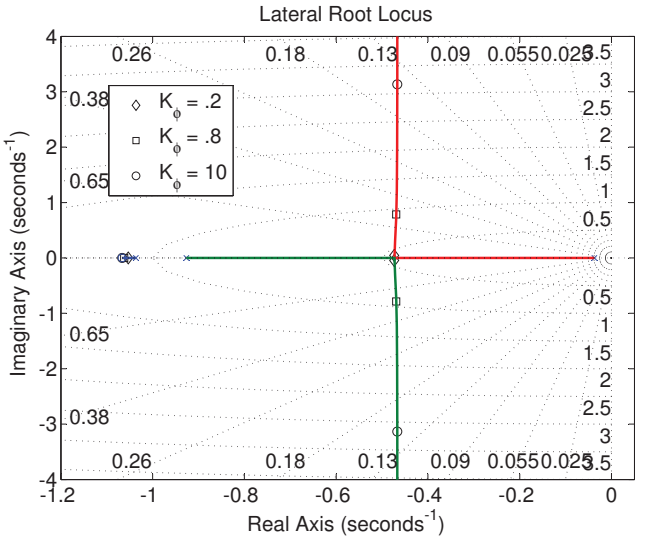

(b)

Figure 6.4: Stability of linearized closed loop guidance system, $V_S = 16\,\text{m/s}$, $V_C = 1\,\text{m/s}$, $T_d = 0$, $K_\theta = 1.5$, $K_\phi = 0.8$; (a) Longitudinal guidance; (b) Lateral guidance.

baseline gains were chosen to be $K_\theta = 0.8$, and $K_\phi = 1.5$. These values have acceptable damping and are near the gains used in the flight trials described in Chapter 5.

6.3 Method of Adjoints

When the guidance models shown in Figures 6.2 and 6.3 are run in Matlab, we can determine a longitudinal and lateral miss distance, or the distance of the seeker centerline from the drogue centerline at contact. As parameters like roll time constant, pitch time constant, sensor delay or others are changed, the simulation can be re-run and the miss distance for that particular scenario and engagement time can be determined. To gain an understanding of how each of the parameters effect performance, thousands of simulated engagements must be run and the data compiled through individual runs or a large Monte Carlo simulation. The adjoint method allows the simulation to be run backward in a sense and, for a given configuration, miss distances for all flight times for the particular docking engagement can be determined in a single simulation. This is the reason for employing adjoints in this dissertation.

Figure 6.5 shows how a single run of an adjoint simulation can represent an infinite number of forward simulations. The trace along the total time axis is the maximum miss distance output from a single run of the adjoint simulation based on a sudden drogue change of 10 m in the lateral direction and sinusoidal motion with an amplitude of 0.25 m and a frequency of 1 rad/s. The traces on the time to go axis are miss distance time histories from maneuver start until docking. The docking engagement times were between 3 and 15 s. The distance between the seeker and the drogue when the maneuver begins is a function of the total time of the docking maneuver. As can be seen in Figure 6.5, the final miss distances for each of the docking maneuvers match the maximum miss distance predicted by the adjoint trace. In this way, a single run of the adjoint simulation can represent the final miss distance from an infinite number of docking maneuvers.

To illustrate the basis for the adjoint method, consider the principle of reciprocity. Laning proposed a thought experiment using a tight string [41]. When the string is depressed at a point A, it will cause a deflection at another point B along the string. If the string is then depressed at B, the deflection at A will be equal to the deflection at point B when pressed at point A. Keeping reciprocity in mind, we consider a linear system that is driven by an impulse. Knowing the impulse, we can then track the behavior of the guidance system over some finite time. However, if we were

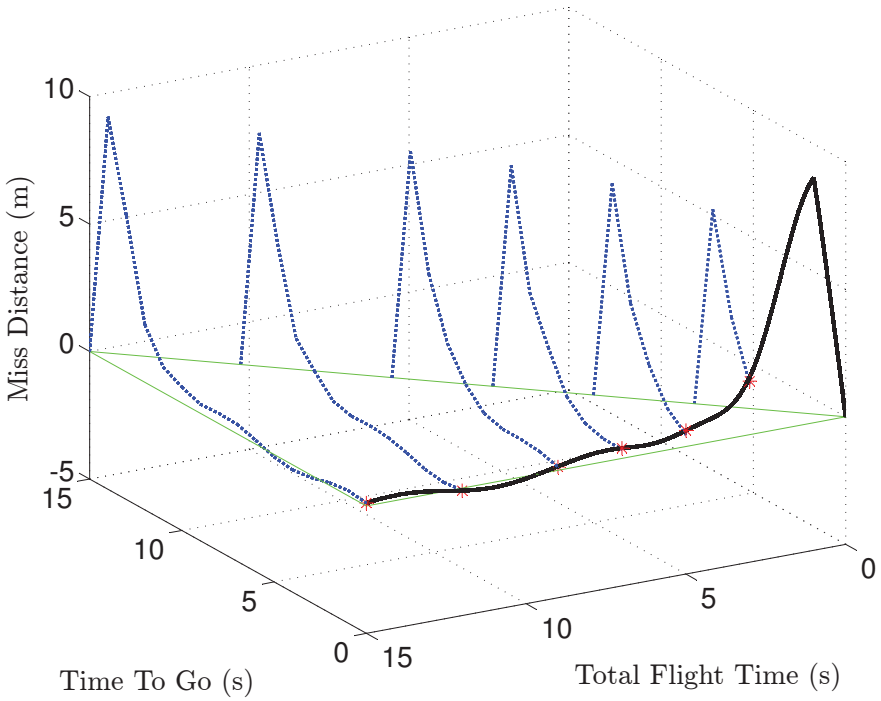

Figure 6.5: Lateral adjoint system.

to reverse this process by applying the impulse at the location of the output we could determine the behavior of the system over all time and in addition see the effects of different system inputs. This method works by converting the system block diagram into an adjoint system by following the rules outlined by Laning and others [41, 43].

1. Convert all system inputs into equivalent systems driven by impulses or white noise processes,

2. Reverse all signal flow directions,

3. Switch all system inputs to adjoint outputs and all system outputs to adjoint inputs,

4. Change all summing points to branch points and all branch points to summing points,

5. Replace time in all time varying elements with adjoint time t^* where $t^* = T_f - t$,

6. Apply an impulse signal to the selected output of the original system,

7. At all the adjoint system stochastic output points, add the adjoint solution sequence to yield the mean square value of the system response.

The system block diagrams from Figures 6.2 and 6.3 are converted into adjoint systems using the method above and are shown in Figures 6.6 and 6.7. Note that the construct of using time to go or $T_f - t$ in the forward simulation now becomes t in the adjoint simulation.

6.4 Target Motion

Examining the adjoint systems in Figures 6.6 and 6.7 it can be seen that there are three types of target motion in the simulation–step, sinusoidal, and stochastic. The effects from target movement can now be observed separately or combined to show the total lateral or longitudinal miss distance. We take each of these types of movement in turn and describe their effect on docking performance.

In Figure 6.8 we see the way step, sine and random target motion are inserted into the adjoint model. The diagram shows a longitudinal engagement, but concept is the same in the lateral direction as well. The seeker is assumed to be on a collision path to the drogue when the maneuver begins (i.e. vehicle centerlines aligned). A step input corresponds to an altitude change or lateral offset. A sine input is the steady-state oscillatory movement of the drogue with a characteristic frequency ω and amplitude A. A stochastic input is the random movement of the drogue due to wind gusts or turbulence. The height of the disturbance is also indicated by the amplitude A. Considering first a step input alone. A step with a value of 10 in the lateral or longitudinal models represents an altitude increase of 10 m or a horizontal offset of 10 m. Flight time can be thought of as the initial separation between the seeker and the drogue at the start of the target movement.

Step target motion

In Figure 6.9 we compare the step input from the forward model in Figure 6.2 to the miss distance output from the adjoint model from Figure 6.6 due to a 10 m altitude maneuver by the drogue.

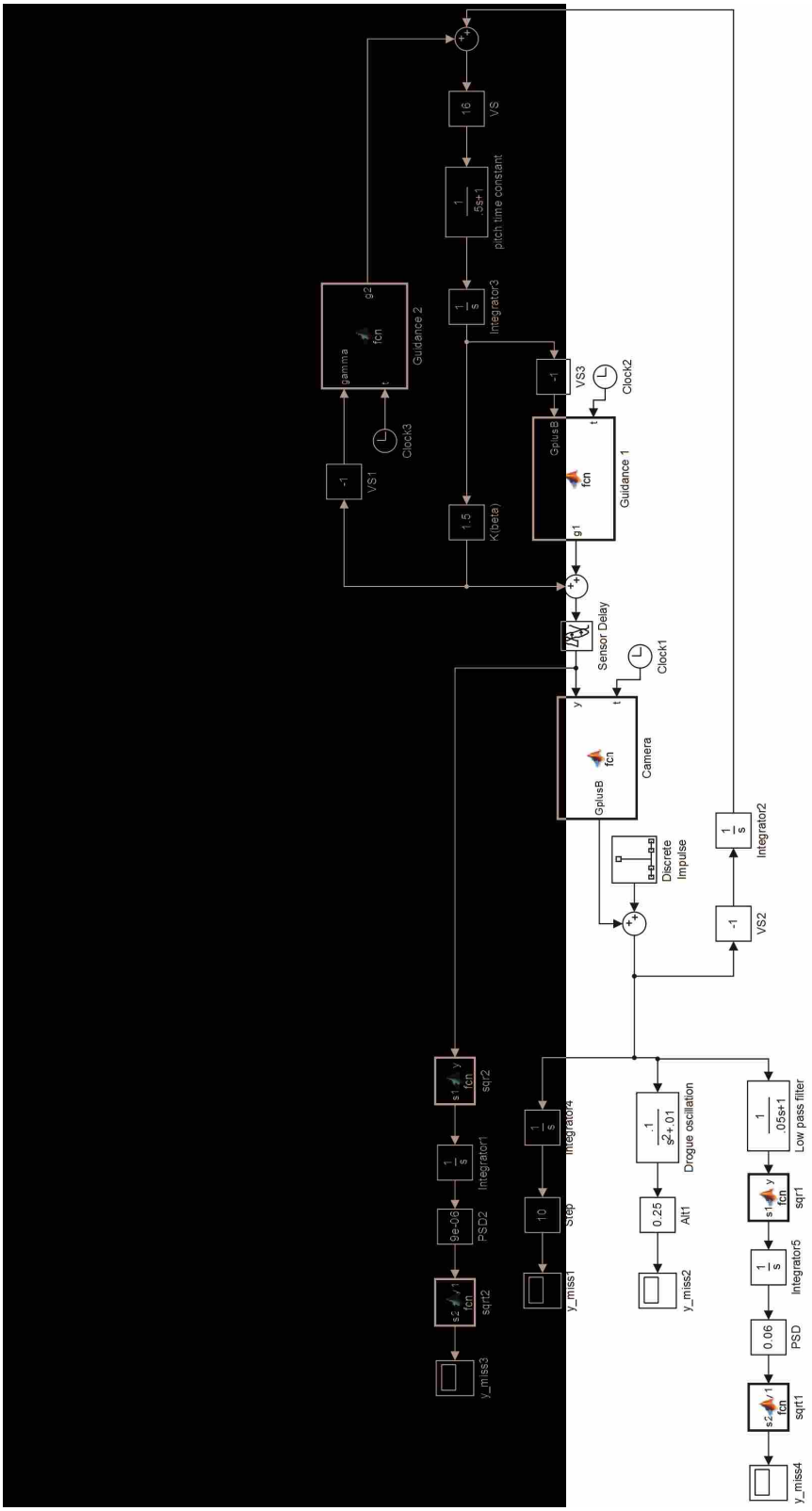

Figure 6.6: Longitudinal adjoint system.

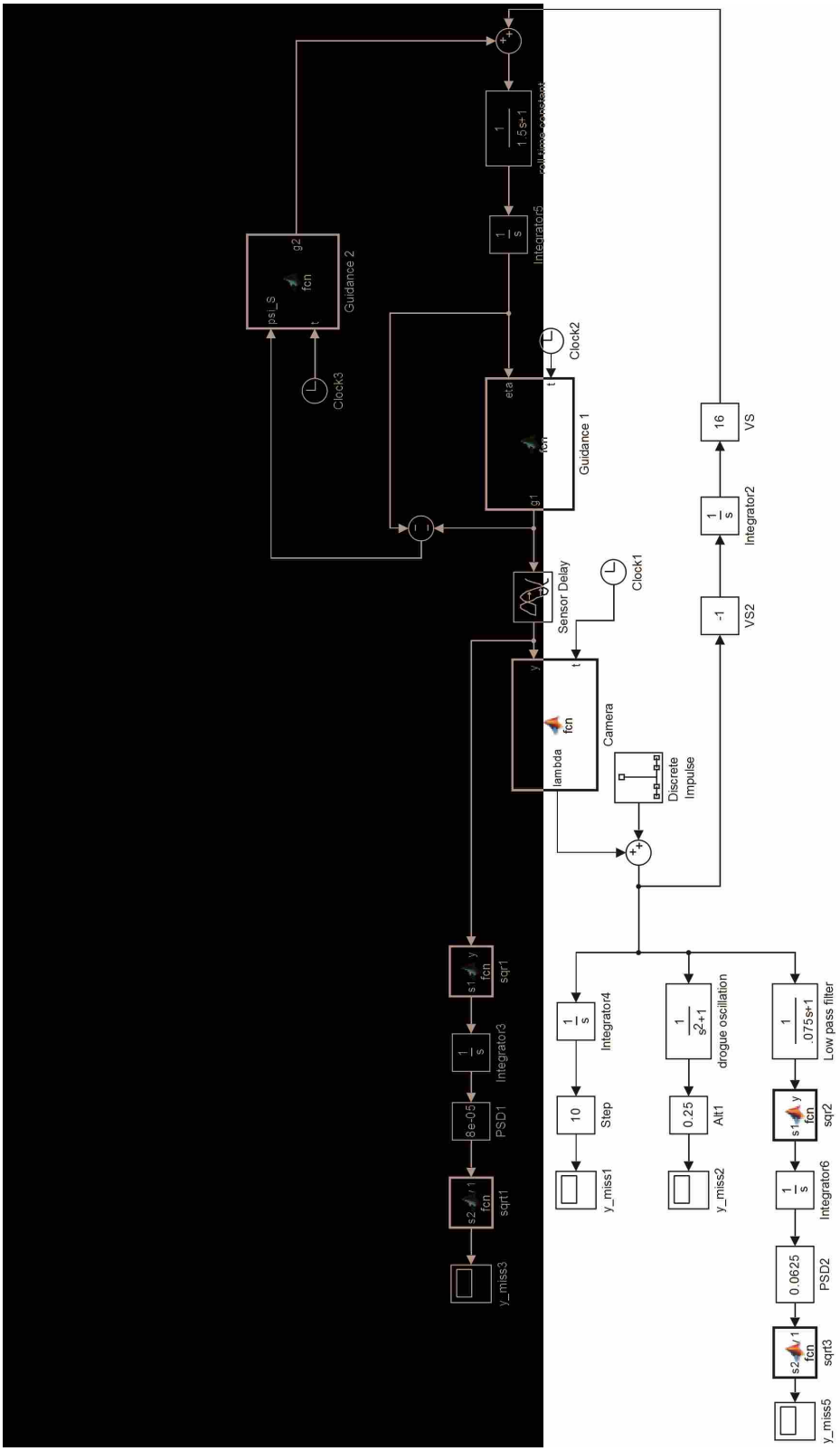

Figure 6.7: Lateral adjoint system.

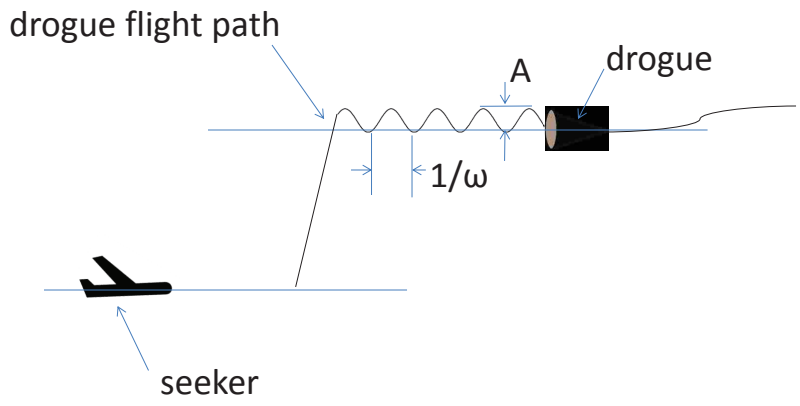

Figure 6.8: Longitudinal step and sine target motion.

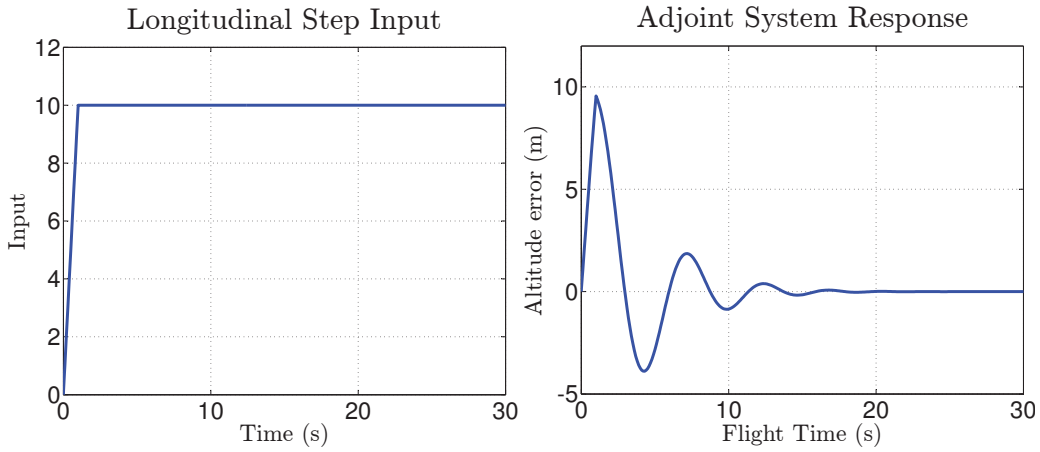

(a) (b)

Figure 6.9: Response to target step input; (a) longitudinal target movement; (b) adjoint system response for miss distance due to longitudinal target step motion.

Examining the adjoint output in Figure 6.9(b), the docking miss distance can be seen for time of flight events from 0 to 30 s. The miss distance for a flight time of 2 s would peak above 9 m and decline to zero at 20 s. The overshoot and damping characteristics are a function of the aircraft design characteristics. These effects will be explained later, but for this example case, any docking attempt for a 10 m altitude step that occurs more than 20 s prior to rendezvous will have

zero miss distance. There is no limit to the flight time that can be simulated. The input and output characteristics are similar for the lateral model.

Sinusoidal target motion

With respect to a sine input, we refer back to Figure 6.8 and look at the steady-state oscillatory portion of the drogue path. Taking the target motion from Figure 6.2 and examining the miss distance from the adjoint simulation in Figure 6.6, we compare the target input to the system response in Figure 6.10. It can be seen that a drogue oscillation with an amplitude of 0.5 m and a frequency of 1 rad/s causes a periodic miss distance response with the same frequency but with a different amplitude.

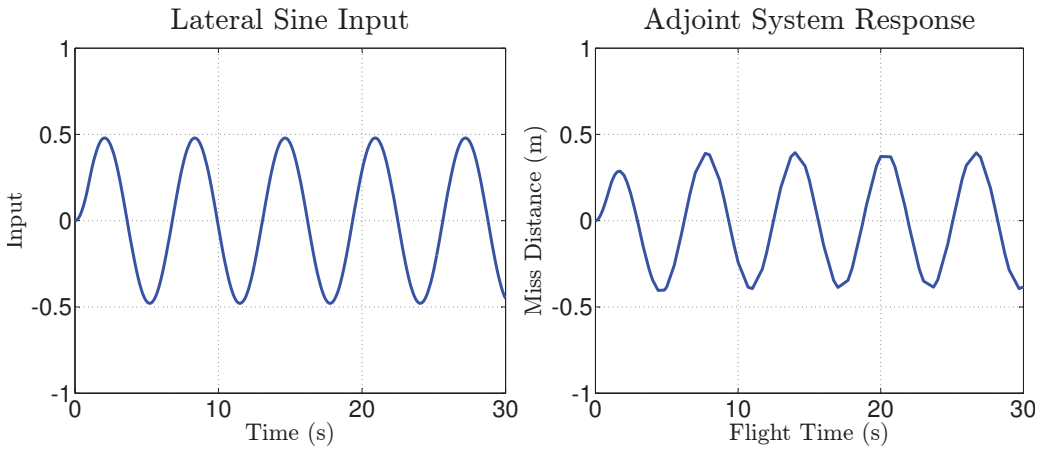

(a) (b)

Figure 6.10: Response to sinusoidal target input; (a) longitudinal target movement; (b) adjoint system response for miss distance due to lateral target sine motion.

The result of the sine input shows that if the oscillation begins when the drogue is very close to the seeker (i.e. short time of flight), the miss distance is small. After a short transitory period, the miss distance becomes periodic with a maximum miss distance indicated by the peak of the miss distance trace. This difference is important because this is where the interaction between drogue oscillation and seeker maneuverability can be seen. It will be shown in the results for maneuverability that when the drogue oscillation frequency is low the seeker generally hits the

drogue with little miss distance, at frequencies higher than the system time constant the maximum miss distance becomes the amplitude of the drogue oscillation. This is because at high frequencies the seeker cannot keep up with the movement of the drogue and the actual miss distance can be anywhere from zero to a maximum of the amplitude of the drogue oscillation as can be seen in Figure 6.10. In the analysis of the performance of the models, steady-state maximum miss distance is used to compare performance with respect to different seeker and drogue characteristics.

Stochastic target motion

Now considering a stochastic or random target motion. This occurs when wind gusts and turbulence buffet the drogue in an unpredictable way. A little of this type of motion is always present in actual flight. To simulate the system response to random target motion we rely on the work of Zarchan [39] and Bucco [43] who showed that random white noise can be represented in the adjoint system according to

$$E\left[y_t^2\right] = \Phi_0 \int_0^{T_f} \left[\mathbf{w}^*(n,0)\right]^2 \mathrm{d}n, \tag{6.7}$$

where $E\left[y_t^2\right]$ is the square of the expectation or RMS miss distance, Φ_0 is the power spectral density, and $\mathbf{w}^*$ the output of the adjoint system. The Simulink representation for random noise can be seen in Figure 6.11.

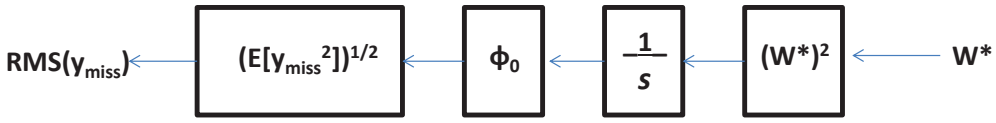

Figure 6.11: Adjoint system for white noise.

To demonstrate the effect of random target motion on miss distance consider a representative scenario as shown in Table 6.2.

The resultant mean miss distance due to random target motion is shown in Figure 6.12. Random target motion may be due to turbulence or gusts and is approximated with low pass fil-

Table 6.2: Nominal system variables

Seeker airspeed	16 m/s
Closing velocity	1 m/s
Roll time constant	1.0
Sensor time delay	0

tered white noise. The power spectral density can be approximated as the variance of a Gaussian distribution with zero mean [52]. If we assume the gust disturbance amplitude is equal to the standard deviation of the random motion, and has a value of 0.25 m, the power spectral density is $\Phi = 0.0625 \mathrm{m}^2/\mathrm{Hz}$. The value of Φ is computed by squaring the maximum noise height.

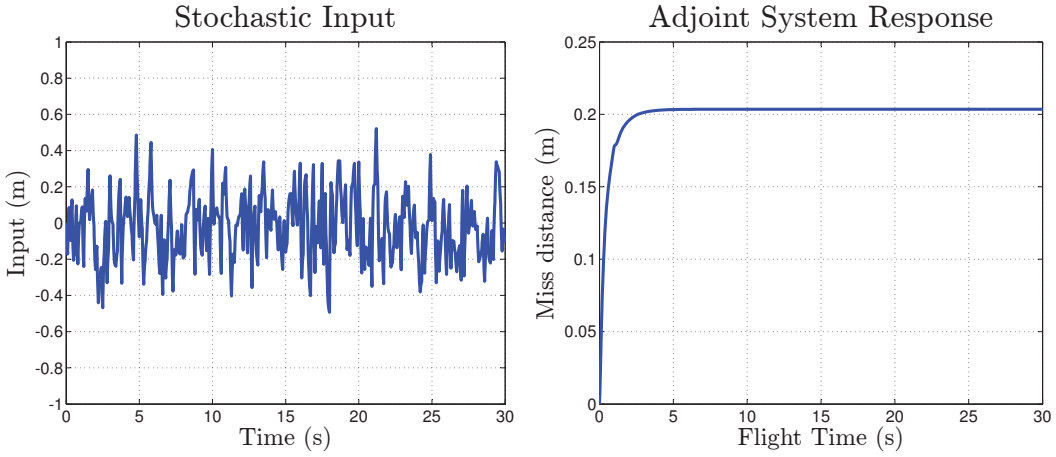

(a) (b)

Figure 6.12: Response to stochastic target input; (a) target random walk due to turbulence; (b) adjoint system response for miss distance due to lateral random target motion.

It can be seen that for any rendezvous attempts longer than 4 s, the mean miss distance due to random target movement is constant at 81 percent of the maximum noise height. Miss distances due to stochastic target motion, typically caused by turbulence, showed similar trends when compared with sinusoidal target motion as seeker and drogue motion characteristics were changed. These trends will be discussed in detail in later sections for sinusoidal motion. However, for stochastic motion the range of miss distances was quite small. For lateral motion the maximum

mean miss distances varied between 80 and 95 percent of the gust noise height for all combinations of airspeed, closing velocity, roll time constant, and sensor delay. For longitudinal target motion, the maximum mean miss distances were between 95 and 101 percent of the noise height for all combinations of seeker characteristics and target maneuver.

Total target motion

Combining the effects of step, sine, and random target motion miss distances from the adjoint simulations gives the combined miss distance. To verify the accuracy of the adjoint systems, the results from several runs of the forward simulations for different times of flight are compared with a single run of the adjoint system. As can be seen in Figure 6.13(a), the results from combined step and sine target motion match the adjoint simulation very well. Figure 6.13(b) shows the results from the adjoint simulation plotted with a Monte Carlo simulation of the basic guidance model. For each point shown in Figure 6.13(b), 50 forward simulations are averaged against random target motion representing gusts on the drogue. This figure shows that the adjoint simulation can calculate consistent results against random target motion. The adjoint simulation will be used for comparing performance for different combinations of aircraft and target characteristics. The

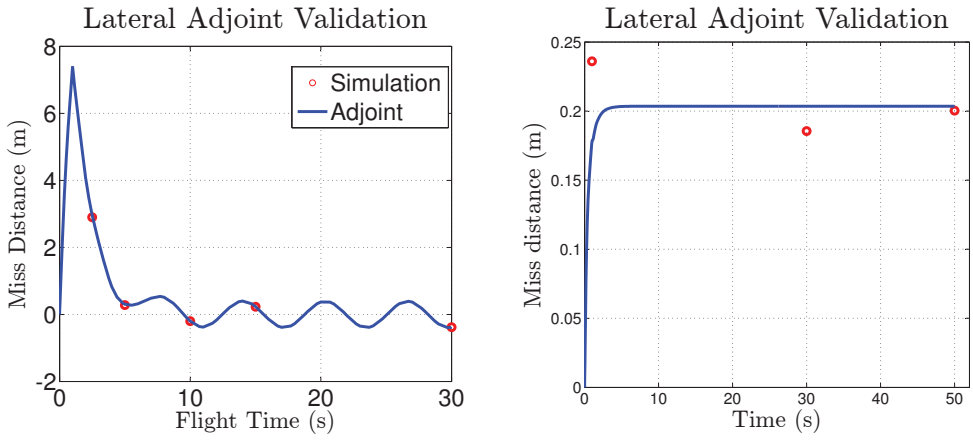

(a) (b)

Figure 6.13: Comparison of adjoint simulation and forward simulation; (a) Combined step and sine input; (b) Stochastic input.

utility of the adjoint method becomes clear when looking at Figure 6.13 and realizing that hundreds of runs using the basic models would be required to produce the single plot in each direction that now shows the miss distance for all rendezvous and docking times for a given set of system characteristics.

6.5 Seeker Maneuverability

Seeker maneuverability is characterized by the system time constant. For example, in the longitudinal direction, the pitch-rate time constant τ represents the time it takes the UAS to achieve the commanded pitch rate. The system time constant includes computation time, control surface actuation time, and aircraft response time. So a $\tau = 0.25\,\text{s}$ would indicate that the UAS would achieve 63 percent of the commanded pitch rate in 0.25 s. In the lateral direction the time constant represents the time it takes the UAS to achieve the commanded bank angle. Taking a representative set of values for the longitudinal and lateral guidance models as shown in Table 6.3, we compute the root locus plots for the longitudinal and lateral models that are shown in Figure 6.14.

Table 6.3: Nominal system variables

Seeker airspeed	16 m/s
Closing velocity	1 m/s
K_ϕ gain	0.8
K_θ gain	1.5
Total time for rendezvous	30 s

For the representative case chosen, both methods are stable. However, system damping decreases as the system time constants increase. In the longitudinal direction, the system is stable for pitch rate time constants up to $\tau = 1\,\text{s}$. Laterally the method is stable for roll time constants up to $\tau = 2\,\text{s}$. However, it will be shown that the performance degrades as the time constants approach the stability limits. Performance analysis of the linearized guidance methods will be restricted to the stable regions.

To compare docking performance, a non-dimensional miss distance parameter called the maximum normalized miss distance has been created by dividing the maximum miss distance after

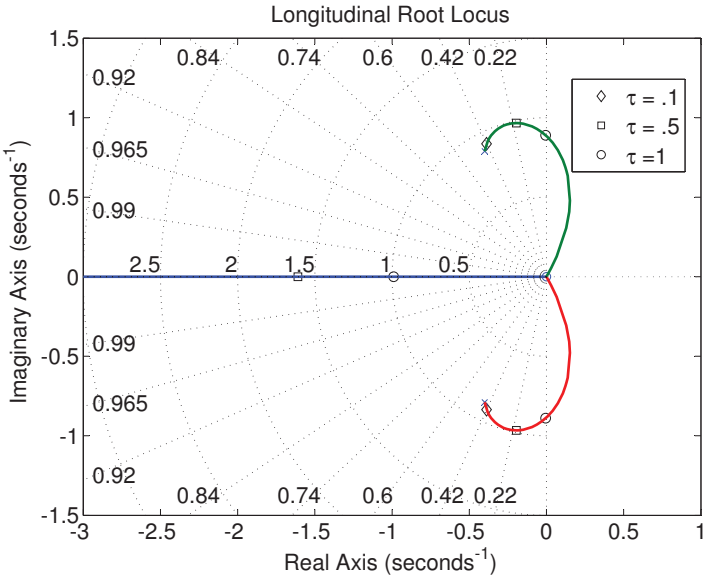

(a)

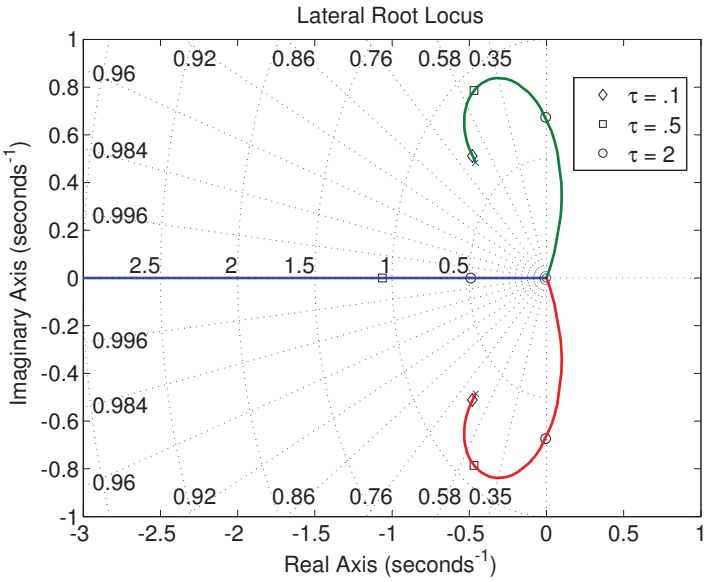

(b)

Figure 6.14: Stability of linearized closed loop guidance system, $V_S = 16\,\text{m/s}$, $V_C = 1\,\text{m/s}$, $\tau_{Lat} = 0.8$, $\tau_{Long} = 1.5$, $T_d = 0$; (a) Longitudinal guidance system; (b) Lateral guidance system.

the transient period y_{miss} by the amplitude A of the drogue oscillation according to

$$y^* = \left(\frac{y_{miss}}{A}\right). \tag{6.8}$$

The longitudinal and lateral adjoint simulations were run using the baseline system parameters shown in Table 6.3 against an oscillating drogue. The drogue frequency was varied between $0.1-30$ rad/s with an oscillation amplitude that varied between $0.1-1$ m. The longitudinal pitch rate time constant was varied between $0.1-0.6$ s and the lateral roll time constant was varied between $0.1-2$ s. The results from all of the adjoint simulations can be seen in Figure 6.15.

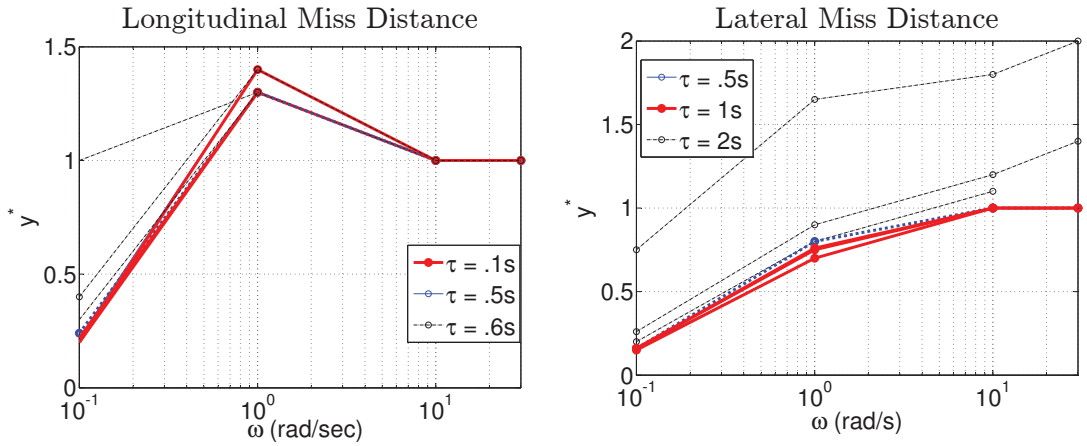

(a) (b)

Figure 6.15: System time constant effect on miss distance, $V_S = 16$ m/s, $V_C = 1$ m/s; (a) Longitudinal guidance system, $K_\theta = 1.5$; (b) Lateral guidance system, $K_\phi = 0.8$.

The data align well for time constants 50 percent below the maximum stable time constants shown in Figure 6.14. For time constants above this level, the data begin to diverge and the effect of drogue oscillation amplitude can be observed in the varied slopes of the miss distance plots. However, for time constants below 50 percent of the maximum stable value, the normalized maximum miss distances fall on top of one another regardless of oscillation amplitude or time constant.

Analyzing the plots we see that at high frequencies the maximum miss distance asymptotes to the amplitude of the drogue oscillation. This is because the seeker can no longer physically fol-

low the rapid drogue movement and the actual miss distance will be a random value between zero and the amplitude of the drogue as was shown in Figure 6.10. When the oscillation frequency and the system time constants are near the same value we see the most variation in performance. It is this combination that produces seeker movement out of phase with the drogue and therefore larger miss distances result. This can be most easily seen in the longitudinal model that is inherently less damped than the lateral model. The phenomena of the maximum miss distance occurring where the target frequency and system time constants are of similar magnitude has also been observed in missile engagements [4]. The best docking performance can be observed, not surprisingly, when the drogue oscillation frequency is very low, or the amplitude is very low. Figure 6.16 is the average y^* versus ω plots for time constants below 50 percent of the maximum stable time constant. These plots will be used as the baseline to compare velocity and sensor delay effects.

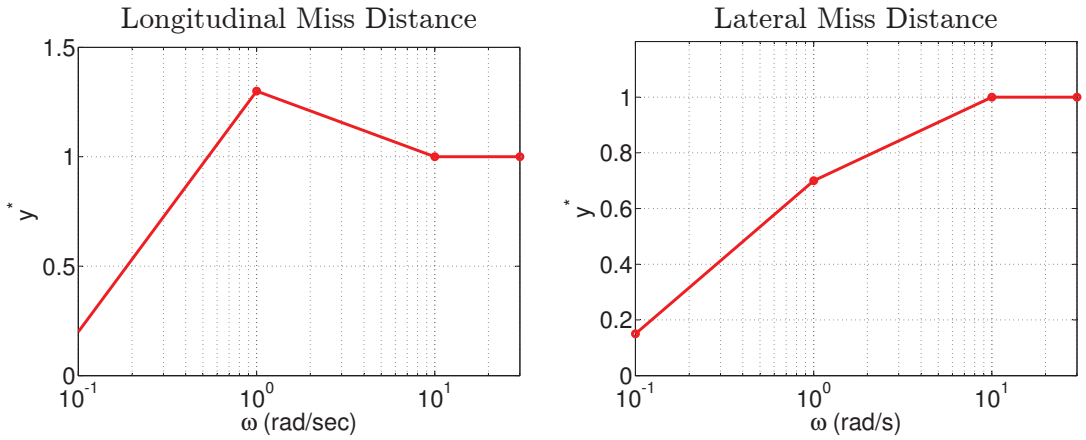

(a) (b)

Figure 6.16: Non dimensional miss distance, $V_S = 16\,\text{m/s}$, $V_C = 1\,\text{m/s}$; (a) Longitudinal guidance system, $K_\theta = 1.5$; (b) Lateral guidance system, $K_\phi = 0.8$.

To calculate the maximum miss distance or maximum lateral and longitudinal offset from the drogue centerline during aerial docking, we use the plots in Figure 6.16. We first find the y^* value for the oscillation frequency and then multiply by the oscillation amplitude to find the actual miss distance.

Example

We will calculate the maximum total miss distance for the scenario where the seeker has the nominal system parameters shown in Table 6.3 and the flight time of the rendezvous attempt is longer than the initial transitory period. The drogue has a known oscillation frequency of 0.5 rad/s with a lateral oscillation amplitude of .25 m, and a longitudinal oscillation amplitude of .1 m. The maximum miss distance in the lateral and longitudinal directions along with the total maximum miss distance is calculated according to

$$\begin{aligned} y_{max} &= y^* * \mathrm{A} \\ y_{lat} &= 0.55 * 0.25\mathrm{m} \\ &= 0.1375\mathrm{m} \\ y_{long} &= 0.95 * 0.1\mathrm{m} \\ &= 0.0950\mathrm{m} \\ y_{total} &= (y_{lat}^2 + y_{long}^2)^{\frac{1}{2}} \\ &= 0.1671\mathrm{m}. \end{aligned}$$

6.6 Velocity Effects

There are two velocity effects to consider–closing velocity V_C, and the seeker airspeed V_S. The difference between the seeker airspeed V_S and the drogue airspeed V_D is the closing velocity V_C.

Closing velocity

First, considering the closing velocity, we examine the effect on stability and performance when increasing V_C from $0.5 - 3$ m/s. Because we are trying to make controlled contact while airborne, V_C out of necessity will be relatively slow. Figure 6.17 shows how the roots of the closed-loop transfer function and maximum normalized miss distance change with increasing velocity.

Looking at Figure 6.17(a), the imaginary roots become more highly damped as closing velocity increases. Looking at Figure 6.17(b) it can be seen that a larger V_C shows slightly lower

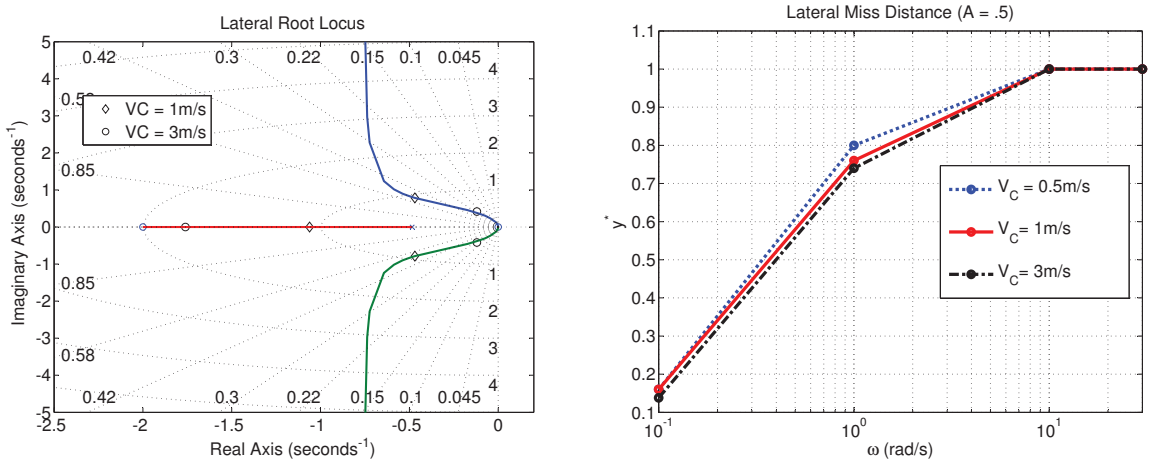

(a) (b)

Figure 6.17: Closure velocity effect on stability and performance; (a) Lateral root locus (b) Lateral normalized miss distance.

miss distances in the middle frequencies where out-of-phase seeker interactions with the drogue can increase miss distance.

Airspeed

The effect of airspeed on the stability and performance can be seen in Figure 6.18. Increasing the airspeed decreases system damping and the oscillation frequency approaching the drogue is higher. Airspeed has a small negative effect on lateral docking performance.

6.7 Sensor Effects

There are two effects on performance that originate with the vision sensor–sensor noise and time delay. We will first consider the effect of noise on miss distance.

Sensor noise

Sensor noise is modeled as a stochastic process and is input into the adjoint system in the same way as random target movement. However, the input location for the noise is at the camera, as can be seen in Figures 6.6 and 6.7. If we assume the noise height is equal to the variance

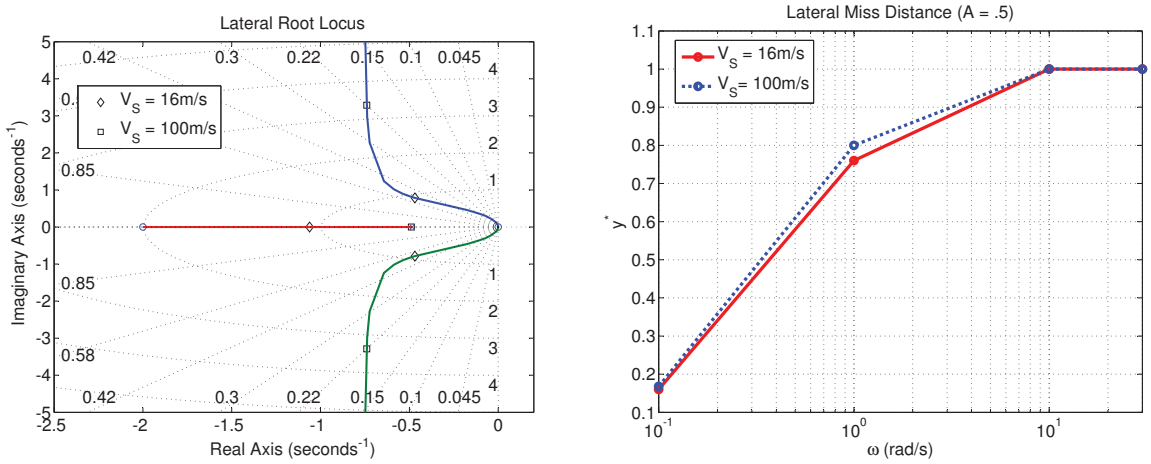

(a) (b)

Figure 6.18: Airspeed effect on stability and performance; (a) Lateral root locus (b) Lateral normalized miss distance.

and has a value of $1/2\,\text{deg}$ or $0.009\,\text{rad}$ on the signal leaving the camera, this would equate to a power spectral density Φ_0 of $0.000081\,\text{rad}^2/\text{Hz}$. The miss distance that correlates to this level of noise for the nominal seeker as described in Table 6.3 is shown in Figure 6.19. The sensor noise

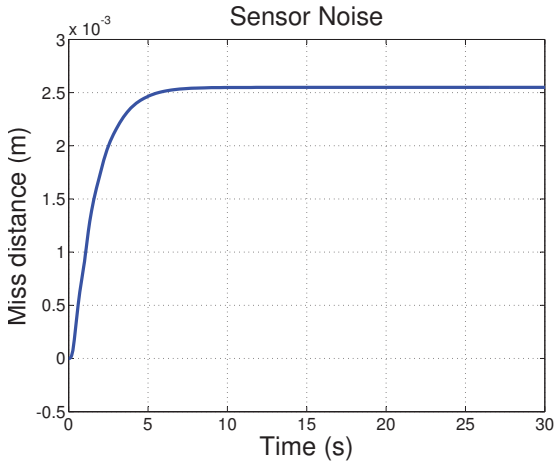

Figure 6.19: Sensor noise effect on miss distance.

creates a miss distance of approximately $2.5\,\text{mm}$ in the lateral direction and a similar value in the

longitudinal direction. This distance is added to the miss distances calculated for target motion to get the total miss distance.

Sensor time delay

We now consider the effect of sensor transport delay on the longitudinal guidance method shown in Figure 6.2. The sensor transport delay includes all of the delay that accounts for where the target is actually located at a moment in time and the location that is perceived by the seeker. These delays are caused by radio frequency transmission and computer processing time in the camera and guidance system. Autopilot and airframe response lags are covered by the aircraft time constants and are not part of sensor delay. We now modify the transfer functions for the two forward paths and three feedback loops in the longitudinal model, by including a first-order Padé approximation for time delay. The forward path and loop transfer functions now become,

$$\begin{aligned} G_1 &= \frac{-V_S}{V_C T_f^2(\tau s+1)s^2}\frac{(2-T_d s)}{(2+T_d s)} \\ G_2 &= \frac{K_\theta V_S}{V_C T_f(\tau s+1)s^2}\frac{(2-T_d s)}{(2+T_d s)} \\ L_1 &= \frac{-K_\theta V_S}{V_C T_f(\tau s+1)s^2}\frac{(2-T_d s)}{(2+T_d s)} \\ L_2 &= \frac{V_S}{V_C T_f^2(\tau s+1)s^2}\frac{(2-T_d s)}{(2+T_d s)} \\ L_3 &= \frac{-K_\theta V_S}{V_C T_f(\tau s+1)s}. \end{aligned}$$

inserting these values into equation (6.4), and setting

$$K_\theta^* = \left[K_\theta - \frac{1}{T_f}\right], \tag{6.9}$$

$$K_\phi^* = \left[K_\phi + \frac{1}{T_f}\right], \tag{6.10}$$

and

$$V^* = V_C T_f. \tag{6.11}$$

The overall transfer function for the linearized longitudinal guidance algorithm with sensor delay is

$$\frac{H_S}{H_T} = \frac{-V_S T_d K_\theta^* s + 2V_S K_\theta^*}{V^* T_d \tau s^4 + V^*(2\tau + T_d)s^3 + (2V^* + K_\theta V_S T_d)s^2 + \left(2K_\theta V_S - V_S T_d K_\theta^*\right)s + 2V_S K_\theta^*}. \quad (6.12)$$

By modifying the transfer function for the linearized lateral guidance model with a first-order Padé approximation for the time delay, the forward path and loop transfer functions become,

$$\begin{aligned} G_1 &= \frac{V_S}{V_C T_f(\tau s+1)s^2}\left[K_\phi + \frac{1}{T_f}\right]\frac{(2-T_d s)}{(2+T_d s)} \\ L_1 &= \frac{-V_S}{V_C T_f(\tau s+1)s^2}\left[K_\phi + \frac{1}{T_f}\right]\frac{(2-T_d s)}{(2+T_d s)} \\ L_2 &= \frac{-V_T}{V_C T_f(\tau s+1)s} \\ L_3 &= \frac{-V_T}{V_C T_f(\tau s+1)s}\left[K_\phi + \frac{1}{T_f}\right]. \end{aligned}$$

Inserting these values into (6.4), the overall transfer function for the linearized lateral guidance algorithm with sensor delay is

$$\frac{Y_S}{Y_T} = \frac{\frac{V_S K_\phi^*}{V^* \tau T_d}(2 - T_d s)}{s^4 + \left(\frac{1}{\tau} + \frac{2}{T_d}\right)s^3 + \left(\frac{V_T}{V^*\tau}\left[1 + K_\phi^*\right] + \frac{2}{\tau T_d}\right)s^2 + \left(\frac{2V_T}{V^*\tau T_d}\left[1 + K_\phi^*\right] - \frac{V_S K_\phi^*}{V^*\tau}\right)s - \frac{2V_S K_\phi^*}{V^*\tau T_d}}. \quad (6.13)$$

In Figure 6.20 we can see the root locus for the transfer functions that now include sensor delay. The longitudinal model is stable up to a sensor delay of 0.5 s, while the lateral model is stable up to a delay of 1 s. However in the region of operation, the sensor delay roots are lightly damped. The performance with sensor delay between 0 to 0.25 s can be seen in Figure 6.21.

Analyzing the plots in Figure 6.21 it can be seen in the lateral plot that sensor delay creates larger miss distances as the delay becomes longer. However, in the longitudinal plot sensor delay appears to act as damping in the mid-frequency range where spikes were observed in the baseline data. Sensor delay shows similar behavior to system time constant even though the mechanisms are different. Like time constant, keeping the sensor delay to 50 percent of the maximum stable time delay provides acceptable system performance.

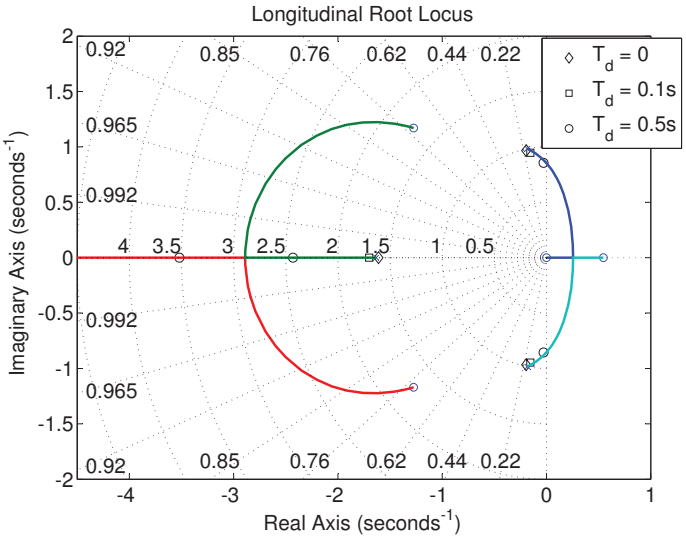

(a)

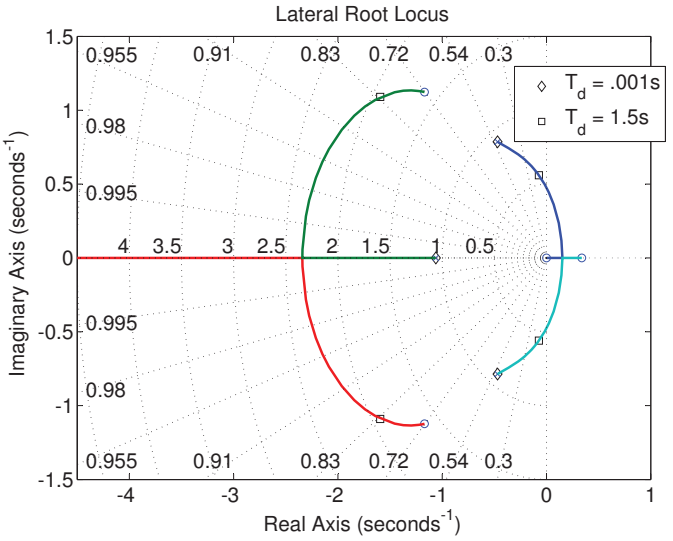

(b)

Figure 6.20: Stability of linearized closed loop guidance system, $V_S = 16\,\text{m/s}$, $V_C = 1\,\text{m/s}$, $\tau_{Lat} = 0.8$, $\tau_{Long} = 1.5$, $K_\theta = 1.5$, $K_\phi = 0.8$; (a) Longitudinal root locus (b) Lateral root locus.

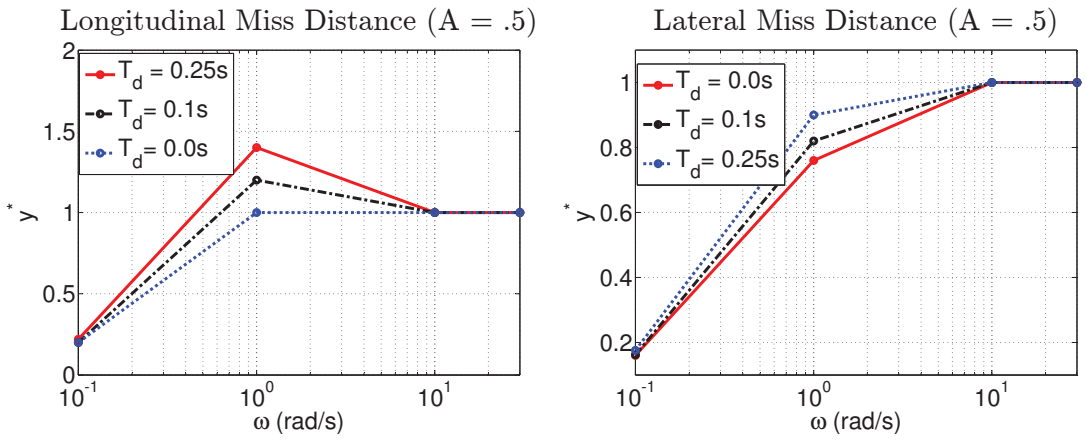

(a) (b)

Figure 6.21: Sensor delay effect on performance; (a) Longitudinal normalized maximum miss distance (b) Lateral normalized maximum miss distance.

6.8 Comparison of Large and Small UAS Performance Using Visual Pursuit

In this section we use the analysis techniques provided in this chapter to evaluate a nominal docking scenario for a small UAS and a large UAS to analyze the suitability of visual pursuit over a wide range of aircraft types. For the small UAS we will use the characteristics of the seeker described in Chapter 2. For the large UAS we will consider a notional aircraft on the scale of the Global Hawk. The Global Hawk has a wing span of approximately 35 m and a takeoff weight approaching 15,000 kg [53] compared with our research UAS that has a 1.4 m wing span and weighs only about 2 kg. The Global Hawk has a cruise airspeed of more than 500 km/hr [53] compared with our research UAS that has a cruise airspeed of around 70 km/hr. Assuming an aerial refueling airspeed of around 360 km/hr or 100 m/s we will compare aerial rendezvous performance using visual pursuit. The notional aircraft and drogue parameters are for a large and small UAS aerial rendezvous are shown in Table 6.4.

The docking system characteristics for the small UAS shown in Table 6.4 are based on known or estimated system characteristics. With respect to the large UAS system characteristics, they are based on estimates of system response time for a long winged aircraft that has additional computing requirements, higher airspeed, smaller closing velocity requirement, and a more stable drogue when compared with the small UAS system. A root locus plot was constructed for the large

Table 6.4: Nominal docking system characteristics

	Small UAS	Large UAS
Wing span	1.4 m	35 m
Takeoff weight	3 kg	15,000 kg
Rendezvous airspeed	16 m/s	100 m/s
Closing velocity	2 m/s	0.5 m/s
K_ϕ gain	0.8	0.8
K_θ gain	1.5	1.5
Roll time constant	0.5 s	2.0 s
Pitch rate time constant	0.1 s	.25 s
Total system time delay	.01 s	.02 s
Vision sensor noise amplitude	0.5 deg	0.5 deg
Total time for rendezvous	30 s	30 s
Target altitude offset	10 m	10 m
Target lateral offset	10 m	10 m
Target oscillation frequency	0.5 rad/s	0.1 rad/sec
Target oscillation amplitude	0.1 m	0.25 m
Gust noise amplitude	0.1 m	0.2 m
Docking accuracy requirement	0.3 m	0.5 m

UAS and it was determined that the maximum stable roll time constant was 4 s which put the nominal roll time constant of 2 s easily within the acceptable performance region. The characteristics from Table 6.4 were put into the adjoint models in Figures 6.6 and 6.7 and the centerline offset distance at docking is recorded in Table 6.5.

Table 6.5: Adjoint docking simulation results

	Small UAS	Large UAS
Lateral step miss distance	0	0
Lateral sine miss distance	0.06 m	0.2 m
Lateral sensor noise miss distance	0.015 m	0.008 m
Lateral gust noise distance	0.18 m	0.19 m
Total lateral miss distance	0.255 m	0.398 m
Longitudinal step miss distance	0	0
Longitudinal sine miss distance	0.08 m	0.035 m
Longitudinal sensor noise miss distance	0.022 m	0.005 m
Longitudinal gust noise distance	0.12 m	0.18 m
Total longitudinal miss distance	0.150 m	0.220 m
Maximum miss distance	0.296 m	0.455 m

The small UAS was operating in the region where the system time constants were very similar to the drogue oscillation frequency. This is the region where target motion can sometimes amplify the target miss distance beyond the oscillation or gust noise amplitude. This was observed as the miss distance due to gust was above the gust noise amplitude. For the large UAS, gust assumptions also played a large roll in the overall miss distance. In addition, the effect of a large roll time constant on the lateral miss distance was seen in the large UAS results. Both systems met their notional docking accuracy requirement which shows that the visual pursuit method can be used over a wide range of UAS design parameters.

6.9 Chapter Summary

In this chapter we have shown that visual pursuit can be linearized for analysis. By creating full system transfer functions, we have shown how time constant, velocity and sensor delay effects can be evaluated to determine the range of values that are stable. We have also introduced the method of adjoints for analyzing the performance of step, sine and stochastic drogue motion. We have shown that the time constant is not a factor in miss distance as long as the time constant remains below 50 percent of the maximum stable value. Drogue oscillation amplitude effects can be incorporated into the miss distance by using the normalized maximum miss distance y^* parameter. Out-of-phase interactions between the seeker and the drogue are most likely to occur at frequencies near the system time constant. In a lightly damped system (like the linearized longitudinal model) these interactions can produce miss distance in excess of the amplitude of the drogue motion. When the drogue oscillation frequency is high, the maximum miss distance asymptotes to the drogue oscillation amplitude regardless of other system characteristics. Raising the seeker airspeed is likely to increase miss distances slightly while increasing the closure rate is likely to decrease miss distance slightly. Sensor time delay creates miss distance behavior similar to changes in the system time constant as long as the time delay remains in the stable region. The roots of the time delay transfer function are in a very lightly damped region of the root locus and therefore time delays in excess of 0.1 s effect docking performance negatively. It was shown that random noise or gust effects on the drogue movement can have a dominant effect on miss distance. Finally, it was shown that visual pursuit is an effective method of aerial rendezvous for both small and large UAS.

CHAPTER 7. CONCLUSIONS AND FUTURE WORK

7.1 Summary of Main Results

The motivation for the research was the desire to develop a vision-based guidance method that would be useful for autonomous air-to-air tracking and rendezvous. Three aerial rendezvous methods were developed and tested. The first was a non-visual method that was produced using vector fields. This method is useful for flying in formation with another aircraft when the seeker has no sensor for detecting the other aircraft. When the target aircraft a flying along a known trajectory and distance to target can be determined through GPS or some other method, both aircraft can remain in lose formation with one another using the vector-field method. The second method was a proportional-integral method that used only line-of-sight angles for guidance. This method requires no communications with the target aircraft. The final method, called visual pursuit, was nonlinear and is useful with a fully cooperating target that is able to relay position, velocity and heading. Visual pursuit is Lyapunov-stable and performs well at tracking from a set standoff distance as well as docking with an aerial drogue. Finally, an analysis approach using the method of adjoints was developed to evaluate the compatibility of a seeker and drogue combination based on the performance and flight characteristics of each.

7.2 Future Work

Hardware limitations, particularly with the vision tracker, limited our ability to fully demonstrate the capabilities of visual pursuit. An improved visual tracker with the capability to track a moving airborne target against a changing background is an important step to moving this work forward.

Development of the distance-limited contact factor came after flight trials were complete and an experimental test of this method to confirm the simulation results would be a valuable next step to providing a reliable aerial docking capability.

A new direction to take this work would be formation flight. Visual pursuit with its LOS guidance method might fit well with an autonomous formation flying system. A system patterned after the *V-formation* used by geese would have relatively light communications requirements could be implemented such that it would provide inherent collision avoidance, mutual support, and energy savings from flying in the lead aircraft wing-tip vortices.

7.3 Conclusions

The results presented in this dissertation are likely to be most applicable to research into autonomous aerial refueling, even though the aerial recovery problem that motivated this work is different from aerial refueling in several important ways. For example, aerial refueling uses a short drogue with both aircraft flying at the same airspeed while aerial recovery uses a very long drogue with the seeker (or receiver) flying at a much slower airspeed than the tanker or mothership. In addition, aerial refueling generally occurs at airspeeds of 200 Kts or more while aerial recovery occurs at around 40 Kts. Noting all of this, the vision-based guidance techniques developed in this dissertation for aerial docking are directly applicable to autonomous aerial refueling research. The visual pursuit technique is compatible with vision, GPS, or other sensors. It accepts communication of state information from the target platform and has been shown to be stable in the sense of Lyapunov throughout the docking maneuver.

This dissertation highlighted an issue with vision-based systems that use line-of-sight angles and distances in their control methods. As vision-based systems approach their target to dock, distances become very small and angles become very large. This can cause control inputs to suddenly become very large and saturate flight controls and cause the seeker vehicle to miss the target or impact at an undesirable attitude. The literature for control methods developed for missile guidance like pursuit, proportional navigation and their derivatives do not discuss the final moments before impact in great detail if at all. Missile guidance developers do not seem to be greatly troubled by large control inputs or unusual attitudes at contact with the target. However, UAS engaged in aerial docking are greatly affected by large control movements near the target. As was shown

in this dissertation, these effects can begin at several meters from the target and cause unusual attitudes at docking, or can cause the seeker to entirely miss the target. In this dissertation, methods for compensating for line-of-sight issues prior to contact with the target were developed consistent with the stability of the overall guidance method.

Visual pursuit was also shown to be effective in tracking an airborne target from a set distance and to be effective in tracking in high winds. This method would be a good candidate for autonomous formation flying using vision or data links to obtain target position information. Visual pursuit would be an effective tool for providing guidance to individual UAS flying in formation while transiting controlled airspace. Two other guidance methods were developed as part of this dissertation–a vector field method that is useful for following a desired path, and a proportional-integral method that uses only line-of-sight angles and requires no external communication from the target.

The vector-field method was created by mathematically describing the desired flight path as the intersection of two surfaces. The flight path of the target vehicle was estimated by constructing a vector field with contraction and circulation terms that drove the seeker UAS to remain on the estimated path. By controlling seeker UAS airspeed it was shown that a following distance within 5 m was possible. The vector-field approach is a non-vision-based method that allows a UAV without a camera to follow a generic path if the guidance inputs can be passed to it from off board the UAS.

Proportional-integral pursuit used line-of-sight angles and proved to be adequate for aerial tracking. PI pursuit was developed as an alternative control method for comparison with visual pursuit. PI guidance did not perform as well as visual pursuit in following a highly dynamic target like an aerial drogue. However, it does have the advantage of not requiring any electronic communication from the target. Each method proved to be successful in tracking an aerial target using either GPS position data or vision data from an onboard camera. Vision-based guidance was superior to GPS-based guidance, but GPS guidance proved to be an adequate back up when vision data was unavailable.

The method of adjoints proved to be a powerful technique for evaluating system performance. By first linearizing the guidance method, the effects of changing control gains, sensor delay, roll time constant or pitch rate time constant were evaluated to find optimum operating re-

gions and regions of low damping or instability. With the model linearized, an adjoint system is created that allows a designer or analyst to evaluate the effect of system design characteristics as well as target motion and disturbances on docking performance. Using the method of adjoints on the visual pursuit method showed the effects on docking performance from changes in airspeed, closure velocity, system time constant, sensor delay and target motion. In addition, the individual contributions to the overall miss distance can be understood and an overall miss distance can be calculated for different aircraft and target combinations. It has been shown how the method of adjoints is an effective tool for analyzing large and small UAS aerial docking.

REFERENCES

[1] Jacobson, S., 2012. "NASA Dryden status." In *Aerospace Control & Guidance Subcommittee Meeting 109, Salt Lake City, UT*. 2, 6

[2] Bergeron, K., Ward, M., and Costello, M., 2012. "An initial investigation of formation flight for drag reduction on the C-17 aircraft." In *AIAA, Guidance, Navigation and Control Conference*. 2

[3] Weibel, R. E., and Hansman, R. J., 2005. Safety considerations for operation of unmanned aerial vehicles in the national airspace system Tech. Rep. ICAT-2005-1, MIT International Center for Air Transportation, March. 2

[4] Zarchan, P., 1998. "Ballistic missile defense guidance and control issues." *Science & Global Security,* **8**, pp. 99–124. 2, 7, 79, 100

[5] Carlson, D., and Colton, M. B., 2010. "Out-of-plane orbit estimation and tracking for aerial recovery of micro air vehicles." *Proc. IEEE International Conference on Robotics and Automation (ICRA10), Anchorage, Alaska*, May. 3, 7, 67

[6] Sun, L., Hedengren, J. D., and Beard, R. W., 2012. "Optimal trajectory generation using model predictive control for aerially towed cable systems (to appear)." *AIAA Journal of Guidance Control and Dynamics*. 3, 7

[7] Ali, A., and Mirza, S. M., 2006. "Object tracking using corrleation, Kalman filter and fast means shift algorithms." In *2nd International Conference on Emerging Technologies*. 3

[8] Chu, H., and Wang, K., 2009. "Target tracking based on mean shift and improved Kalman flitering algorithm." In *Proceedings of the IEEE International Conference on Automation and Logistics*. 3

[9] Valasek, J., Gunnam, K., Kimmett, J., Tandale, M. D., and Junkins, J., 2005. "Vision-based sensor and navigation system for autonomous air refueling." *Journal Of Guidance, Control, And Dynamics,* **28**(5), pp. 979–989. 3, 6

[10] Fravolini, M. L., Ficola, A., Campa, G., Napolitano, M. R., and Seanor, B., 2004. "Modeling and control issues for autonomous aerial refueling for UAVs using a probe and drogue refueling system." *Aerospace Science and Technology,* **8**, pp. 611–618. 3, 6

[11] Saghafi, F., and Khansari Zadeh, S. M., 2008. "Vision-based trajectory tracking controller for autonomous close proximity operations." In *Proc. IEEE Aerospace Conf*, pp. 1–11. 3

[12] Ferrin, J., Nichols, J., and McLain, T., 2012. "Design and control of a maneuverable towed aerial vehicle." In *AIAA, Guidance, Navigation and Control Conference*. 4, 7

[13] Beard, R. W., and McLain, T. W., 2012. *Small Unmanned Aircraft: Theory and Practice*. Princeton University Press. 4, 11, 28, 36, 41, 68

[14] Nelson, D. R., Barber, D. B., McLain, T. W., and Beard, R. W., 2007. "Vector field path following for miniature air vehicles." *IEEE Transactions on Robotics,* **23**(3), pp. 519–529. 4, 19

[15] Lawrence, D. A., Frew, E. W., and Pisano, W. J., 2008. "Lyapunov vector fields for autonomous unmanned aircraft flight control." *Journal of Guidance, Control, and Dyanmics,* **31**(5), Septermber-October, pp. 1220–1229. 4, 5, 8, 19

[16] Goncalves, V. M., Pimenta, L. C. A., Maia, C. A., Dutra, B. C. O., and Pereira, G. A. S., 2010. "Vector fields for robot navigation along time-varying curves in *n*-dimensions." *IEEE Transactions on Robotics,* **26**(4), pp. 647–659. 4, 5, 8, 19, 20, 21

[17] Ambrosino, G., Ariola, M., Ciniglio, U., Corraro, F., De Lellis, E., and Pironti, A., 2009. "Path generation and tracking in 3-D for UAVs." *IEEE Transactions on Control Systems Technology,* **17**(4), pp. 980–988. 4

[18] Stepanyan, V.and Hovakimyan, N., 2008. "Visual tracking of a maneuvering target." *Journal of Guidance, Control, and Dyanmics,* **31**, pp. 66–80. 5

[19] Calise, A. J., Johnson, E. N., Sattigeri, R., Watanabe, Y., and Madyastha, V., 2005. "Estimation and guidance strategies for vision based target tracking." In *Proc. American Control Conf the 2005*, pp. 5079–5084. 5

[20] Park, S., Deyst, J., and How, J. P., 2007. "Performance and Lyapunov stability of a nonlinear path-following guidance method." *Journal of Guidance, Control, and Dynamics,* **30**(6), November-December, pp. 1718–1728. 5

[21] Wang, L., Dong, X. M., Guo, J., and Jia, H. Y., 2012. "Autonomous aerial refueling for UAVs based on GPS/MV." *Advanced Materials Research,* **433**, pp. 4087–4094. 6

[22] Ryan, J., 2012. Autonomous aerial refueling and formation flight at NASA Dryden Flight Research Center Tech. Rep. Doc ID: 20120013571, National Aeronautics and Space Administration, March. 6

[23] Saunders, J., and Beard, R. W., 2011. "Visual tracking in wind with field of view constraints." *International Journal of Micro Air Vehicles,* **3**(3), September, pp. 169–182. 6

[24] Wyllie, T., 2001. "Parachute recovery for UAV systems." *Aircraft Engineering and Aerospace Technology,* **73**(6), pp. 542–551. 6

[25] Mullens, K., Burmeister, A., Wills, M., Stroumtsos, N., Denewiler, T., Thomas, K., and Stancliff, S., 2004. "Automated launch, recovery, and refueling for small Unmanned Aerial Vehicles." *Mobile Robots XVII, Society of Photo-Optical Instrumentation Engineers, SPIE Proceedings Series,* **5609**, pp. 233–243. 6

[26] Kahn, A. D., 2010. "Vision-based recovery and guidance for small unmanned air vehicles." In *AIAA Guidance, Navigation, and Control Conference*. 6

[27] Williamson, W. R., Glenn, G. J., Dang, V. T., Speyer, J. L., Stecko, S. M., and Takacs, J. M., 2009. "Sensor fusion applied to autonomous aerial refueling." *Journal of Guidance Control and Dynamics,* **32**, pp. 262–275. 6

[28] Sun, L., Beard, R. W., Colton, M. B., and McLain., T. W., 2009. "Dynamics and control of cable-drogue system in aerial recovery of micro air vehicles based on Gauss's principle." In *American Control Conference*, pp. 4729–4734. 7

[29] Sun, L., and Beard, R. W., 2010. "Towed body altitude stabilization and states estimation in aerial recovery of micro air vehicles." In *AIAA, Guidance, Navigation and Control Conference*. 7

[30] Sun, L., Beard, R. W., and Colton, M. B., 2010. "Motion planning and control for mothership-cable-drogue systems in aerial recovery of micro air vehicles." In *American Control Conf*, pp. 2101–2106. 7, 66

[31] Colton, M., Sun, L., Carlson, D., and Beard, R., 2011. "Multi-vehicle dynamics and control for aerial recovery of micro air vehicles." *Int. Journal of Vehicle Autonomous Systems,* **9**, pp. 78–107. 7

[32] Sun, L., and Beard, R. W., 2011. "Towed-body trajectory tracking in aerial recovery of micro air vehicle in the presence of wind." In *American Control Conference*, pp. 3209–3214. 7, 67

[33] Owen, M. A., Nichols, J. W., and Colton, M. B., 2011. "Cooperative aerial tracking and rendezvous along time-optimal 3-dimensional curves." In *AIAA, Guidance, Navigation and Control Conference*. 7, 8, 19

[34] Nichols, J., Ferrin, J., Owen, M., and McLain, T., 2012. "Vision-enhanced aerial rendezvous along elliptical paths." In *AIAA Guidance, Navigation and Control Conference, Minneapolis, Minnesota*. 7, 8, 9

[35] Nichols, J. W., Sun, L., Beard, R., and McLain, T., 2013 (Submitted). "Aerial rendezvous of small unmanned aircraft using a passive towed cable system." *Journal of Guidance, Dynamics, and Control*. 7, 9, 10

[36] Nichols, J. W., and McLain, T., 2013. "A nonlinear guidance law for visual pursuit of a cooperative aerial target in wind." *International Journal of Micro Air Vehicles,* **5**(2), June, pp. 127–143. 7, 8, 10

[37] Park, S., 2004. "Avionics and control system development for mid-air rendezvous of two unmanned aerial vehicles." Ph.d dissertation, Massachusetts Institute of Technology, February. 7, 19

[38] Shneydor, N. A., 1998. *Missile Guidance and Pursuit*. Horwood. 7, 34, 42

[39] Zarchan, P., 2007. *Tactical and Strategic Missile Guidance*., 5th ed., Vol. 219, Progress in Aeronautics and Astronautics American Institute of Aeronautics and Astronautics, Inc, 1801 Alexander Bell Drive, Reston, VA 20191-4344. 7, 79, 94

[40] Zarchan, P., 1995. "Proportional navigation and weaving targets." *Journal of Guidance Control and Dynamics,* **18**, pp. 969–974. 7, 79

[41] Laning Jr., J. H., and Battin, R. H., 1956. *Control Systems Engineering*. McGraw-Hill. 7, 87, 88

[42] Zarchan, P., 1979. "Complete statistical analysis of nonlinear missile guidance systems - slam." *Journal Of Guidance and Control,* **2**, pp. 71–78. 7

[43] Bucco, D., 2010. Aerospace applications of adjoint theory Tech. Rep. 20100817005, Defence Science and Technology Organisation, Commonwealth of Australia, January. 7, 88, 94

[44] Hall, J. K., 2009. "Attitude estimation and maneuvering for autonomous obstacle avoidance by miniature air vehicles." PhD thesis, Brigham Young University. 11

[45] Owen, M. A., 2011. "Aerial rendezvous of an unmanned air vehicle along time-optimal Dubins airplane interception paths with an air vehicle following an arbitrarily oriented ellipse." Master's thesis, Brigham Young University. 23

[46] Barber, D., Griffiths, S., McLain, T., and Beard, R. W., 2007. "Autonomous landing of miniature aerial vehicles." *AIAA Journal of Aerospace Computing, Information, and Communication,* **4**, pp. 70–84. 24

[47] Grewal, M. S., Weill, L. R., and Andrews, A. P., 2007. *Global Positioning Systems, Inertial Navigation, and Integration*., second ed. John Wiley & Sons. 27, 69

[48] United States Air Force, 2012. *Combat Aircraft Fundamentals*., 3.3.F-15 ed. 34

[49] Khalil, H. K., 2002. *Nonlinear Systems*., third ed. Prentice Hall. 44, 124

[50] Sun, L., Beard, R. W., and Colton, M. B., 2010. "Motion planning and control for mothership-cable-drogue systems in aerial recovery of micro air vehicles." In *American Control Conference*, pp. 2101 – 2106. 67

[51] Sinha, N., 2008. *Control Systems*., third ed. New Age International. 80

[52] Kay, S. M., 1993. *Fundamentals of statistical signal processing*. Prentice Hall. 95

[53] Northrop Grumman Corporation, 2008. RQ-4 Global Hawk, May. 107

APPENDIX A. GUIDANCE LAWS FROM DECOUPLED DYNAMICS

Visual pursuit was originally developed using two-dimensional dynamics. Simulation and flight experimentation showed visual pursuit to be an effective and robust guidance method for air-to-air tracking. However, in order to provide a more rigorous proof of visual pursuit, three-dimensional dynamics were used to develop the guidance laws shown in Chapter 4. In this appendix, the guidance laws based on two-dimensional dynamics are presented along with a comparison of performance between the two models. It will be shown that the two-dimensional guidance equations are a very good representation of the three-dimensional guidance equations.

A.1 Longitudinal Dynamics

The relative longitudinal dynamics between the seeker and the drogue are expressed in two-dimensional polar coordinates with the inertial y-axis projected onto the inertial x and z-axes as shown in Figure A.1.

Let $\mathbf{v}_S$ and $\mathbf{v}_T \triangleq (V_x^i, V_z^i)^T \in \mathbb{R}^2$, where $\mathbf{v}_S$ is the seeker velocity vector and $\mathbf{v}_T$ is the target velocity vector. The target vehicle is assumed to be flying at a constant altitude. The time rate of change of the LOS vector $\mathbf{P}$ in the x-z inertial frame is computed by taking the vector difference of the target and seeker velocities according to

$$\dot{\mathbf{P}}^{x\text{-}z\,i} = \mathbf{v}_T - \mathbf{v}_S, \tag{A.1}$$

where,

$$\mathbf{v}_T = \begin{bmatrix} V_T \\ 0 \end{bmatrix} \tag{A.2}$$

$$\mathbf{v}_S = \begin{bmatrix} V_S \cos\gamma \\ V_S \sin\gamma \end{bmatrix}. \tag{A.3}$$

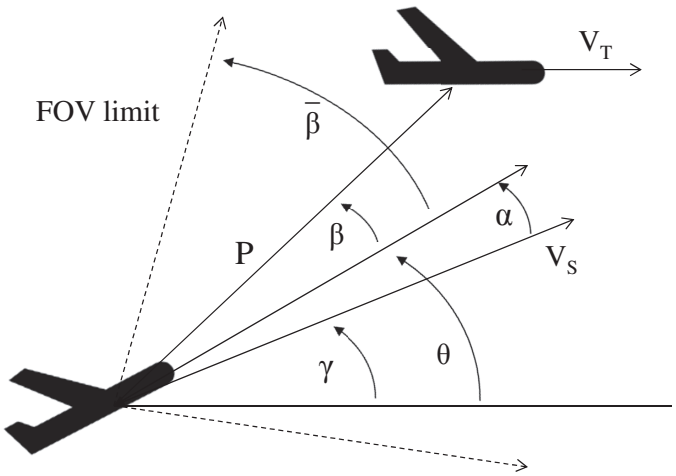

Figure A.1: Two-dimensional longitudinal polar coordinates of the seeker and target in the *x*-*z* inertial frame, where β is the angle between the seeker pitch angle θ and the longitudinal LOS vector; **P** is the LOS vector; and the angle $\bar{\beta}$ is the maximum FOV angle. The LOS frame of reference is aligned with the LOS vector **P**.

The counterclockwise rotation matrix from the two-dimensional inertial to the line-of-sight frame is

$$\mathbf{R}_{x\text{-}z\,i}^{LOS} = \begin{bmatrix} \cos(\theta+\beta) & -\sin(\theta+\beta) \\ \sin(\theta+\beta) & \cos(\theta+\beta) \end{bmatrix}. \tag{A.4}$$

$$\begin{bmatrix} \dot{P}_r \\ \dot{P}_t \end{bmatrix} = \begin{bmatrix} (V_T - V_S\cos\gamma)\cos(\theta+\beta) + V_S\sin\gamma\sin(\theta+\beta) \\ (V_T - V_S\cos\gamma)\sin(\theta+\beta) - V_S\sin\gamma\cos(\theta+\beta) \end{bmatrix},$$

and can be simplified to

$$= \begin{bmatrix} V_T\cos(\theta+\beta) - V_S\cos(2\theta+\beta) \\ V_T\sin(\theta+\beta) - V_S\sin(2\theta+\beta) \end{bmatrix}. \tag{A.5}$$

Therefore from (A.5), the time rate of change in the line-of-sight vector in the tangential direction is

$$\dot{P}_t = V_T \sin(\theta+\beta) - V_S \sin(2\theta+\beta). \tag{A.6}$$

From the dynamics shown in Figure A.1, the change in the LOS vector in the radial direction $\dot{P}$ and tangential direction $\dot{P}_t$ can be expressed as

$$\begin{bmatrix} \dot{P}_r \\ \dot{P}_t \end{bmatrix} = \begin{bmatrix} \dot{P} \\ P(\dot{\theta}+\dot{\beta}) \end{bmatrix}. \tag{A.7}$$

Using the relationships for $\dot{P}_t$ in (A.6) and (A.7) the change in the longitudinal LOS angle β is found to be

$$\dot{\beta} = \frac{V_T \sin(\theta+\beta) - V_S \sin(\theta+\beta+\gamma)}{P} - \dot{\theta}. \tag{A.8}$$

From (A.5) and (A.7) it can be seen that the rate of change in the longitudinal LOS distance between the seeker and the target can be expressed as

$$\dot{P} = V_T \cos(\theta+\beta) - V_S \cos(\theta+\beta+\gamma). \tag{A.9}$$

In the x-z plane,

$$\dot{\theta} = q. \tag{A.10}$$

The dynamics of θ are hidden in the development of visual pursuit. However in Chapter 4, θ was shown to be well behaved for typical maneuvers.

A.2 Lateral Dynamics

The relative lateral dynamics between the seeker and the drogue are expressed in two-dimensional polar coordinates with the inertial z-axis projected onto the inertial x and y-axes as shown in Figure A.2.

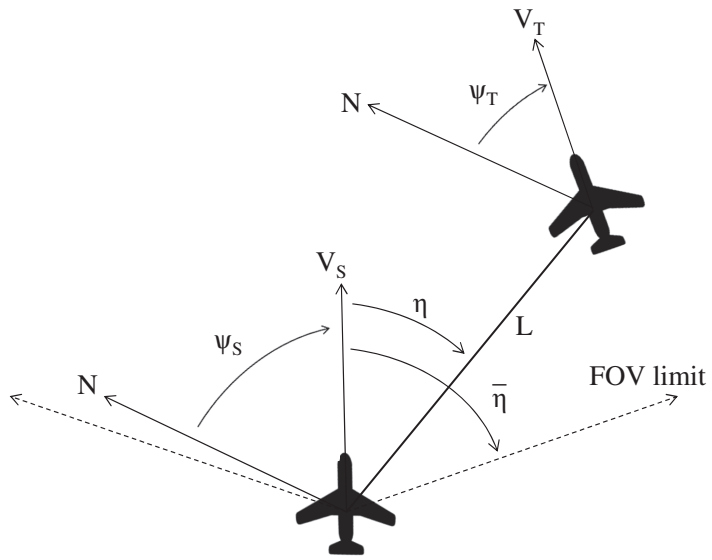

Figure A.2: Two-dimensional lateral polar coordinates of the seeker and target in the *x*-*y* inertial frame. Where **L** is the LOS vector between the seeker and the target; η is the angle between the seeker heading and the line-of-sight vector; $\bar{\eta}$ is the maximum FOV angle; and the angles ψ_S, and ψ_T are the seeker and target headings.

Let **L** be the line-of-sight vector and η be the lateral line-of-sight angle or the angle between the optical axis of the seeker and the target.

$$\dot{\mathbf{L}}^{x\text{-}y\,i} = \mathbf{v}_T - \mathbf{v}_S, \tag{A.11}$$

where,

$$\mathbf{v}_T = \begin{bmatrix} V_T \cos\psi_T \\ V_T \sin\psi_T \end{bmatrix} \tag{A.12}$$

$$\mathbf{v}_S = \begin{bmatrix} V_S \cos\psi_S \\ V_S \sin\psi_S \end{bmatrix}. \tag{A.13}$$

The clockwise rotation matrix from the two-dimensional inertial to the line-of-sight frame is

$$\mathbf{R}_{x\text{-}y\,i}^{LOS} = \begin{bmatrix} \cos(\psi_S+\eta) & \sin(\psi_S+\eta) \\ -\sin(\psi_S+\eta) & \cos(\psi_S+\eta) \end{bmatrix}. \tag{A.14}$$

In the LOS frame, the lateral LOS vector can be expressed in terms of radial and tangential components as

$$\begin{aligned} \dot{\mathbf{L}}^{LOS} &\triangleq \begin{bmatrix} \dot{L}_r \\ \dot{L}_t \end{bmatrix} \\ &= \mathbf{R}_{x\text{-}y\,i}^{LOS}\dot{\mathbf{L}}^{\,x\text{-}y\,i} \end{aligned} \tag{A.15}$$

$$= \begin{bmatrix} (V_T(\cos\psi_T\cos(\psi_S+\eta)+\sin(\psi_S+\eta)\sin\psi_T)+V_S(\cos(\psi_S+\eta)\cos\psi_S+\sin\psi_S\sin(\psi_S+\eta)) \\ (V_T(-\cos\psi_T\sin(\psi_S+\eta)+\cos(\psi_S+\eta)\sin\psi_T)-V_S(-\cos(\psi_S+\eta)\cos\psi_S+\sin\psi_S\cos(\psi_S+\eta)) \end{bmatrix} \tag{A.16}$$

and can be simplified to

$$\begin{bmatrix} \dot{L}_r \\ \dot{L}_t \end{bmatrix} = \begin{bmatrix} -V_S\cos\eta+V_T\cos(\psi_S-\psi_T+\eta) \\ V_S\sin\eta-V_T\sin(\psi_S-\psi_T+\eta) \end{bmatrix}. \tag{A.17}$$

Therefore from (A.17), the time rate of change in the line-of-sight vector in the tangential direction is

$$\dot{L}_t = V_S\sin\eta-V_T\sin(\psi_S-\psi_T+\eta). \tag{A.18}$$

From the dynamics shown in Figure 4.5, the change in the LOS vector in the radial direction $\dot{\rho}$ and in the tangential direction $\dot{\rho}_t$ can be expressed as

$$\begin{bmatrix} \dot{L}_r \\ \dot{L}_t \end{bmatrix} = \begin{bmatrix} \dot{L} \\ L(\dot{\psi}_S+\dot{\eta}) \end{bmatrix}. \tag{A.19}$$

Using the relationships for $\dot{L}_t$ in (A.17) and (A.19) the change in the lateral LOS angle η is found to be

$$\dot{\eta} = -\dot{\psi}_S + \frac{V_S}{L}\sin\eta - \frac{V_T}{L}\sin(\psi_S - \psi_T + \eta). \tag{A.20}$$

Using the expression for a coordinated turn

$$\dot{\psi}_S = \frac{g}{V_S}\tan\phi, \tag{A.21}$$

the expression for $\dot{\eta}$ can now be written as a function of bank angle ϕ according to

$$\dot{\eta} = -\frac{g}{V_S}\tan\phi + \frac{V_S}{L}\sin\eta - \frac{V_T}{L}\sin(\psi_S - \psi_T + \eta). \tag{A.22}$$

From (A.17) and (A.19) it can be seen that the rate of change in the lateral LOS distance between the seeker and the target can be expressed at

$$\dot{L} = V_T\cos(\psi_S - \psi_T + \eta) - V_S\cos\eta. \tag{A.23}$$

The dynamics of ψ_S are hidden in the development of visual pursuit. However in Chapter 4, ψ_S was shown to be well behaved for typical maneuvers.

A.3 Visual Pursuit in Two Dimensions

Using the LOS angles described in Figures A.1 and A.2, we develop longitudinal and lateral guidance methods for the seeker. The objective is to develop methods that will ensure that once the target has been captured in the camera FOV, the guidance methods will keep the target in the FOV. In other words we want to develop a function that produces control inputs that will drive the longitudinal LOS angle β to zero. In the lateral direction the goal is slightly different. Rather than drive η to zero, it should converge to a region around the center of the image, but not necessarily the image center. This relaxation in the lateral direction will be shown to improve performance in wind and still guarantee convergence to a region within the camera image. We use bank angle ϕ^c,

pitch rate q^c, and seeker airspeed V_S^c as the control inputs as shown in the system block diagram in Figure 4.6.

An approximation for L and P is made in the guidance laws derived from decoupled dynamics in this appendix. The approximation is to use the three-dimensional LOS distance ρ in the calculation of ϕ^c, q^c, and V_S^c. Since ρ will always be greater than L and P, this will not cause instability. There could be some degradation in performance at extreme angles, but this was not observed in practice. As will be shown later in this appendix, the simulation results show a very high degree of correlation between the guidance laws developed using coupled dynamics and the guidance laws presented in this appendix that were developed using decoupled dynamics. In addition, as will be shown in Chapter 5, artificially increasing the LOS distance ρ is a necessary process for good docking performance. Therefore, ρ is used as an approximation for L and P in the guidance laws developed in this appendix.

Since the guidance method is an outer guidance loop that wraps around a higher bandwidth inner autopilot control loop we assume that the commanded guidance inputs ϕ^c and q^c track the instantaneous roll and pitch rate for the purpose of proving stability of the methods. We now develop a Lyapunov function based on ρ, η and β that will drive us to select values for V_S, ϕ^c and q^c that will be convergent about the center of the image. Consider the Lyapunov function

$$\mathbf{W} = \underbrace{\frac{1}{2}\beta^2}_{\mathbf{W}_1} + \underbrace{\frac{1}{2}\eta^2}_{\mathbf{W}_2} + \underbrace{\frac{1}{2}\rho^2}_{\mathbf{W}_3}. \tag{A.24}$$

Differentiating the function with respect to time yields

$$\dot{\mathbf{W}} = \underbrace{\beta\dot{\beta}}_{\dot{\mathbf{W}}_1} + \underbrace{\eta\dot{\eta}}_{\dot{\mathbf{W}}_2} + \underbrace{\rho\dot{\rho}}_{\dot{\mathbf{W}}_3}. \tag{A.25}$$

For the system to be stable or in other words to ensure that the target will remain within the FOV, $\dot{\mathbf{W}}$ must remain negative at all times [49]. This is accomplished by ensuring that each of the subterms $\dot{\mathbf{W}}_1$, $\dot{\mathbf{W}}_2$ and $\dot{\mathbf{W}}_3$ remain negative. The value of each subterm is a function of our choice for pitch rate q^c, roll angle ϕ^c and seeker airspeed V_S^c. Each will be addressed in turn.

Longitudinal Guidance

Beginning with the subterm $\dot{\mathbf{W}}_1$ from (A.25) and substituting (A.8) for $\dot{\beta}$ we see that

$$\begin{aligned} \dot{\mathbf{W}}_1 &= \beta\dot{\beta} \\ &= \beta\left(\frac{V_T\sin(\theta+\beta)-V_S\sin(\theta+\beta+\gamma)}{P}-\dot{\theta}\right). \end{aligned} \tag{A.26}$$

By substituting (A.10) and selecting the pitch rate q to be

$$q^c = \frac{V_T\sin(\theta+\beta)-V_S\sin(\theta+\beta+\gamma)}{P}+K_\theta\beta \tag{A.27}$$

and substituting into (A.26), the function becomes

$$\dot{\mathbf{W}}_1 = -K_\theta\beta^2. \tag{A.28}$$

If the gain K_θ is chosen to be positive, $\dot{\mathbf{W}}_\mathbf{1}$ is always negative which ensures that while using (A.27) for q^c, the target location in the camera FOV will longitudinally move toward the center of the image plane.

Lateral Guidance

Beginning with the subterm $\dot{\mathbf{W}}_2$ from (A.25) and substituting (A.22) for $\dot{\eta}$ we see that

$$\begin{aligned} \dot{\mathbf{W}}_2 &= \eta\dot{\eta} \\ &= \eta\left[-\dot{\psi}_S+\frac{1}{\rho}(V_S\sin\eta+V_T\sin(\psi_S-\psi_T+\eta))\right]. \end{aligned} \tag{A.29}$$

Using the expression for a coordinated turn

$$\dot{\psi}_S = \frac{g}{V_S}\tan\phi, \tag{A.30}$$

the expression for $\dot{\mathbf{W}}_2$ can now be written as a function of bank angle ϕ according to

$$\dot{\mathbf{W}}_2 = \eta \left[-\frac{g}{V_S} \tan\phi + \frac{1}{\rho}(V_S \sin\eta - V_T \sin(\psi_S - \psi_T + \eta)) \right]. \tag{A.31}$$

The lateral control must support two objectives, aerial tracking and aerial docking. Using bank angle command ϕ^c, the lateral control can be tailored for each purpose.

Lateral Command for Docking

For docking, it is desirable that the seeker LOS be pointed directly at the drogue such that at contact the seeker body-x axis is nearly perpendicular with the face of the drogue. The commanded bank angle ϕ^c is selected such that the nonlinear terms in (A.31) are zero according to

$$\phi^c = \tan^{-1}\left[\frac{V_S}{g} \left(\frac{1}{\rho}(V_S \sin\eta - V_T \sin(\psi_S - \psi_T + \eta)) + K_\phi \eta \right) \right] \tag{A.32}$$

and substituting back into (4.30), the scalar subterm becomes

$$\dot{\mathbf{W}}_2 \;=\; -K_\phi \eta^2. \tag{A.33}$$

If the gain K_ϕ is chosen to be positive, $\dot{\mathbf{W}}_\mathbf{2}$ is always negative which ensures that while using (A.32) for $\dot{\phi}^c$, the target location in the camera FOV will laterally move toward the center of the image plane.

Lateral Command for Tracking

Winds in the small UAS flight environment are often the dominant environmental factor to overcome when doing precision guidance. To accommodate high cross winds when tracking an airborne target, the lateral guidance has been extended in a way that preserves the desirable stability features and drives the target to a stable region of the image frame, but not necessarily to the center of the image. This is accomplished by adding $K_\phi \eta - \nu$ to the commanded roll angle ϕ^c

such that the nonlinear terms in (A.31) are zero according to

$$\phi^c = \tan^{-1}\left[\frac{V_S}{g}\left(\frac{1}{\rho}(V_S\sin\eta - V_T\sin(\psi_S - \psi_T + \eta)) + K_\phi\eta - \nu\right)\right] \tag{A.34}$$

and substituting back into (4.30), the scalar subterm becomes

$$\dot{\mathbf{W}}_2 \;=\; -K_\phi\eta^2 + \eta\nu. \tag{A.35}$$

For $\dot{\mathbf{W}}_2$ to remain negative,

$$|\nu| \;<\; K_\phi\eta. \tag{A.36}$$

From (A.35) and (A.36) and choosing K_ϕ to be positive ensures the target image will be driven to a region around the center of the image if we control ϕ according to (A.34). The parameter ν is optimized to allow the seeker vehicle to keep the target in the field of view, but adjust the seeker heading such that the seeker is pointed into or with the prevailing wind as much as possible. The optimization scheme is described in Section 4.3.2.

Airspeed Control

Since the target is assumed to be flying at a constant altitude, the lateral LOS distance is used in the calculation for the nonlinear airspeed control. Beginning with the subterm $\dot{\mathbf{W}}_3$ from (A.25) and substituting (A.23) for $\dot{\rho}$ we see that

$$\begin{aligned}\dot{\mathbf{W}}_3 &= \rho\dot{\rho} \\ &= V_T\cos(\psi_S - \psi_T + \eta) - V_S\cos\eta).\end{aligned} \tag{A.37}$$

Airspeed control supports two objectives, aerial tracking and aerial docking. Using seeker commanded airspeed V_S^c, the airspeed control is tailored for each purpose.

Airspeed Control for Docking

In the docking scenario, the distance between the seeker and the drogue will decrease until the two vehicles make contact. Separation distance is controlled by airspeed V_S^c, and is selected such that the nonlinear terms in (A.37) are zero according to

$$V_S^c = \frac{V_T \cos(\psi_S - \psi_T + \eta) + V_C}{\cos\eta} \tag{A.38}$$

where V_C is the closure velocity. Substituting back into (A.37), the scalar subterm becomes

$$\dot{\mathbf{W}}_3 = -V_C \rho. \tag{A.39}$$

If V_C is chosen to be positive and the separation distance ρ remains positive, $\dot{\mathbf{W}}_\mathbf{3}$ is always negative which ensures that while using (A.38) for V_C, the target location in the camera FOV will remain in the FOV as the seeker approaches the drogue. As the LOS angles become very small, (A.38) reduces to

$$V_S^c = V_T + V_C. \tag{A.40}$$

Airspeed Control for Tracking

In the tracking scenario, the seeker maintains a desired separation distance ρ^d from the target. The error between the actual separation distance $\rho^d - \rho$ is substituted for ρ in (A.24) such that

$$\begin{aligned} \mathbf{W}_3 &= \frac{1}{2}(\rho^d - \rho)^2 \\ \dot{\mathbf{W}}_3 &= -\dot{\rho}(\rho^d - \rho) \\ &= -(V_T \cos(\psi_S - \psi_T + \eta) - V_S \cos\eta))(\rho^d - \rho). \end{aligned} \tag{A.41}$$

The airspeed V_S^c is selected such that the nonlinear terms in (A.41) are zero according to

$$V_S^c = \frac{V_T \cos(\psi_S - \psi_T + \eta) - K_v(\rho^d - \rho)}{\cos\eta} \tag{A.42}$$

and substituting back into (A.41), the scalar subterm becomes

$$\dot{\mathbf{W}}_{\mathbf{3}} \quad = \quad -K_V(\rho^d - \rho)^2. \tag{A.43}$$

If K_V is chosen to be positive, $\dot{\mathbf{W}}_{\mathbf{3}}$ is always negative which ensures that while using (A.42) for V_C, the target location in the camera FOV will remain in the FOV as the seeker tracks the target from a desired separation distance. As the LOS angles become very small, (A.42) reduces to proportional control according to

$$V_S^c = V_T - K_V(\rho^d - \rho). \tag{A.44}$$

A.4 Simulation Results

To show the correlation of the guidance laws developed using coupled dynamics in Chapter 4 and the guidance laws developed in this appendix using decoupled dynamics, two simulations were conducted to look at tracking and docking performance. The simulations were conducted using the six-DOF aerodynamics and system model discussed previously. The docking performance simulation was conducted by flying the drogue on a straight path with 5 m/s of crosswind, 1 m/s of updraft and noise on the vision sensor. The comparison of guidance inputs and LOS performance during the docking simulation are shown in Figure A.3. From Figure A.3 there appears to be very little difference in the performance of the two guidance models. Looking at the mean values over the total period of the docking maneuver as shown in Table A.1, the RMS values differ by less than 2 percent for all of the control inputs.

Table A.1: Comparison of coupled and decoupled guidance laws during docking

	Coupled guidance laws	Decoupled guidance laws
LOS RMS (deg)	3.26	3.28
ϕ RMS (deg)	6.70	6.92
θ RMS (deg)	3.99	3.82
airspeed RMS (m/s)	18.37	18.53

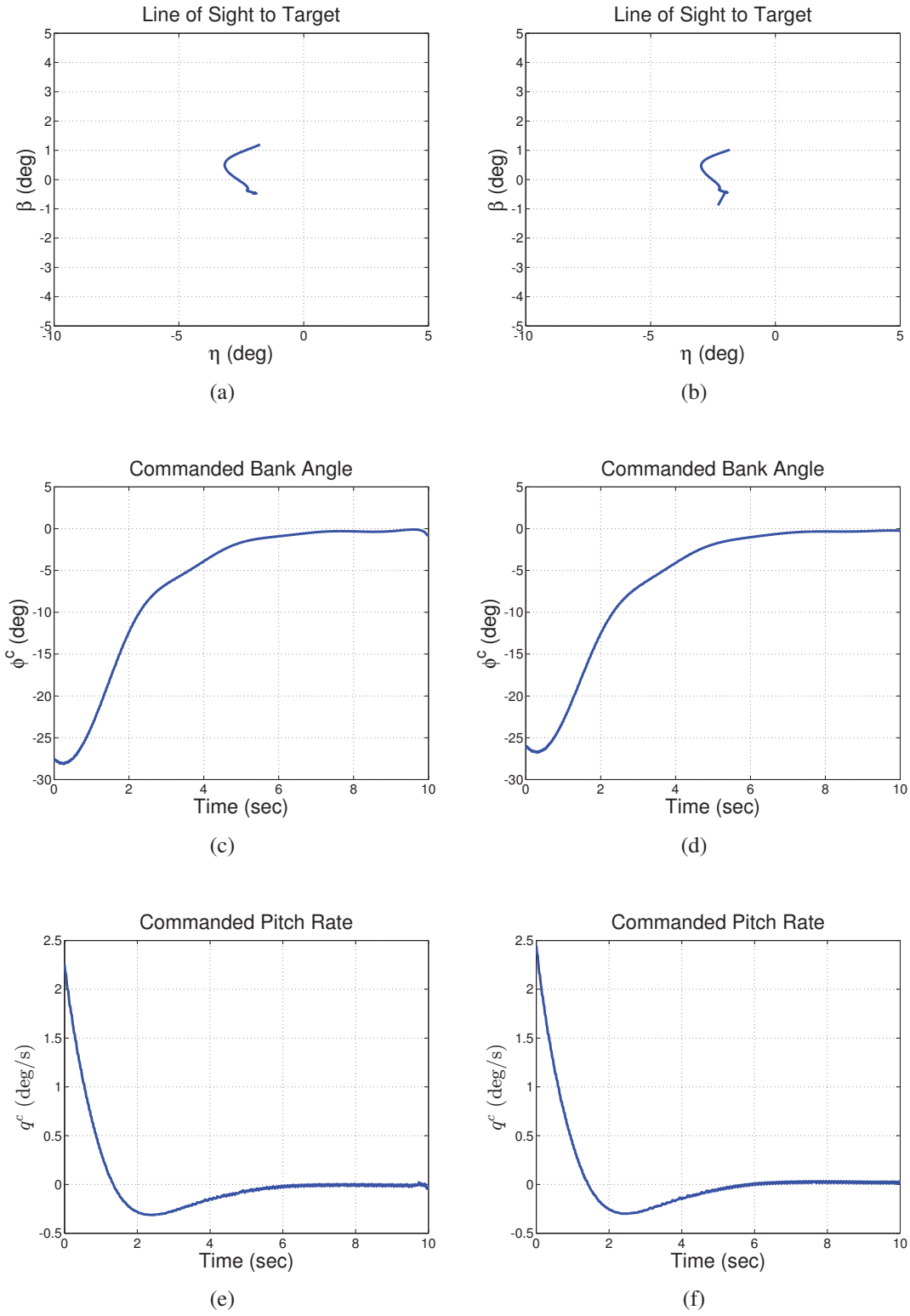

Figure A.3: Comparison of coupled and decoupled guidance laws during docking; (a) coupled LOS error; (b) decoupled LOS error; (c) coupled commanded bank angle; (d) decoupled commanded bank angle; (e) coupled commanded pitch rate; (f) decoupled commanded pitch rate.

Tracking performance was compared using the waggle maneuver shown in Figure 4.10. This maneuver tests primarily the lateral control with turns of varying radii and direction against a 7 m/s wind, 1 m/s of down draft and noise on the vision sensor. The comparison of guidance inputs and LOS performance during tracking are shown in Figures A.4 and A.5.

From these results there appears to be very little difference in the performance of the two guidance models. Looking at the mean values over the total period of tracking as shown in Table A.2, the RMS values differ by less than 1 percent for all of the control inputs over more 70 s of simulation in challenging wind conditions. It can be seen that airspeed saturates on the upper and lower bound for short periods of time. The stability proof was based on the assumption that the controls do not saturate. However, it was observed that the guidance methods is robust to short periods of saturation as long as they do not occur in very close proximity to the target.

Table A.2: Comparison of coupled and decoupled guidance laws during tracking

	Coupled guidance laws	Decoupled guidance laws	Decoupled guidance with proportional airspeed control
LOS RMS (deg)	7.23	7.16	7.66
ρ RMS (m)	35.17	35.39	30.09
ϕ RMS (deg)	14.43	14.45	14.95
θ RMS (deg)	5.36	5.42	5.29
airspeed RMS (m/s)	17.03	17.03	17.21

The simplified relationships for airspeed during docking (A.40) and tracking (A.44) along with the decoupled guidance laws for ϕ^c and q^c were used throughout the flight trials conducted during the work on this dissertation. Using the same tracking simulation shown in Figures A.4 and A.5, the simplified airspeed control (A.44) for tracking along with the guidance laws for ϕ^c (A.34) and q^c (A.27) developed in this appendix are compared against the guidance laws developed from coupled dynamics in Chapter 4 (4.26), (4.33), and (4.44). The results are tabulated in Table A.2. Looking at the mean values over the total period of tracking as shown, the RMS values differ by less than 10 percent.

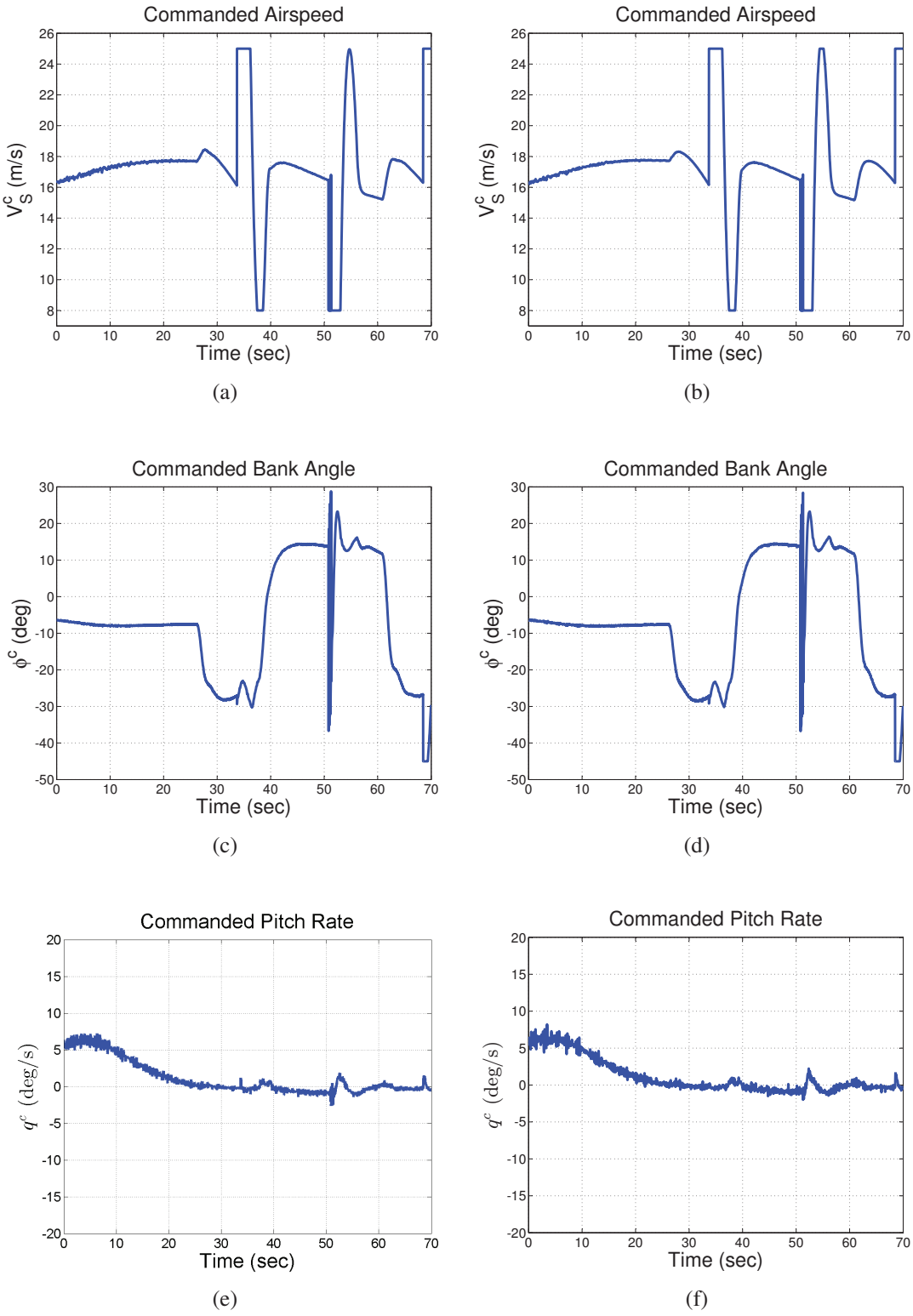

Figure A.4: Comparison of coupled and decoupled guidance laws during tracking with $|v| < 0.6$; (a) coupled commanded airspeed; (b) decoupled commanded airspeed; (c) coupled commanded bank angle; (d) decoupled commanded bank angle; (e) coupled commanded pitch rate; (f) decoupled commanded pitch rate.

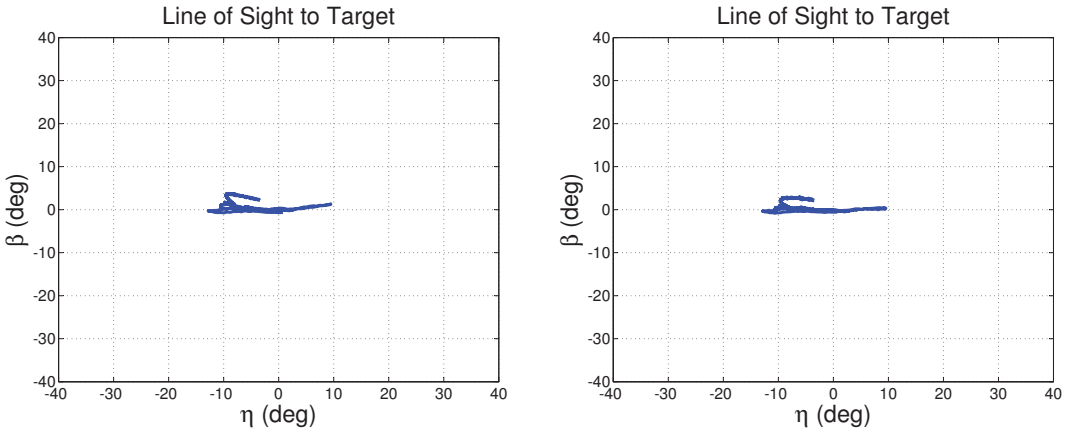

(a)

Figure A.5: Comparison of coupled and decoupled LOS during tracking with $|v| < 0.2$; (a) Coupled airspeed; (b) Decoupled airspeed.